



**WICHITA STATE
UNIVERSITY**

UNIVERSITY LIBRARIES

**Fabrication and characterization of electrospun
polyacrylonitrile carbonized fibers as strain gauges in
composites for structural health monitoring applications**

Item Type	Dissertation
Authors	Alarifi, Ibrahim M.
Publisher	Wichita State University
Rights	Copyright 2017 by Ibrahim M. Alarifi All Rights Reserved
Download date	2026-05-13 17:20:44
Link to Item	http://hdl.handle.net/10057/14538

FABRICATION AND CHARACTERIZATION OF ELECTROSPUN
POLYACRYLONITRILE CARBONIZED FIBERS AS STRAIN GAUGES IN COMPOSITES
FOR STRUCTURAL HEALTH MONITORING APPLICATIONS

A Dissertation by

Ibrahim M. Alarifi

Master of Science, Southern Methodist University, 2016

Master of Science, Eastern Michigan University, 2010

Bachelor of Engineering, University of Toledo, 2008

Submitted to the Department of Mechanical Engineering
and the faculty of the Graduate School of
Wichita State University
in partial fulfillment of
the requirements for the degree of
Doctor of Philosophy

July 2017

© Copyright 2017 by Ibrahim M. Alarifi

All Rights Reserved

Note that the dissertation work is protected by copyright, with all right reserved. Only author has the legal right to publish, produce, sell, or distribute this work. Author permission is needed for others to directly quote significant amounts of information in their own work or to summarize substantial amounts of information in their own work. Limited amounts of information cited, paraphrased, or summarized from the work may be used with proper citation of where to find the original work.

FABRICATION AND CHARACTERIZATION OF ELECTROSPUN
POLYACRYLONITRILE CARBONIZED FIBERS AS STRAIN GAUGES IN COMPOSITES
FOR STRUCTURAL HEALTH MONITORING APPLICATIONS

The following faculty members have examined the final copy of this dissertation for form and content, and recommend that it be accepted in partial fulfillment of the requirement for the degree of Doctor of Philosophy with a major in Mechanical Engineering.

Ramazan Asmatulu, Committee Chair

Muhammad Rahman, Committee Member

Hamid M. Lankarani, Committee Member

Rajeev Nair, Committee Member

Abu Asaduzzaman, Committee Member

Accepted for the College of Engineering

Royce Bowden, Dean

Accepted for the Graduate School

Dennis Livesay, Dean

DEDICATION

To my loving parents, Mr. Mohammed and Modhi Alarifi, for giving me their full support during my overseas study; to my family who openhandedly provided me with a healthy environment in order to proceed with my studies here in the United States; to my dear brothers and sisters back home who have supported me during my absence

ACKNOWLEDGEMENTS

I would like to express my true appreciation to my boss and advisor, Dr. Ramazan Asmatulu, for his support, and for providing me with clear guidance, inspiration, suggestions, criticism, and financial assistance on my Ph.D. journey. I could not have asked for a better mentor, and I owe him much for his support over the years. His leadership consistently challenged me to be a better researcher and provided the right environment for me to achieve my goals. I am proud to have worked under him while completing my doctoral degree at Wichita State University.

I would like to express appreciation to my department chair Dr. Muhammad Rahman for his efforts in the Department of Mechanical Engineering, which created a warm and healthy environment. Special thanks go to Dr. Hamid M. Lankarani for his honest opinions and guidance aimed at enrolling me in the department and helping me to continue my Ph.D. study. Also, thanks to Dr. Rajeev Nair who provided me with valuable feedback, time, and advice on my Ph.D.'s dissertation.

My sincere thanks go to Dr. Abu Asaduzzaman for his efficient and valuable help on my Ph.D. project. I especially thank my team in the mechanical engineering department for their guidance, for sharing knowledge, and for assistance during the experimental process.

Finally, I acknowledge my parents, wife, children, sisters, and brothers for their continuous support and encouragement.

ABSTRACT

This dissertation is aimed at developing new materials to be used as strain gauges in structural health monitoring (SHM) of composite aircraft structures. The unabated growth in air traffic has spurred increased demand in the aerospace industry to manufacture reduced-cost aircraft that are efficient to operate, friendly to the environment, and have an adequate level of safety. Due to their easy manufacturing process and high performance, carbon-based piezoresistive sensors, such as carbon nanotubes, graphite, and graphene, have been developed as alternatives to the traditional silicon/metal-based microelectromechanical system (MEMS), with applications ranging from industrial to medical fields. These sensors can be used in in-situ SHM industries and prosthesis applications because of their small size and high sensitivity to small forces. The detection of flaws and monitoring on a continuous and routine basis is the motive behind SHM devices. Nanomaterials play an remarkable role in the development of nanotechnology. Carbon nanofibers have high strength and stiffness as well as unique thermal and electrical properties. The primary precursor used for the bulk production of carbon nanofibers is polyacrylonitrile (PAN). The most promising technique for the synthesis of carbon nanofibers is electrospinning, with PAN as the main polymer precursor. This dissertation deals with the fabrication of PAN-derived fibers via electrospinning followed by stabilization and carbonization in order to remove all non-carboneous materials and ensure pure carbon fibers as the resulting material. Prepared nanofiber films were placed on pre-preg composites and co-cured in a vacuum oven. The basic aim of this study was to fabricate lightweight and cost-effective PAN-derived electrospun fibers for SHM applications of composites and test them for durability under different conditions.

TABLE OF CONTENTS

Chapter	Page
1. INTRODUCTION.....	1
1.1 Literature Review.....	2
1.2 Use of Composites in Aircraft Structures	8
1.3 Structural Health Monitoring of Aerospace Composites	11
1.3.1 Conventional Resistance Strain Gauges	12
1.3.2 Fiber Optic Sensors	13
1.3.3 Development of Small-Diameter Optical Fibers and Fiber Bragg Sensors.....	19
1.3.4 Damage Detection by FBG Sensors	21
1.4 Piezoelectric Wafer Active Sensors.....	24
1.4.1 Piezoelectric Systems	24
1.4.2 Traveling-Wave PWAS Methods.....	28
1.4.3 Standing-Wave PWAS Methods.....	29
1.5 Electrically Sensitive Sensors.....	30
1.6 Electrospun Nanofiber-Based Sensors.....	31
1.6.1 Electrospun Nanofibers	31
1.6.2 Electrical Conductivity for Uniaxial Tests	33
1.6.3 PAN-Derived Carbon Nanofibers as Strain Gauges	34
1.7 References for Chapter 1.....	36
2. CARBONIZED ELECTROSPUN PAN NANOFIBERS AS HIGHLY SENSITIVE SENSORS IN STRUCTURAL HEALTH MONITORING OF COMPOSITE STRUCTURES	43
2.0 Abstract	43
2.1 Introduction	45
2.2 Experimental Materials and Methods	47
2.2.1 Materials	47
2.2.2 Fabrication and Carbonization of PAN Nanofibers	48
2.2.3 Strain-Sensing Tests for SHM	54
2.3 Results and Discussion.....	55
2.4 Conclusions	63
2.5 References for Chapter 2.....	64
3. THERMAL, ELECTRICAL, AND SURFACE HYDROPHOBIC PROPERTIES OF ELECTROSPUN POLYACRYLONITRILE NANOFIBERS FOR STRUCTURAL HEALTH MONITORING.....	67
3.0 Abstract	67

TABLE OF CONTENTS (continued)

Chapter	Page
3.1	Introduction69
3.2	PAN Electrospun Fibers as Strain Sensor in SHM Applications71
3.3	Experimental Materials and Methods73
3.3.1	Materials73
3.3.2	Carbonization of PAN Nanofibers74
3.3.3	Fabrication of Nanocomposite for Sensors.....76
3.4	Results and Discussion.....77
3.4.1	X-Ray Diffraction Analysis77
3.4.2	Fourier Transform Infrared Analysis.....81
3.4.3	Thermogravimetric Analysis.....84
3.4.4	Differential Scanning Calorimetry Analysis.....86
3.4.5	Ionic Conductivity Test88
3.4.6	Surface Hydrophobicity of Carbonized Fibers91
3.4.7	Thermal Behavior of Stabilized PAN Fibers96
3.4.8	Raman Spectra of Stabilized PAN and PAN Fibers.....98
3.5	Conclusions102
3.6	References for Chapter 3.....104
4.	MECHANICAL AND THERMAL PROPERTIES OF CARBONIZED PAN NANOFIBERS COHESIVELY ATTACHED TO SURFACE OF PREPREG CARBON COMPOSITE107
4.0	Abstract107
4.1	Introduction109
4.2	Experimental Materials and Methods111
4.2.1	Materials111
4.2.2	Fabrication of PAN Nanofibers112
4.2.3	Carbonization of PAN Nanofibers113
4.2.4	Nanocomposite Fabrication114
4.3	Results and Discussion.....115
4.3.1	Tensile Tests of PAN-Derived Carbon Nanofiber Composite115
4.3.2	Raman Spectrum of PAN-Derived Carbon Fiber Composite.....117
4.3.3	Thermogravimetric Analysis of PAN-Derived Carbon Fibers118
4.3.4	Dynamic Mechanical Analysis of PAN-Derived Carbon Fibers120
4.3.5	Differential Scanning Calorimetry of PAN-Derived Carbon Fibers.....125
4.3.6	Thermomechanical Analysis of PAN-Derived Carbon Fibers127
4.3.7	Energy-Dispersive X-Ray Analysis129
4.3.8	Thermomechanical Analysis.....130
4.3.9	Mechanical Properties of Pre-Preg Nanocomposite.....135
4.3.10	Thermal Analysis of PAN-Carbonized Fiber Composite.....136
4.4	Conclusions138

TABLE OF CONTENTS (continued)

Chapter	Page
4.5 References for Chapter 4.....	139
5. GENERAL CONCLUSIONS	144
6. FUTURE WORK	147

LIST OF FIGURES

Figure	Page
1.1 Schematics of SHM system in aircraft	6
1.2 Percentage of materials in 787-B	10
1.3 Fiber optic details: (a) total internal reflection principle; (b) optical fiber embedded in CFRP composite; (c) single-mode and multi-mode fibers	15
1.4 Schematic of fiber Bragg grating	17
1.5 Fiber Bragg grating mechanism: (a) light source transmitted through FBG, and narrow band reflected back, centered around Bragg wavelength; (b) shift of back-reflected band after external perturbations	18
1.6 Optical fiber: (a) small-diameter fiber; (b) fiber embedded in CFRP lamina; (c) small-diameter FBG sensor connected to conventional fiber	20
1.7 FBG sensor response to uniform and non-uniform strain distributions	21
1.8 Small-diameter FBG sensor embedded in -45° ply transverse crack detection in close vicinity of 90° ply of quasi-isotropic $[45/0/-45/90]_s$ laminate	22
1.9 Change in wavelength distribution in reflected light from FBG sensor due to crack	22
1.10 FBG sensor for determining edge delamination in $[45/-45/0/90]_s$ composite	23
1.11 Coupling between Lamb wave and piezoelectric wafer active sensor in thin-walled structure: (a) symmetric mode; (b) antisymmetric mode	25
1.12 Piezoelectric wafer active sensors: (a) 7 mm^2 PWASs on metallic structure; (b) 7 mm round and square PWASs on composite	26
1.13 PWAS for detection of damage with standing and propagating guided waves in thin-walled structures: (a) pitch-catch, (b) pulse-echo, (c) thickness mode, (d) impact and acoustic emission (AE) detection, (e) electromechanical (E/M) impedance, (f) PWAS phased array	27
1.14 Schematic of electrospinning process.....	31
1.15 Schematic of electrical conductivity testing done on pre-preg composite samples incorporated with carbonized PAN nanofibers under different strain rates	33

LIST OF FIGURES (continued)

Figure	Page
2.1 SEM images of electrospun PAN nanofibers: (a) before carbonization process; (b) after carbonization process	54
2.2 Schematic images of testing setups: (a) layup fabrication scheme of carbon fiber composite incorporated with carbonized PAN nanofibers; (b) specimen used in strain sensing	57
2.3 Curing cycle of carbon fiber pre-preg with carbonized PAN nanofiber mat.....	58
2.4 Experimental views of test setup for strain sensing response studies on prepared composite coupons	58
2.5 Engineering stress-strain curve for carbon fiber composites co-bonded with carbonized electrospun PAN nanofibers.....	60
2.6 Monotonic increment of stress vs. time of composite specimen co-bonded with	61
2.7 Strain vs. time curve of composite specimen co-bonded with carbonized electrospun PAN nanofibers	61
2.8 Change in voltage during loading of composite specimen co-bonded with carbonized electrospun PAN nanofibers	63
2.9 Change in resistance vs. time of composite specimen co-bonded with carbonized electrospun PAN nanofibers	65
2.10 Current (mA) vs. voltage (mV) of composite specimen co-bonded with carbonized electrospun PAN nanofibers	66
3.1 SEM images of PAN-derived carbon fibers: (a) electrospun; (b) after carbonization at 750°C for 1 hr; (c) after carbonization at 850°C for 1 hr; (d) after carbonization at 950°C for 1 hr.....	80
3.2 Heat treatment of carbonized fiber and conversion to carbon nanofibers by stabilizing in oxygen atmosphere at 270°C for 1 hr followed by carbonization at 750°C and 850°C	81
3.3 Experimental setup for strain sensor	82
3.4 XRD pattern of PAN pre-carbonized fibers: (a) at 750°C; (b) at 850°C; (c) at 950°C.....	84

LIST OF FIGURES (continued)

Figure	Page
3.5 FTIR spectra of PAN fibers prior to carbonization	86
3.6 FTIR spectra of PAN fibers carbonized at 750°C, 850°C, and 950°C.....	87
3.7 TGA curves of PAN fibers prior to carbonization	89
3.8 DSC thermogram of PAN fibers for heat flow, non-rev heat flow and rev heat flow	90
3.9 Experimental setup for electrochemical measurement (Gamry Instruments) of ionic conductivity.....	93
3.10 Experimental setup for water drop capture.....	96
3.11 Water contact angle of pre-carbonized PAN fibers at different temperatures of 750°C, 850°C, and 950°C	97
3.12 Results of tensile tests for carbonized PAN nanocomposite fibers at different temperatures of 750°C, 850°C, and 950°C.....	98
3.13 DSC thermograms of bulk PAN fibers.....	99
3.14 DSC thermograms of stabilized PAN fibers.....	100
3.15 Raman spectrum of carbonized bulk PAN polymer.....	101
3.16 Raman spectra of PAN fibers carbonized at 750°C.....	103
3.17 Raman spectra of PAN fibers carbonized at 850°C.....	104
3.18 Raman spectra of PAN fibers carbonized at 950°C.....	104
3.19 Stress vs. strain behavior of carbon fiber composites with carbonized electrospun PAN nanofibers	105
3.20 Contact angle measurements of PAN samples after carbonization at 750°C, 850°C, and 950°C.....	107
4.1 SEM images of PAN fibers: (a) before carbonization, (b) after carbonization	119
4.2 Fabrication of PAN-derived carbonized nanofiber composite.....	121

LIST OF FIGURES (continued)

Figure	Page
4.3 Engineering stress-strain curve for PAN-derived carbonized nanofiber composite	122
4.4 Raman spectrum of carbonized PAN nanofiber.....	124
4.5 Thermogravimetric curves of PAN-derived carbon fiber composites.....	126
4.6 Specimen mounted in DMA three-point bending fixture	127
4.7 DMA curves of storage modulus, loss modulus, and $\tan \delta$ of carbonized PAN nanocomposite fibers.....	128
4.8 Storage modulus (E') curves as function of temperature for pre-preg carbonized nanofibers, composite complex viscosity as a function of temperature, and change in system compliance as function of force level up to 6 N.....	129
4.9 DSC thermogram curves of carbonized PAN nanocomposite fibers at 850°C.....	132
4.10 Schematics of TMA used in this study	135
4.11 TMA curves of CTE, thermal expansion of carbonized nanofiber-reinforced composite in 0° direction	135
4.12 Carbonized PAN fibers: (a) SEM image; (b) results of EDX analysis	136
4.13 Thermal expansion of composites: (a) 3-D mesh surface generated by MATLAB; (b) CTE curves of prepreg nanocomposites with 0° plies orientation.....	138
4.14 Thermal expansion of composites: (a) 3-D mesh surface generated by MATLAB; (b) CTE curves of prepreg nanocomposites at 90° plies orientation.....	139
4.15 Stress analysis of prepreg composites incorporated with carbonized PAN nanofibers as top layers using ANSYS analysis.	142
4.16 Thermal analysis: (a) dimensions of prepreg composites incorporated with carbonized PAN nanofibers as top layers; (b) steady-state from ANSYS analysis.	144
4.17 Steady-state thermal analysis of carbonized PAN nanofibers using ANSYS simulation.....	144

LIST OF TABLES

Table	Page
1.1 Electrical Conductivity K Ms/Cm for Indicated Concentration in Mass Percent	35
2.1 Characteristics of Epoxy Resin System for Pre-Preg Carbon Fibers (5320-1).....	52
2.2 Properties of Carbonized Electrospun PAN Nanofibers	55
2.3 Recommended Cure Cycles for Pre-Preg Carbon Fibers (5320-1).....	55
2.4 Tensile Properties of 5320-1 Epoxy Resin System.....	56
3.1 Structure Parameters Determined by X-Ray Diffraction for PAN Carbon Fibers.....	85
3.2 Conductivity Values of Carbonized PAN Fibers at 850°C.....	94
3.3 Water Contact Angle Values for Electrospun Carbonized PAN Fibers.....	95
3.4 Mechanical Properties of PAN-Derived Carbon Fiber Composites	99
3.5 Properties of Carbonized Electrospun PAN Nanofibers on Prepreg Composite	105
4.1 Quantity Analysis of Elements in Carbonized PAN Nanofibers.	137
4.2 Average Linear Thermal Expansion Coefficient of Prepreg Carbon Nanocomposites at 0° Orientation.....	140
4.3 Average Linear Thermal Expansion Coefficient of Prepreg Carbon Nanocomposites at 90° Orientation.....	140
4.4 Mechanical Properties of Prepreg Composites Incorporated with Carbonized PAN Nanofibers as Top Layers	143

LIST OF ABBREVIATIONS

AE	Acoustic Emission
ANSI	American National Standard Institution
CFRP	Carbon Fiber-Reinforced Plastic
C-N	Carbon-Nitrogen
CTE	Coefficient of Thermal Expansion
DI	Deionized
DMA	Dynamic Mechanical Analysis
DMF	Dimethylformamide
DSC	Differential Scanning Calorimetry
EDX	Energy-Dispersive X-Ray
E/M	Electromechanical
FBG	Fiber Bragg Grating
FTIR	Fourier Transform Infrared
GFRP	Glass Fiber-Reinforced Polymer
HCl	Hydrochloric Acid
IEEE	Institute of Electrical and Electronics Engineers
MEMS	Microelectromechanical System
MTS	Machine Tensile Stress
MWCNT	Multi-Walled Carbon Nanotube
NDT	Non-Destructive Testing
PAN	Polyacrylonitrile
PEEK	Polyetheretherketone

LIST OF ABBREVIATIONS (continued)

PEO	Polyethylene Oxide
PPS	Polyphenylene Sulfide
PVA	Polyvinyl Alcohol
PVDF	Polyvinylidene Difluoride
PWAS	Piezoelectric Wafer Active Sensor
SEM	Scanning Electron Microscopy
SHM	Structural Health Monitoring
T_g	Glass Transition Temperature
TGA	Thermogravimetric Analysis
T_m	Melting Temperature
TMA	Thermomechanical Analysis
UV	Ultraviolet
wt%	Weight Percent
XRD	X-Ray Diffraction

LIST OF SYMBOLS

$^{\circ}$	Degree
λ	Wavelength
c	Speed of Light (3.00×10^8 m/s)
e^{-}	Electron
eV	Electron Volt (Unit of Energy)
h	Planck's Constant (6.63×10^{-34} J.s.)
h^{+}	Hole
μm	Micrometer
(n)	Effective Refractive Index
(Λ)	Periodic Variation
(ΔT)	Temperature changes
(λ_B)	Bragg Wavelength
S_{ij}	Mechanical Stress
T_{kl}	Mechanical Strain
E_k	Electrical Field
D_j	Electrical Displacement
S_{ijkl}^E	Mechanical Compliance
ϵ_{jk}^T	Dielectric Constant
d_{jkl}	Piezoelectric Coupling
(E_3)	Electric Field

CHAPTER 1

INTRODUCTION

1.1 Literature Review

Structural health monitoring (SHM) has become an important topic of interest recently, because of the growing demand for innovative approaches to preventing damage in large infrastructures. SHM is a methodology adopted for the full-scale investigation of many kinds of damage pertaining to the continuous fitness of infrastructures under gradual or sudden changes in their state, in order to learn about either the response mechanism or load. SHM is a scientific methodology of nondestructively pinpointing the health conditions of infrastructures, such as operational and environmental loads, damages, the growth mechanism of damages, and the prediction of future performance of structures, because damages accumulate and can subsequently cause catastrophic failure. SHM is a scientific methodology of determining the ability of the structure to continue unabatedly to perform its intended functionality. Government agencies and private companies spend billions of dollars annually on the maintenance of plant equipment, facilities, tunnels, and bridges. Similarly, the maintenance and repair of commercial aircraft cost companies enormous amounts of money each year. The ever-increasing expense involving aging infrastructures has become a challenging issue and demands immediate attention.

The implementation of a damage identification strategy for all kinds of engineering infrastructures is commonly referred to as structural health monitoring [1]. SHM is a technique of establishing some knowledge of the existing conditions of an infrastructure with the objective of determining its current location and extent of damage. SMH has vast potential for applications

in the real-time monitoring of offshore, aerospace, and building infrastructures subjected to corrosion, creep, fatigue, impact, and dynamic loads. This process involves the observation of a structure or mechanical system over time based on periodically spaced measurements and statistical analysis of these measurements to monitor the current state of a system's health [1]. The fundamental idea of SHM is to build a system similar to the human nervous system. When more nerves (sensors) are placed close to critical organs (critical structural components), the real-time dependent information about the health of the organ (structural component) can be ascertained, and appropriate action can be taken to ensure excellent service performance. Over time, the output of this process is periodically updated and monitored in order to determine the performance of a structural component, especially under aging and damage accumulation resulting from the operating environment [1]. Under extreme circumstances, such as during an earthquake, SHM is used for rapid condition screening. The purpose of this screening is to ascertain information on a real-time basis about system performance under such extreme circumstances and the subsequent integrity of the system [1].

Damage is the change in the material and/or geometrical properties of an infrastructure under service, including changes to system connectivity and boundary conditions, which deleteriously affect the performance of a system [1]. All materials have some initial flaws, and under appropriate loading conditions, these flaws grow and coalesce to a point where the failure of a component occurs, or component-level failure occurs. Further loading at this point may cause failure of another structural component, which can lead to system-level failure. Damage often occurs in many engineering systems during their service life. Such damage generally occurs for many reasons, such as excessive loads, crack growth, unexpected extra loads, and

sudden impact by a foreign object. For whatever reason, damage is detrimental to infrastructures and under severe operating conditions or prolonged service life may result in catastrophic failure. In order to ensure excellent system performance, the integrity of components, structural safety, and minimum maintenance cost, SHM offers a reliable, efficient, and cost-effective methodology to monitor system performance, detect and monitor defects, diagnose the structural health conditions, and take appropriate action regarding the safety of infrastructures.

All damage begins at the material level, is commonly referred to as defects or flaws, and is present to some degree in almost all materials [1]. Under appropriate loadings, these defects or flaws continue to grow and coalesce, and eventually cause component damage and subsequently system-level damage [1]. Damage does not necessarily mean a complete loss of functionality of a system, but rather the system loses its maximum operating capacity [1]. The damage continues to grow to a point where it becomes almost impossible for the system to be operative. This point is typically referred to as failure. In terms of timescale, damage can accumulate incrementally over a long period of time until a cataclysmic failure occurs [1]. On the other hand, in a relatively short timescale, damage can result from scheduled service events such as aircraft landings and take offs. The interest in SHM and its corresponding advantage for pronouncing life-safety and economic benefits have spurred the need for investigation [1]. Almost all materials contain flaws, and under operating conditions, these flaws play an important role in unexpected failure. SHM is an effective technique to monitor these flaws in aging infrastructures and at the same time provide financial benefits by reducing the cost of scheduled maintenance and the life-cycle of these materials and devices, and increasing their safety and reliability.

One of the primary ideas behind SHM technology is to monitor any structural changes on the infrastructure with time and take proper steps to avoid catastrophic failure. Owing to the economic benefits and effectiveness of SHM, this type of monitoring has become a topic of much recent interest and numerous research activities. The growing demand of SHM makes it worthy of innovative approaches to prevent damage to infrastructures by developing a damage identification strategy for all kinds of infrastructures.

Every year, the U.S. government spends billions of dollars on the maintenance of plant equipment, facilities, and bridges. Similarly, the maintenance and repair of commercial aircraft costs a considerable amount of money every year [2]. The ever-increasing cost of aging infrastructures has become a challenging issue and demands immediate attention. SHM is an effective technique for ensuring the safety of infrastructures and at the same time providing financial benefits. SHM reduces the costs of maintenance and the life-cycle. The purpose of SHM is to monitor changes in the infrastructure on a real-time basis and take expedient measures to avoid catastrophic failure. SHM allows engineers to employ the sensing of structural responses corresponding to various stress conditions under service in conjunction with appropriate data compilation and model-updating techniques. The aim of SHM is to monitor effectively infrastructure damage and take preemptive measures prior to any catastrophic failure. SHM ensures safety and reliability while reducing maintenance costs. SHM reduces maintenance and repair costs by replacing the scheduled maintenance with a needed maintenance, thereby reducing the cost of unwanted maintenance and eliminating the need for unscheduled maintenance [2]. Owing to the economic benefits and effectiveness of SHM, this method has become a topic of growing interest, and numerous research papers are being published.

All material contains flaws of some kind, and under operating conditions, these flaws play an important role in its failure. The detection of flaws and monitoring them on a continuous and routine basis is known as structural health monitoring. SHM employs the use of sensors that can be placed in structures to monitor any malfunctioning in either an active or a passive way [2]. These sensors are lightweight, affordable, and unobstructive to the functioning of structures.

SHM determines the state of structural health and uses appropriate data processing to access the remaining life of a structure. Many civil and aerospace infrastructures are at risk since they are beyond their expected/designed lifetimes. However, it is expected that they will remain in service an extended period of time [2]. Many physical structures in the world have become deficient or functionally obsolete and in need of immediate attention. Their repair or maintenance will cost billions of dollars. The costs associated with aging infrastructures have become a major obstacle. The increasing age of infrastructures makes the cost of their maintenance a challenge. SHM replaces scheduled maintenance with needed maintenance, thus eliminating the cost of scheduled maintenance and also preventing unscheduled maintenance [2]. SHM is the enabling technology that will allow old infrastructures to function properly for an extended period of time through an appropriate warning system before catastrophic failure.

SHM outlines the issues associated with aging aerospace and civil structures, which is a major challenge for the engineering community. SHM replaces scheduled maintenance with needed and condition-based maintenance [2]. Condition-based maintenance via SHM generally increases availability and reliability, and decreases maintenance costs while maintaining safety. SHM eliminates unnecessary inspections, minimizes the inspection cost, and provides accurate information about the life of structural components. Another application of SHM is the

installation of new sensors and associated sensory equipment in new structures [2]. Figure 1.1 shows a schematic representation of an SHM system in an aircraft.

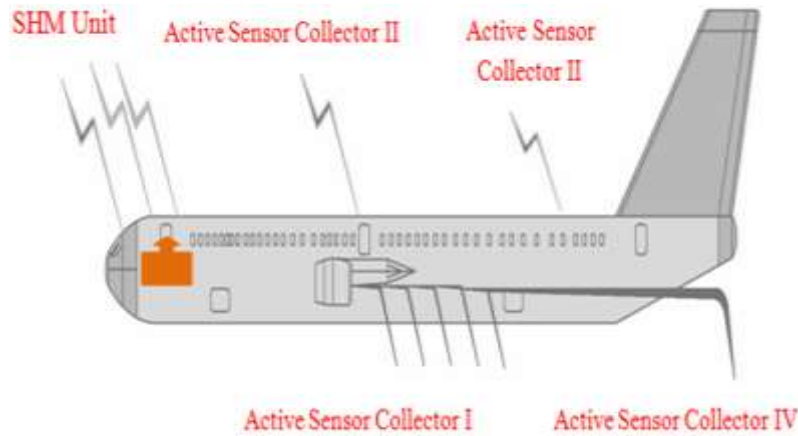


Figure 1.1. Schematics of SHM system in aircraft.

As mentioned previously, SHM system can be performed by either a passive or an active approach. Active SHM (Figure 1.1) detects damage directly by installing sensors on structures that can provide data pertaining to flaws so that needed action can be taken immediately [2]. Passive SHM is related to measuring various operational parameters and then estimating the SHM condition from these parameters. For instance, various flight parameters, such as airspeed, turbulence, stress in critical parts, fatigue life of critical components, and vibration levels, could be monitored, and then algorithms could be designed to conclude how much life of the aircraft has been used up and how much life is remaining [2].

The detection of flaws and their monitoring and maintenance in a routine and systematic manner in order to prevent any catastrophic failure is a major concern of SHM. A wide variety of smart materials for practical applications in SHM has been developed by many researchers [2]. The rapid growth of nanotechnology has permitted the manipulation of matter at a molecular level, which provides the building blocks of smart materials [2]. Smart materials developed via

nanotechnology have the ability to significantly improve the measurement and monitoring motion in devices in nanoscale [3]. There is a growing need for monitoring the structural health and identification of damage in infrastructures before any catastrophic event, which will cost billions of dollars and loss of valuable lives [4]. Recently, there has been a drastic interest in this new topic due to the significant benefits of SHM for improving the safety of critical structural components and potential for economic savings [4].

The abundant use of composite materials in civil and military aviation vehicles demand that SHM be used for continuous monitoring of defects and cracks in critical structural components in order to ensure safety and excellent performance. For large commercial aircraft structures, certification of safety use has become a challenging task, which highlights the importance of embedded sensors that can be regularly inspected and provide important information about the structures without the need for removal of a component [4]. Currently, the cost of inspection is extremely high, especially for large aircraft structures, which signifies the need for a low-cost inspection solution that can help in providing real-time monitoring and inspection data for SHM applications. Several passive and active technologies are available for real-time, continuous monitoring of composite structures for SHM applications such as piezoelectric wafer active sensors (PWASs) and optical sensors laminated in the composite structure [4]. Factors that must be considered before selecting a technology for SHM applications are low cost, large-area processability, seamless integration with the composite structure, and ease of signal detection and processing [4]. Considering the cost and large-area integration with the composite structure in these technologies, electron polyacrylonitrile (PAN) fibers are promising candidates in strain sensors in composite structures. Recently, there has been

significant interest in strain sensing by using polymer nanocomposites due to their unique properties [3].

1.2 Use of Composites in Aircraft Structures

Composite materials consist of fiber-reinforcement materials bonded together with a matrix material. Composite materials exhibit excellent physical and chemical properties that include lightweight, stiffness, corrosion resistance, and resistance to chemical attack. The stiffness and strength of composite materials can be changed in the direction of fiber loading. Composite materials are being used extensively in aircraft structures (Airbus A380, B787, Typhoon, F35) due to their excellent properties [5]. The use of composites in commercial and military aircraft has increased significantly over the past three decades.

Although commercial airlines are concerned with fuel economy and reduced production and maintenance costs, ease in assembly has been a major issue in switching over to composites. The traditional materials for aircraft construction are steel, titanium, and aluminum. Composites do not corrode like metals. In commercial aircraft, the corrosion and fatigue cracking is a major problem in the aluminum fuselage structure. The replacement of parts with composites is relatively easy; therefore, composite parts are being extensively used as replacements for metallic parts in older airplanes. Aircraft parts made from composite materials include the spoiler, interior design, flight controls, fairings, landing gear doors, panels, floor beams and floor boards, fuselage, propellers, turbine engine fan blades, stabilizers, etc. Composites are also widely used in aircraft interiors to create luggage compartments, sidewalls, ceilings, cargo liners bulkheads, floor, electronics, and seatings. The most significant application of advanced composites in aircraft structures is their usage in highly loaded parts with gauges, areas

susceptible to corrosion such as the fuselage, high-fatigue load parts such as wings and fuselages, and weight reduction areas such as fuselages and wings.

Composite materials were developed two to three decades ago with the purpose of weight savings over aluminum parts. Composite materials are being used extensively for primary structures in commercial and military aerospace. Previously, the Boeing 787 (2011) and the Airbus A350XWB (2013), all major commercial carriers, were using 3 to 5 weight percent (wt%) of composites in their structures, compared to the total structural weight. However, in the near future, carbon fiber-reinforced plastics (CFRPs) will contribute to around 50% of the weight of aircraft. A major aircraft manufacturer has successfully tested CFRPs as a stabilizer and as an airbrake. The excessive use of composite materials in aircraft allows for a lightweight, corrosive-, chemical-, and fatigue-resistant next-generation high-performance economical aircraft design to materialize. In addition to these advantages, composites present some disadvantages, such as low fracture toughness and moisture absorption [6]. Since the service of the Boeing 787 in 2011 and the Airbus A350XWB in 2013, CFRPs have become common structural materials for commercial aircraft [8], as shown in Figure 1.2. The weight ratio of composites used in commercial carriers is around 50% corresponding to a volume ratio of about 70% [7, 8]. The Boeing 787 has increased its composite materials for airframes to 39%, while the Boeing 787-B uses only 11% composite materials [11].

Advanced composites used in the aerospace industry are composed of carbon fibers, polyphenylene sulfide (PPS), polyetheretherketone (PEEK), and epoxy [8]. CFRPs have higher specific strength and stiffness than many other materials, hence the reason for their excessive use in aircraft structures. The laminated composite structures are reinforced in specific directions,

and there is no reinforcement in the through-the-thickness direction [8]. Although, composites have been used in the aerospace industry for the last 30 years, the interlaminar strength of laminated composite structures is still one of the design's limiting factors [9]. Improving the interlaminar fracture toughness is extremely important in aircraft structure [8]. However, special interlayer-toughened laminates are used in the fuselage and wings of aircraft [8, 10]. Composite material-based aircraft allow for less fuel consumption, high efficiency, and reduced operating costs. Since composites contain different phases (fibers and matrix), they display different types of damages under service with different propagation characteristics [5]. The detection of flaws in composites and estimating the remaining life cycle of composite structures is a challenging issue.

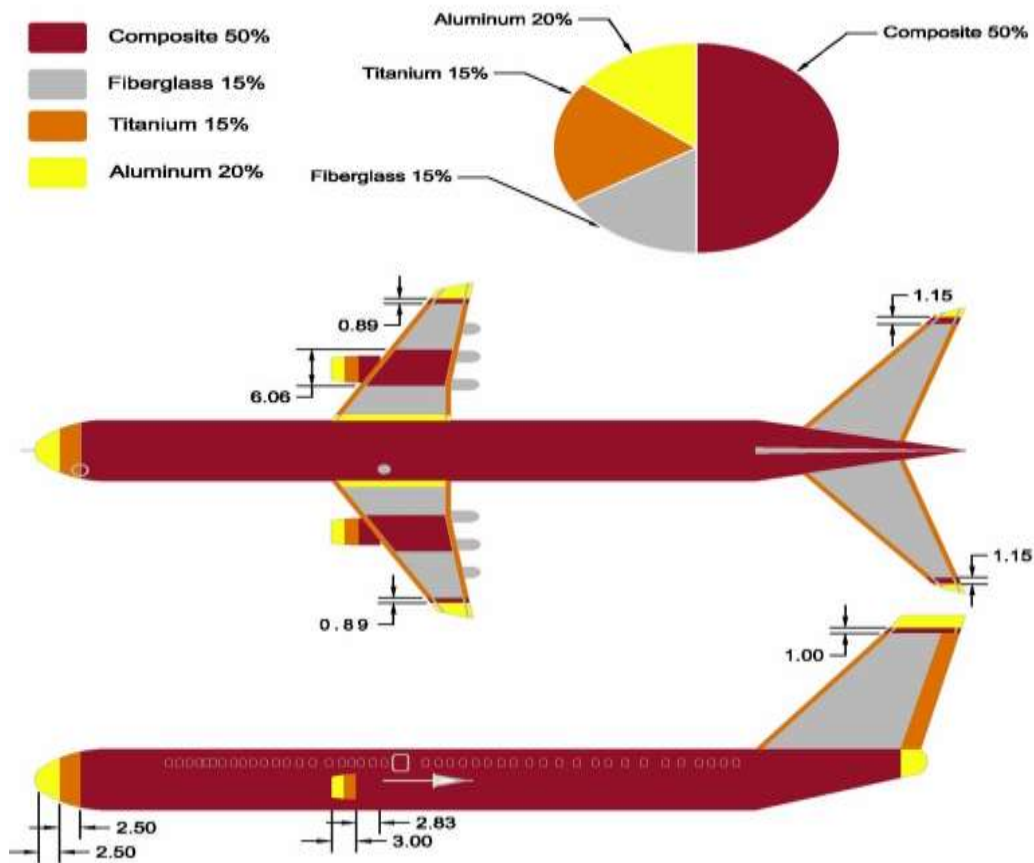


Figure 1.2. Percentage of materials in Boeing 787-B.

The common damage in composite structures is caused by an impact that results in degradation of the mechanical properties [5]. This type of impact can cause cracking in the matrix, delamination, and broken fibers, which results in reduced fatigue life and strength [5, 7]. In sandwich structures, impact damage causes delamination between the skin and the foam. Some studies have shown that a material with high stiffness can arrest cracks in sandwich structures [8]. In other studies, a novel through-the-thickness reinforcement technique for CFRP laminates has been outlined [8]. These studies have shown that in-plane yarns entangled with each other in the thickness direction improve the interlaminar strength [8].

Composites are anisotropic, and their strength and stiffness can be tailored to the load direction, which may result in less damage tolerance in some regions directly on the structure [11]. It is expected that some defects can initiate in these regions under critical service conditions. However, very little is known about service defects in structural composites compared to metals since composites are relatively new. Therefore, non-destructive testing (NDT) of the composite structure is important for preventing failure in composite structures [11].

1.3 Structural Health Monitoring of Aerospace Composites

Almost all government and private industries are interested in imposing the SHM strategy in their infrastructures in order to detect damage as early as possible. However, such detection needs some form of SHM and is motivated by the potential life-safety and economic impact of this technology [1]. SHM technology depends on sensors that are permanently embedded in the structure and monitor its performance over time in either a passive or an active way [12]. These sensors are lightweight, inexpensive, unobtrusive, and not harmful to the structure. SHM technologies have been studied extensively in order to ensure the safety and durability of

composite structures in aircraft. CFRP laminates are largely being used for primary aircraft structures, but their maintenance cost is relatively high due to their complicated structure [13]. Sensors that are typically used in SHM applications and can operate in dynamic and static areas [1] are the following [12]:

- Conventional resistance strain gauges
- Fiber optic sensors (fiber Bragg grating [FBG] sensors)
- Piezoelectric wafer active sensors
- Electrical property sensors
- Electrospun PAN-derived carbon fibers as strain sensors

Other damage-estimation methods based on large-area measurements are scanning Doppler laser velocimetry, thermography, and ultrasonic C-scan. Strain sensors are having a wide range of applications in almost all industries for measuring different quantities, such as stress, pressure, and vibrations.

1.3.1 Conventional Resistance Strain Gauges

Various methods are used to measure force and moments electrically, all of which depend on amplifying the effects that small deflections have on resistance, inductance, or capacitance of a system [14]. The theory of resistance strain gauges is based on the fact that all materials offer resistance to electricity, which can be measured by a multimeter [14]. The conventional resistance strain gauge is a strain-sensitive component embedded into a structure in order to measure strain [14, 15]. When the gauge is strained, its resistance is proportional to strain [14]. Strain can be determined by measuring the change in electrical resistance [14, 15]. The strain-induced resistance change can be due to the geometric effect or by the piezo-resistive effect

exhibited by some materials [2]. The resistance strain gauge is also used in the field of stress analysis. Here, it works on the principle that electrical resistance changes when the specimen is either stressed or compressed. Resistance strain gauges can operate in both static and dynamic regimes [2]. Strain gauge technology is very well developed and has been used for a long time; however, some problems are associated with these gauges. For example, various environmental conditions may have an adverse effect on the electrical wire connections that may cause strain drift or even signal loss [2]. Despite the fact that conventional strain gauges possess excellent properties, they also possess some limitations relative to their measurement range, low sensitivity, and problems associated with their embedment in structural components.

1.3.2 Fiber Optic Sensors

Fiber optic sensor technology offers the possibility of sensing different parameters such as strain, temperature, and pressure in a harsh environment and remote locations. Fiber optic sensors have many advantages over conventional sensors, and today they are considered an important component in improving industrial processes, quality control systems, and preventing and controlling general process abnormalities. The uses for optical fibers have been expanding rapidly in recent years. All aircraft operators are encountering problems regarding the extension of service life of aircraft beyond their designed lifecycle, resulting in heavy maintenance and inspection costs [16]. SHM based on advanced sensor technology is a cost-effective approach to addressing this issue by reducing the cost of maintenance and inspection [16]. Fiber optic sensor technology has undergone outstanding growth since its inception in the early 1970s with laboratory demonstrations of fiber optic gyros and acoustic sensors and the introduction of

spectrally based sensors [17]. Fiber optic technology was developed to provide the capability of SHM of aircraft because of its outstanding features.

Recently, SHM applications use optical fibers [13] that have enough flexibility, heat resistance, and strength to be embedded easily into composite structures for monitoring applications [13]. A useful candidate for a monitoring device is an optical fiber Bragg grating sensor [13, 18]. FBG sensors are sensitive to the non-uniform distribution of strains, thereby detecting damage that causes non-uniform strain distribution in CFRP laminates [13]. FBG is a region of periodic refractive index perturbation inscribed inside the core of an optical fiber, thus diffracting the propagating optical signal at some specific wavelengths. Optical fibers may cause degradation in the mechanical properties of laminates, thereby resulting in a reduction of strength in composites [13]. Recently invented small-diameter optical fibers together with the FBG sensor do not cause any degradation in composite laminates [13, 19]. Fiber optic sensors offer significant advantages for SHM applications such as corrosion resistance and immunity to electromagnetic interference [2].

In an optical fiber, a central core is surrounded by an annular cladding and a protective coating, as shown in Figure 1.3 [15]. Light is injected and then guided by a dielectric cylinder core surrounded by dielectric cladding [14]. Since cladding has a lower refractive index than the core, the light wave is confined to the core and can travel long distances with little loss, as shown in Figure 1.3(a) [15]. Snell's law states that reflection depends on an angle derived as a function of the index ratio, which is known as the critical angle [14]. When the critical angle is not exceeded, the light remains at the core of the optical fiber and will be reflected [14]. However, if the critical angle is exceeded, then the light will not reflect, and will be lost and absorbed into the

cladding [14]. The purpose of the optical fiber is to behave as a waveguide for light and its energy [14].

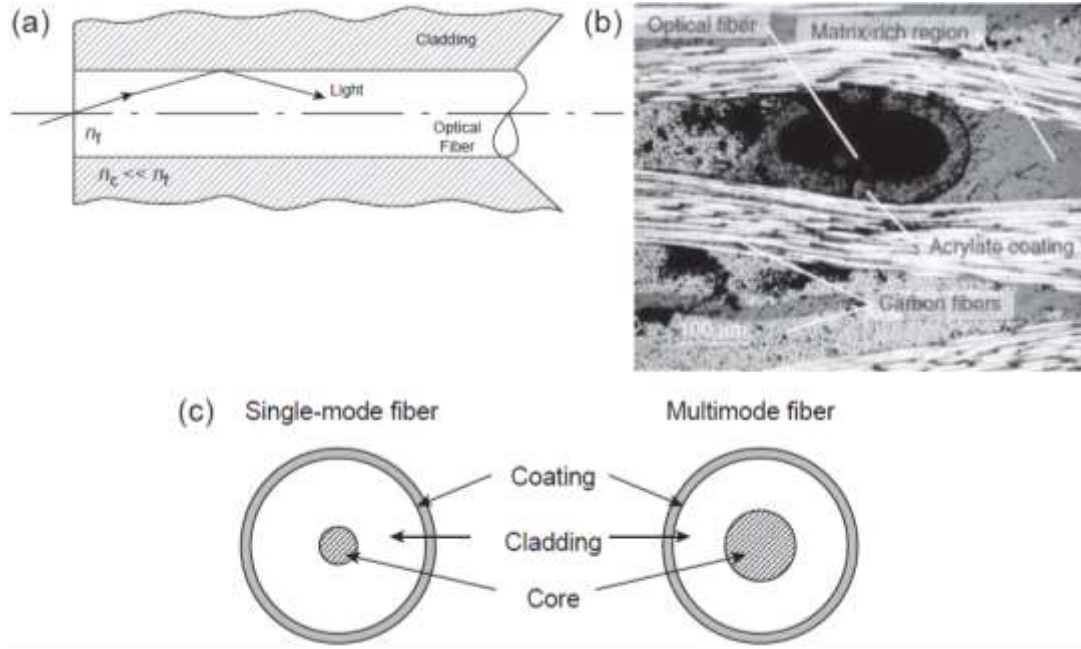


Figure 1.3. Fiber optic details: (a) total internal reflection principle; (b) optical fiber embedded in CFRP composite; (c) single-mode and multi-mode fibers [20].

The diameter of the optical fiber generally varies between 120 and 250 μm . Optical fibers create discontinuity when embedded in a composite, as shown in Figure 1.3(b) [20]. However, fiber optics with a diameter of 52 μm for embedding into composites have also been reported in the literature [15, 20]. Single-mode fibers have a 10 μm core and can accommodate only the fundamental guided light wave model [2]. Multi-mode fibers, as shown in Figure 1.3(c), generally have cores up to 100 μm and allow for the propagation of multiple modes [15]. Both single-mode and multi-mode optical fibers are constructed using a fiber optics sensor [15]. However, a single-mode optical fiber is more strain sensitive due to its small core size [15]. In 1969, Nippon Sheet Glass and Nippon Electric Cooperative manufactured the first gradient index

fiber for telecommunication applications [21]. Ken O. Hill determined the effect of photosensitivity on Germanium-doped fibers, which, when exposed to UV light, induce a permanent change in the refractive index [21]. This effect was used to write Bragg gratings on fibers, which can reflect small wavelength peaks. The wavelengths of these peaks change when the fibers are strained. FBGs match very well with composites like glass and carbon fiber-reinforced composites. They can be integrated into composites or can be fixed or used as patches on composite surfaces [21]. FBGs can measure high strain ($>10,000 \mu\text{m/m}$) and, therefore, are very well suited to measure high strains. They are lightweight, small in size, and immune to electromagnetic interference. FBGs are a fiber optic passive component displaying fundamental attributes of reflection and filtration. They can operate up to 50 km in distance and cryogenic conditions [21].

Fiber Bragg gratings can be written in a single-mode optical fiber. The core of the fiber has a high refractive index due to Germanium doping, and the outer part (cladding) is made of pure glass (SiO_2) with a diameter of $125 \mu\text{m}$. The differences in refractive indexes between the core and the cladding cause light to propagate inside the core. In order to obtain the Bragg gratings on the fiber core, the fiber should be free from the coating, but then after writing the Bragg gratings, the core should be coated [21]. To measure the strain, the sensor should be embedded into the composite structure. Stretching a fiber optic Bragg sensor results in the change of a considerable period, which causes an alteration in the wavelength of the reflected UV light. The reflected wavelength of Bragg gratings is very small in bandwidth (peaks in the spectrum) [21]. The operation principle of an FBG sensor for monitoring based on the

wavelength of the returned “Bragg” signal shifts with changes in the measured strain [23]. The Bragg wavelength can be given by [22, 23]

$$\lambda_B = 2n\Lambda \quad (1.1)$$

where Λ is the grating pitch, and n is the effective of the core [23]. Figure 1.4 shows a schematic of fiber Bragg grating.

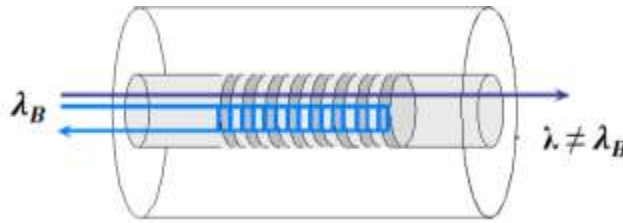


Figure 1.4. Schematic of fiber Bragg grating.

FBG is a periodic longitudinal variation of the refractive index in the core of an optical fiber, and the spacing of variation can be determined by the wavelength of the reflected light. FBG indicates a particular wavelength of light and transmission of all others. The Bragg condition can be fulfilled when two requirements—frequency of incident and reflected radiation—are the same, and the sum of the incident wave vector and the grating vector is equal to the wave vector of the scattered radiation. FBG involves the spatially periodic variation of the refractive index along the fiber’s core in a short segment of a single-mode optical fiber with a cladding diameter of 125 μm [19]. As shown in Figure 1.5(a), when light from a broadband source is injected into an optical fiber containing FBG, a narrowband spectral component at the Bragg wavelength is reflected back by the grating, which depends on the periodic variation (Λ) of the FBG and the effective refractive index (n) [19]. When the FBG sensor is subjected to mechanical perturbations, the back-reflection peak wavelength is shifted according to the extent

of the perturbations influenced by the FBG sensor, which is sensitive to axial strain, as shown in Figure 1.5(b) [19]. The axial strain influences the response caused by the FBG sensor through compression and expansion changes in the spacing of periodic variation and through the effective index of the optical fiber [19].

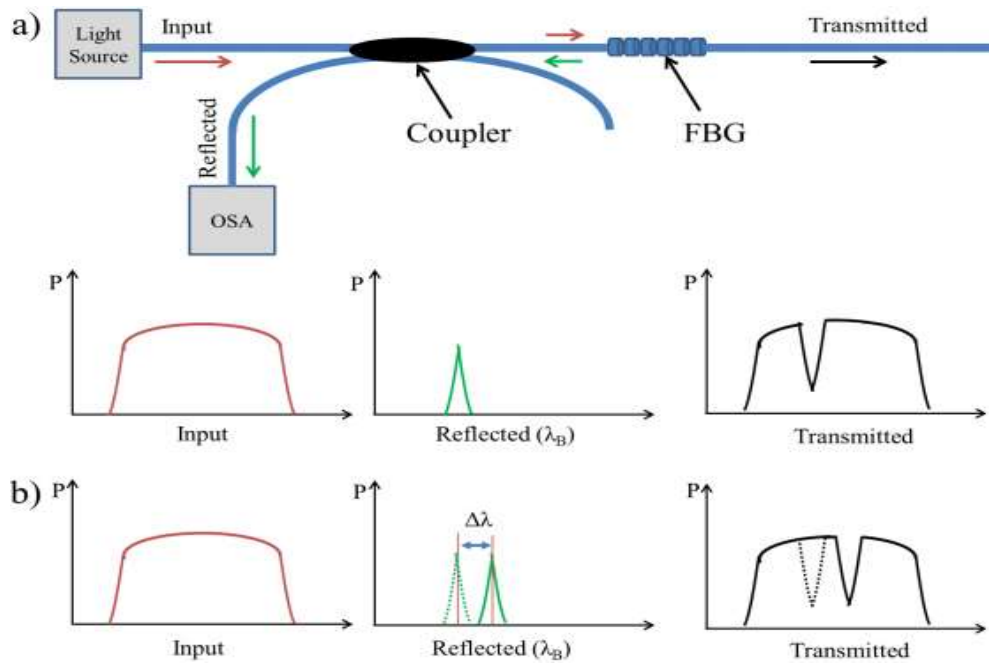


Figure 1.5. Fiber Bragg grating mechanism: (a) light source transmitted through FBG, and narrow band reflected back, centered around Bragg wavelength; (b) shift of back-reflected band after external perturbations [19].

Temperature changes (ΔT) influence the grating period and refractive index, thereby changing the Bragg wavelength [19]. The strain, ambient temperature, grating period, and refractive index are related as follows [19]:

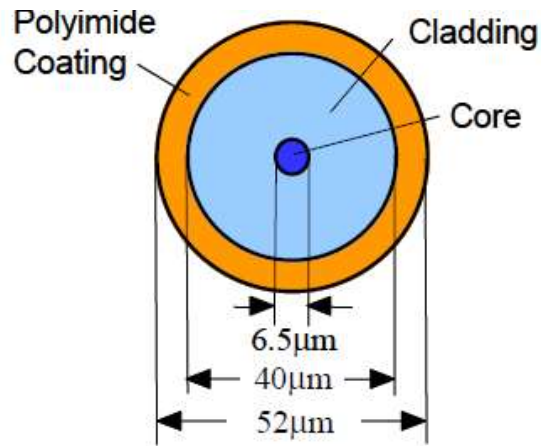
$$\Delta\lambda_B = 2 \left[\Lambda \frac{\partial n}{\partial l} + n \frac{\partial \Lambda}{\partial l} \right] \Delta l + 2 \left[\Lambda \frac{\partial n}{\partial T} + n \frac{\partial \Lambda}{\partial T} \right] \Delta T \quad (1.2)$$

where Δl is the change in FBG length due to strain, and ΔT is the change in temperature [19]. In order to determine the Bragg wavelength (λ_B), an optical spectrum analyzer is generally employed when experiments are done inside the laboratory [19]. However, when experiments are done outside the laboratory, a special kind of interrogator is generally used [19]. When high-speed interrogators are employed, FBG sensors are more suitable for monitoring strains [19].

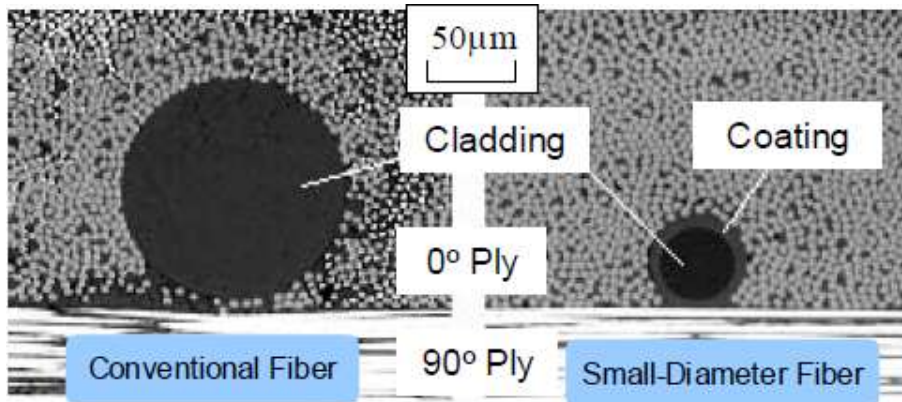
1.3.3 Development of Small-Diameter Optical Fibers and Fiber Bragg Grating Sensors

Figure 1.6 shows a small-diameter optical fiber (both single-mode and multi-mode) and FBG sensor used with this type of fiber. The optical fiber with cladding has a diameter of 40 μm , and the optical fiber with a polyimide coating has a diameter of 52 μm , which can be easily embedded within one CFRP ply of 125 μm thickness [13].

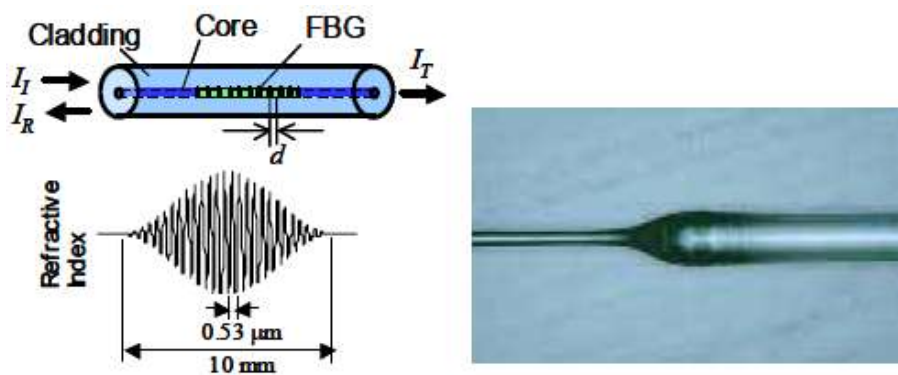
Such optical fibers do not cause any significant reduction in the strength of composite materials when embedded parallel to reinforcement [13]. When a small-diameter optical fiber is embedded parallel to the laminates, the resin-rich region cannot be found in the vicinity of optical fibers, as shown in Figure 1.6(b) [13]. The polyimide coating prevents stress concentration around the cladding and thereby helps in maintaining strength and stiffness of the composite [13]. The coating is highly compatible with epoxy and other resins used in CFRP composites under high-temperature exposure [13]. When a broadband of light is injected from one end of the fiber, a narrow band of the light spectrum having a sharp wavelength corresponding to the grating variation is observed [13]. FBG sensors are generally used to determine strain and temperature through a shift in the wavelength peak [13].



(a)



(b)



(c)

Figure 1.6. Optical fiber: (a) small-diameter fiber [11]; (b) fiber embedded in CFRP lamina; (c) small-diameter FBG sensor connected to conventional fiber [13].

1.3.4 Damage Detection by FBG Sensors

FBG sensors are sensitive to non-uniform strain distribution, and the light reflection spectrum becomes broadband from the FBG sensor (Figure 1.7) [11]. Microscopic damages due to non-uniform strain distribution in CFRP laminates can be determined using the sensitive nature of the FBG sensor [11]. An FBG sensor is used in -45° plies in order to detect a transverse crack in a 90° ply of a quasi-isotropic laminate $[45/0/-45/90]$, as shown in Figure 1.8. Non-uniform strain distribution causes a broadband spectrum of light after reflection from the FBG sensor due to initiation of the transverse crack (Figure 1.9) [11]. When there is no transverse crack in the composite, the spectrum will not be distracted, and the wavelength will be shifted, corresponding to the applied strain. If there are cracks present in the composite, then the shape of the reflected spectrum will be distorted [11]. Figure 1.10 shows the FBG sensor embedded in a $[45/-45/0/90]$ CFRP laminate specimen. The small-diameter optical fiber can be embedded in the laminate and penetrate the surface to the outside without causing any defect [11].

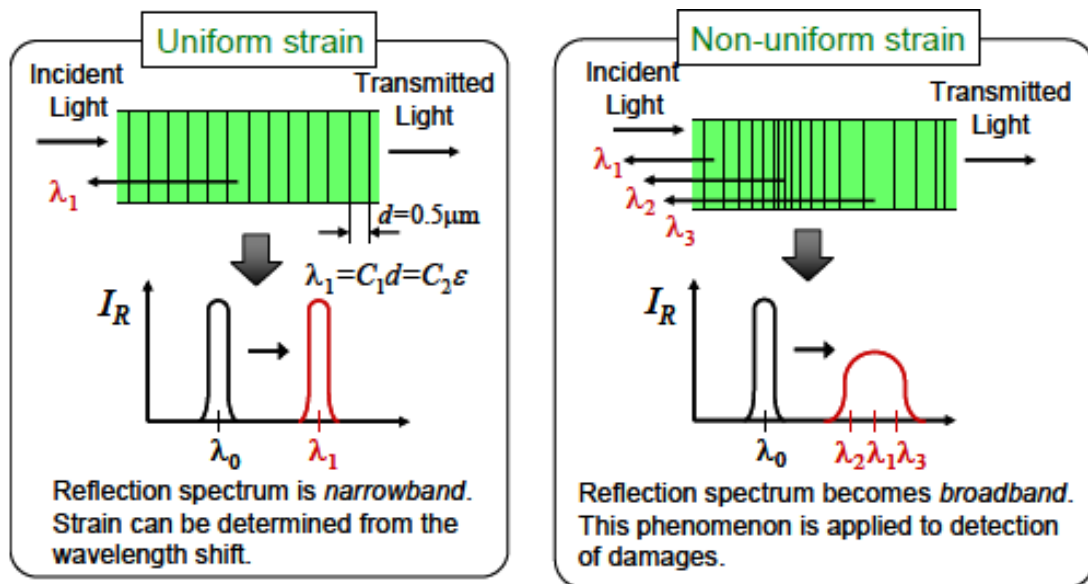


Figure 1.7. FBG sensor response to uniform and non-uniform strain distributions [11].

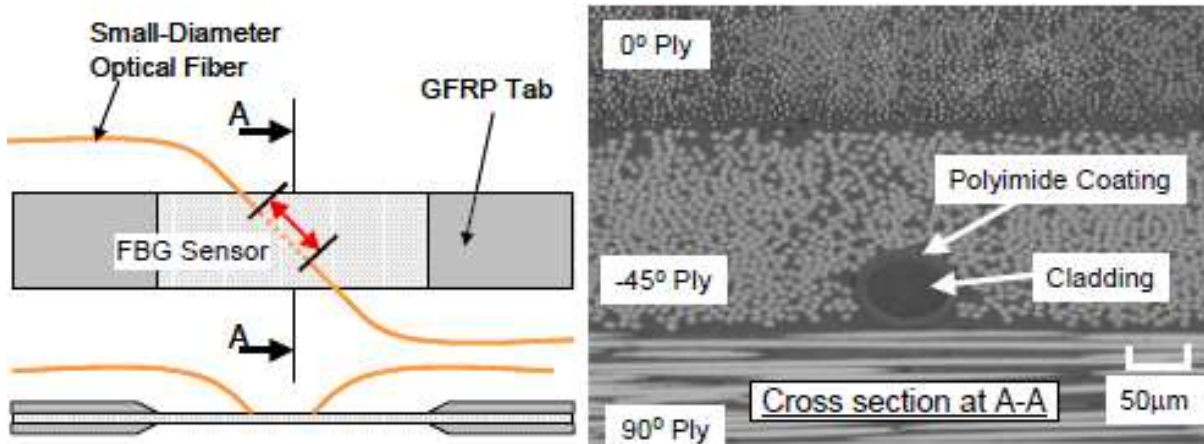


Figure 1.8. Small-diameter FBG sensor embedded in -45° ply transverse crack detection in close vicinity of 90° ply of quasi-isotropic $[45/0/-45/90]_s$ laminate [11]

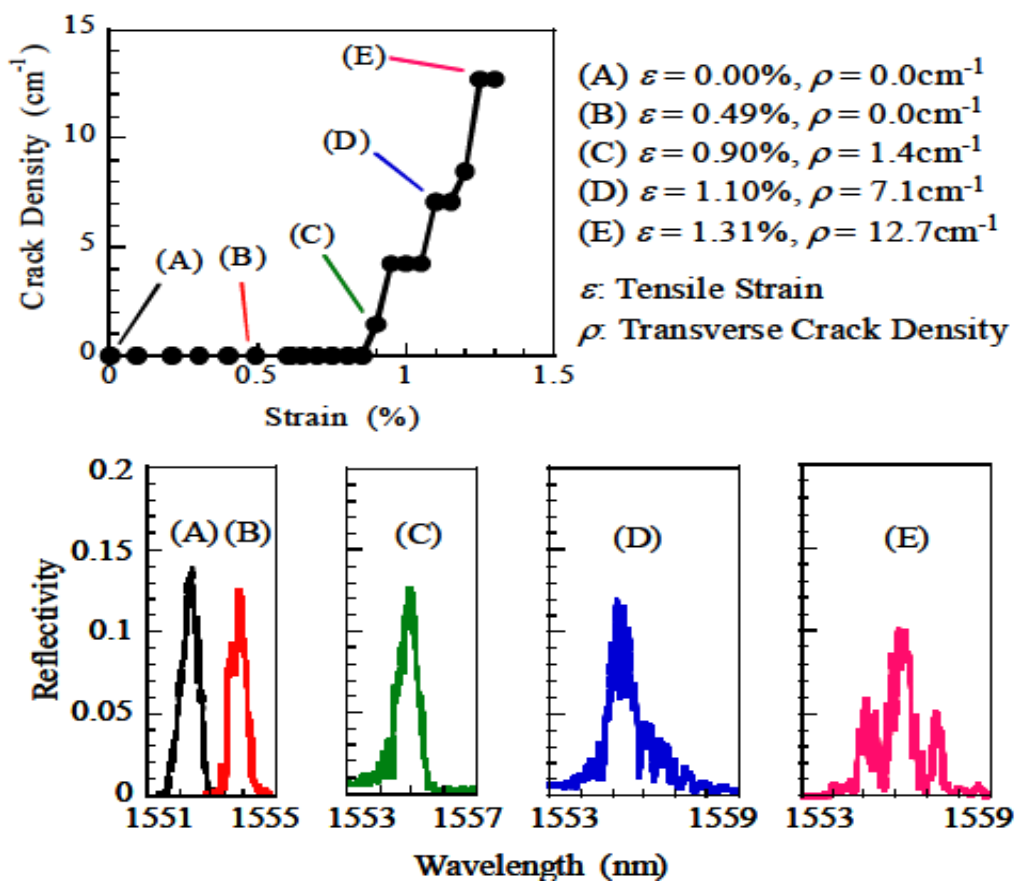


Figure 1.9. Change in wavelength distribution in reflected light from FBG sensor due to crack.

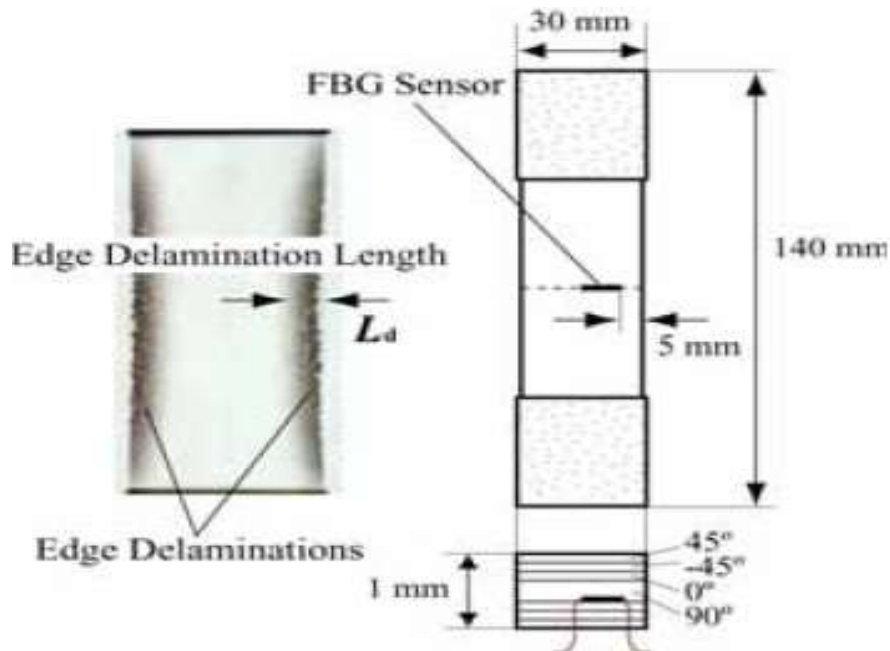


Figure 1.10. FBG sensor for determining edge delamination in [45/-45/0/90] composite [11].

The free-edge delamination grows at 0/90 and 90/90 under fatigue loading [11]. The reflected spectrum shows a single peak, which is separated into two peaks, and the peak at the longer wavelength grows as the edge delamination grows in the composite [11]. The two peaks from the reflected spectrum correspond to strain levels of the bonded and delaminated areas, respectively [11]. This method could be applied to many other kinds of delamination such as screw holes, rivet holes, and transverse cracks [11]. The FBG sensor can also be used to monitor axial thermal residual stress during fabrication of CFRP laminates [11]. The only problem with this kind of measurement is that the reflection spectra are distorted after fabrication due to non-axisymmetric thermal residual stresses caused by embedment of the sensor [11]. This kind of distortion in reflection spectra leads to unreliable measurements [11]. In order to avoid this problem, residual thermal stresses are measured from the reflection spectrum during the fabrication process and are correlated with theoretical predictions [11].

1.4 Piezoelectric Wafer Active Sensors

1.4.1 Piezoelectric Systems

A piezoelectric wafer active sensor is a less-expensive, small, nonintrusive, and unobtrusive device that can be mounted on a structure and can operate on the piezoelectric principle by integrating an electrical energy field and a mechanical energy field [19, 20]. This non-resonant device has wideband capabilities, and can be wired into sensor arrays and connected to data concentrators and wireless communicators [20]. The general constitutive equation of piezoelectric materials (ANSI/IEEE Standard 176-1987) relates to the electrical variables. The mechanical variables (mechanical stress S_{ij} , mechanical strain T_{kl} , electrical field E_k , and electrical displacement D_j) are of the following form [20, 22]:

$$S_{ij} = S_{ijkl}^E T_{kl} + d_{kij} E_k \quad (1.3)$$

$$D_j = d_{jkl} T_{kl} + \varepsilon_{jk}^T E_k \quad (1.4)$$

where S_{ijkl}^E is the mechanical compliance of the material at zero electric field ($E = 0$), ε_{jk}^T is the dielectric constant (dielectric permittivity) at zero mechanical stress ($T = 0$), and d_{jkl} is the piezoelectric coupling between mechanical and electrical variables [20, 22]. The piezoelectric effect converts the applied stress to the sensor to an electric charge [22], whereas the converse piezoelectric effect produces strain when voltage is applied to the sensor [22].

The electric field (E_3) is applied across the thickness in all three directions, and piezoelectric coupling occurs between the in-plane strain in two directions and the out-of-plane electric field in the third direction [22]. A PWAS tends to sense and excite the guided Lamb wave traveling long distances along the thin-walled structure of the aircraft at ultrasonic

frequency [22]. Lamb wave methods are considered a reliable method to locate damages in composite materials [21]. They have been mentioned in the literature in a variety of ways such as the use of separate actuators and sensors to monitor reflected and transmitted waves, and patches that can both sense and actuate [21]. Each of these methods has some advantages in detecting certain types of damage [21]. Lamb waves are elastic perturbation waves that propagate in a specimen with free boundaries [21]. Both symmetric and antisymmetric Lamb waves are shown in Figure 1.11. PWASs are made of thin piezoceramic wafers poled electrically in the direction of thickness and contain top and bottom electrodes [22]. They are generally 7 mm² or discs having a 0.2 mm thickness (Figure 1.12). PWASs are either experimentally embedded between the layers of a composite or can be bonded to the structure, similar to strain gauges [22].

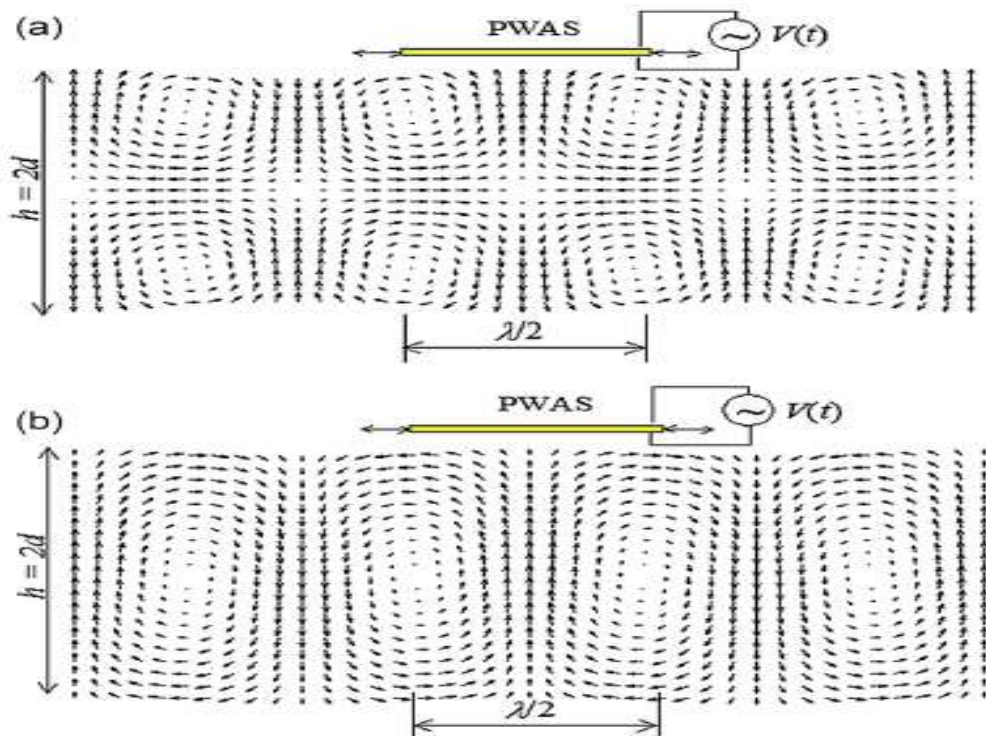


Figure 1.11. Coupling between Lamb wave and piezoelectric wafer active sensor in thin-walled structure: (a) symmetric mode; (b) antisymmetric mode [22].

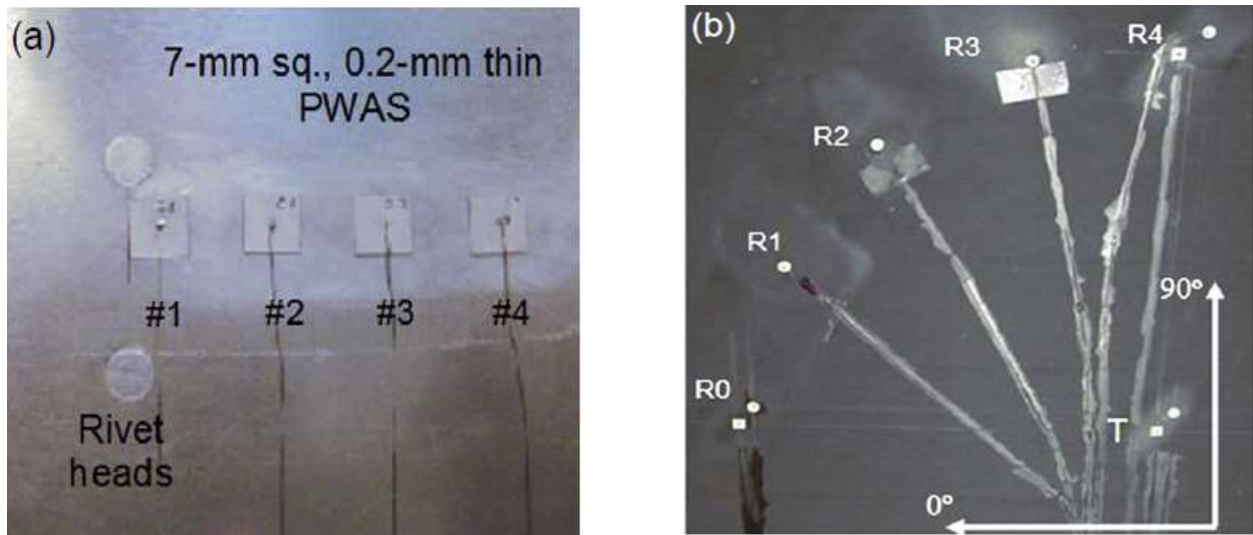


Figure 1.12. Piezoelectric wafer active sensors: (a) 7 mm² PWASs on metallic structure; (b) 7 mm round and square PWASs on composite [22].

Lamb waves in a thin-walled structure can detect microcracks, delamination, and corrosion damage [22]. PWAS transducers can act as transmitters as well as receivers of Lamb waves traveling in thin-walled structures [22]. As shown in Figure 1.13, PWAS transducers can serve many purposes, such as high-bandwidth wave exciters and receivers, high-bandwidth strain sensors, and embedded model sensors using the electromechanical (E/M) impedance method and resonators [22]. Depending upon the application, PWAS transducers can be employed for active sensing of far-field damage using pulse-echo, pitch-catch, and phased-array methods; active sensing of near-field damage using the high-frequency E/M impedance method and thickness gauge mode; and passive sensing of damage-generating events through detection of low-velocity impacts and acoustic emissions (AEs) at the tip of advancing cracks [22]. The PWAS produces Lamb waves in a thin-walled structure when excited with an electric field [22]. The traveling Lamb waves in a thin-walled structure are diffracted or reflected by the damage sites, and upon

arrival at the PWAS, they are transformed into electrical signals [22]. The PWAS can operate either in traveling or standing wave mode [22].

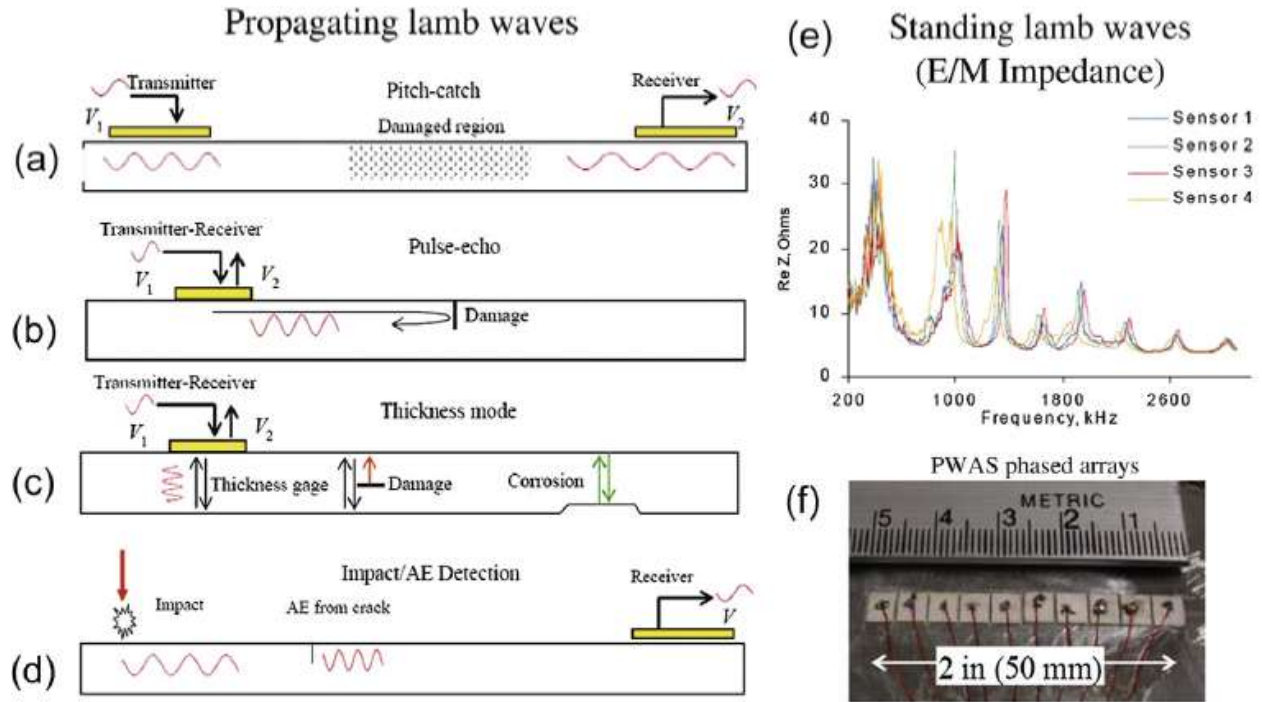


Figure 1.13. PWAS for detection of damage with standing and propagating guided waves in thin-walled structures: (a) pitch-catch, (b) pulse-echo, (c) thickness mode, (d) impact and acoustic emission (AE) detection, (e) electromechanical (E/M) impedance, (f) PWAS phased array [23].

1.4.2 Traveling-Wave PWAS Methods

Figure 1.13(a) shows the pitch-catch method of detecting damage in a structure [22]. Here, an electrical signal is applied at the transmitter. Through the piezoelectric transducer, the PWAS generates some signals into the structure and is captured at the receiver of the PWAS [1]. If there is no damage region in the structure, then the transmitted and received signal will be the same. However, if there is damage, then the received signal will be modified [22]. This method is applied to detect degradation in composites [22]. Figure 1.13(b) shows the pulse-echo method. Here, the PWAS acts as both transmitter and receiver. A tone-burst signal is applied to the

PWAS to generate elastic waves, which travel through the structure and are reflected from the boundaries and damage sites [22]. In a pristine structure, reflections from the boundaries appear, whereas in a damaged structure, reflections from boundaries as well as from damaged sites appear. By comparing the two signals, the presence of damage can be identified [22].

Figure 1.13(c) shows the PWAS transducer in thickness mode [22]. Here, the elastic waves are generally excited at a higher frequency—a 0.2 mm PWAS is excited at 12 MHz [22]. In a composite structure, the thickness mode measurements can detect microcracks parallel to the surface of a structure, such as delaminations [22]. There are some limitations to this technique. For example, it can detect damage in the close vicinity of the PWAS [23]. Figure 1.13(d) shows the detection of impact and acoustic emission events [22]. In this method, the elastic waves are generated by the impact or by an AE event, and the PWAS acts as a receiver of the elastic waves [23]. When waveforms of the Lamb wave AE signal are due to internal damage in the composite structure and are tested in conjunction with dynamic surface strain, this could impact the force recorded during impact tests. By employing several PWAS transducers in a network around the composite structure, a listening system can be installed to monitor any impact damage or AE event occurrence [22]. Signals recorded by the PWAS network can be processed to determine the exact location and amplitude of the impact or AE event.

1.4.3 Standing-Wave PWAS Methods

When a composite structure is excited with harmonic excitation at a given frequency, the elastic waves travel through the structure and experience boundary reflections and finally settle down in a standing-wave pattern [22]. Structural vibration occurs at the resonance frequency, and the structural response measured over a frequency range including resonance frequency

develops a vibration spectrum [22]. When there is a damage site in a structure, the vibration spectrum changes [22]. Conventional vibration analysis techniques are not capable of detecting very small damage; therefore, the electromechanical impedance method is capable of measuring a structural spectrum up to hundreds of KHz and in the MHz range [22]. The electromechanical impedance technique can measure electrical impedance, $Z(u)$, of a PWAS transducer employing an impedance analyzer [22]. When the PWAS is attached to a composite structure, the real part of the impedance measured at the PWAS terminals shows the structural dynamic spectrum [22]. Therefore, a PWAS attached to a structure can be used as a structural identification sensor to measure the structural response at high frequencies, as shown in Figure 1.13(e) [22].

1.5 Electrically Sensitive Sensors

Electrical SHM depends on materials behaving like sensors [22]. Epoxy is an insulator, whereas carbon fibers are thermally and electrically conductive [22]. However, if the volume fraction of carbon fiber is high, then the CFRP becomes somewhat conductive [23]. When cracks and delamination take place in composite materials, the electrical conductivity changes due to hindrance in the flow of electrons [22]. Glass fiber-reinforced polymer (GFRP) composites are insulators having certain dielectric properties [22]. Damage caused by microcracks and delamination changes the dielectric properties of composites since the dielectric constant of air is smaller than that of GFRP [23]. Traces of water change the overall dielectric properties of GFRP composites. The dielectric permittivity of water is around 80, which is much higher than that of GFRP composites. This method is self-sensing since it relies on measuring electrical characteristics and does not need an additional transduction sensor [22]. The only devices necessary to be installed on the composite structure are electrodes [22]. The outer skin of an

aircraft used to minimize a lightning strike can also serve as a measuring electrode [22]. Electrical SHM methods do not necessarily use the simple measurement of electrical resistance, but some more sophisticated methods, such as dielectric measurement, electrochemical impedance, and potential electrical mapping, are also used [22].

1.6 Electrospun Nanofiber-Based Sensors

1.6.1 Electrospun Nanofibers

Carbon nanofibers possess high strength and stiffness, have excellent thermal and electrical properties, and are used in an assortment of industrial applications, such as reinforcements in composites. They are also used in protective textiles, filtration membranes, electronics, and wound dressings [23-25]. The primary precursor used for the bulk production of carbon nanofibers is polyacrylonitrile. The most promising technique for the synthesis of fabricating carbon nanofibers is electrospinning, with PAN being the main polymer precursor [23, 24].

Electrospinning is a process that can generate continuous polymer fibers having diameters in the submicron range; the process involves the application of an external electric field imposed on a spinneret containing the polymer solution. Electrospun fibers possess several attractive structural features, including good tensile strength, high surface area per unit volume, interconnected open pores, and high porosity. In a typical electrospinning process, the polymeric solution (mixture of polymer and solvent) at the end of a capillary tube is held by its surface tension. In electrospinning polyacrylonitrile fibers, PAN is generally dissolved in dimethylformamide (DMF). DMF is the best solvent for PAN, although dimethylacetamide is also used. Here, a charge is induced in the liquid by an electric field. Mutual charge repulsion

creates tangential forces that overcome the surface tension, resulting in the formation of a cone (Taylor cone), and a jet emanates from the cone [32]. The jet travels linearly (Figure 1.14) for some distance, then experiences perturbations, and finally is collected on a collector screen placed some distance from the capillary tube [26, 27, 28]. The phenomenon of perturbations during electrospinning is referred to as “bending instability,” a dominant thinning mechanism in electrospinning. Typically, the bending instability causes the jet length to elongate at a rate of $1,000,000\text{s}^{-1}$, more than 10,000 times in a very quick interval of time. Such an enormous drawing rate effectively stretches the PAN macromolecular chains in ultrafine fibers and aligns them along the fiber axes. In addition to fast evaporation of the solvent, i.e., more than 99% solvent in electrospinning jets could be removed during or shortly after bending instability, the macromolecular orientation in the electrospun PAN nanofibers is likely to be retained on a collector screen [28]. Figure 1.14 shows a schematic of the electrospinning process.

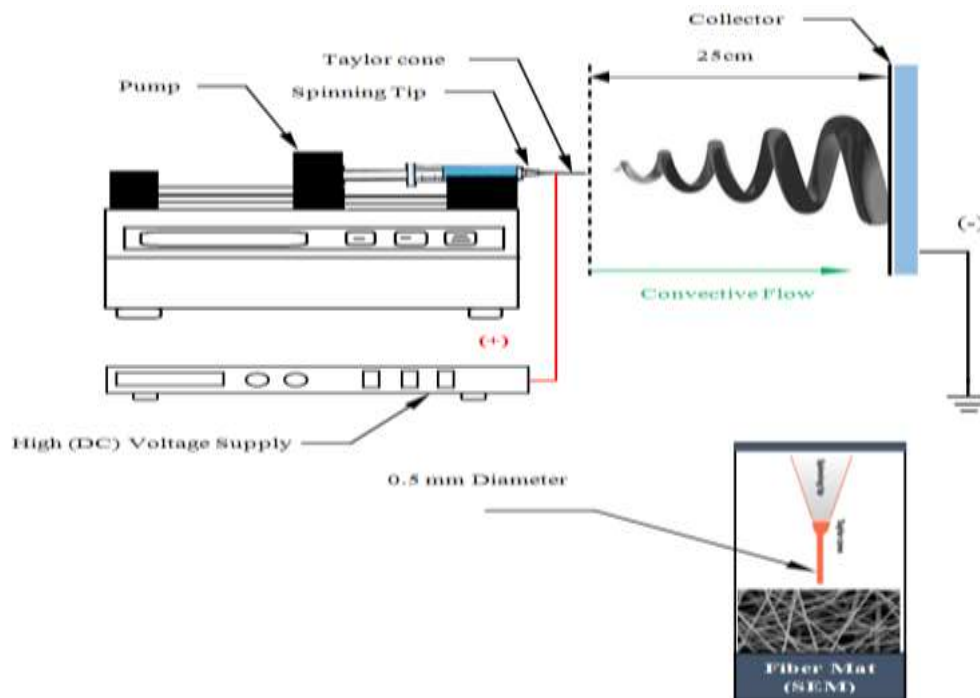


Figure 1.14. Schematic of electrospinning process.

The as-produced nanofibers are later converted to carbon nanofibers by stabilizing them in an oxygen atmosphere at 270°C for one hour followed by carbonization in an inert (argon) atmosphere at 850°C for one hour. After heat treatment, the non-carbon elements, such as hydrogen, oxygen, nitrogen, and sulfur, are eliminated and released as volatile matter, leaving material with a high carbon content. The pre-preg technique is used to fabricate nanocomposites. The conductive carbon film (PAN-derived carbon fibers) is placed at the top. These PAN-derived carbon fiber nanocomposites are used as a strain gauge in the composite structure of aircraft.

1.6.2 Electrical Conductivity for Uniaxial Tests

Composite panels prepared with carbonized PAN fibers on the top surface were cut to extract the composite specimens prior to electrical conductivity test using the MTS Criterion Model 44 High Elongation Extensometer [30]. The composite specimens had a length of 177.8 mm, width of 50.8 mm, and thickness of 1.26 mm. Electrical conductivity tests were conducted using the current and voltage supply units (Keithley Model 2230-30 electrometer and two Keithley Model 2110 electrometers, respectively) [30]. LabVIEW software and SRM-232 systems were employed to deliver unique and high-performance measurements with the PC software on the pre-preg carbon fiber composites [30]. A constant current was applied along the axial direction through outer probes while the corresponding voltage drop between inner probes was measured for various strains along the axial orientation of the composite samples [30]. Figure 1.15 shows a schematic of electrical conductivity tests on pre-preg composite samples incorporated with carbonized PAN nanofibers under different strain rates. [34] Motaghi, A et al. [34] studied electrical conductivity using PAN-derived long carbon fibers $6.25 \times 10^{+2}$ S/cm.

Brigandi, P et al. [35] claimed that using conductive polymer PAN with a multi-walled carbon nanotube (MWCNT) 0.625 yielded the highest electric conductivity of $1.2 \times 10^{+2}$ S/cm. Taipalus et al. [36] observed that the electrical conductivity of short carbon fiber is $1 \times 10^{+3}$ S/cm.

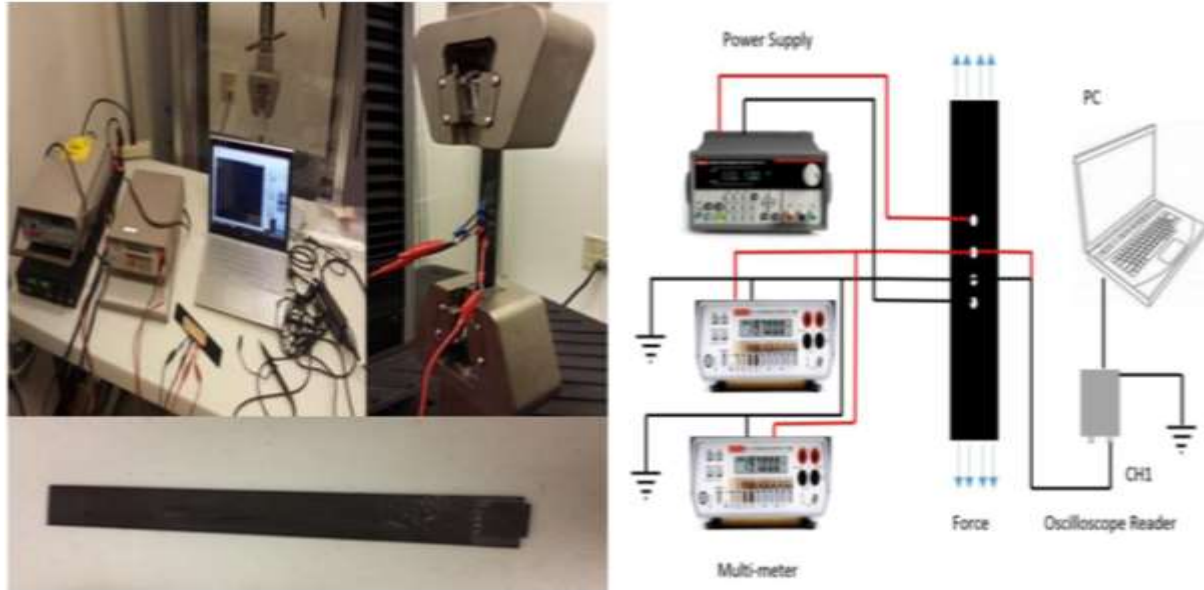


Figure 1.15. Schematic of electrical conductivity testing done on pre-preg composite samples incorporated with carbonized PAN nanofibers under different strain rates.

1.6.3 PAN-Derived Carbon Nanofibers as Strain Gauges

Voltage changes across the two inner probes is due to the change in dimension (direction of loading when the change in length occurs) of the carbon fiber specimen. This could be recognized by the change in resistivity of the specimen [32]. The change in voltage in the specimen increases with the applied load. As soon as the tensile stress increases, the change in voltage increases as well. A linear change in voltage was observed with respect to applied strain in the elastic region. A similar study was done by Eswaraiah et al. [31] on a functionalized graphene-reinforced nanocomposite as a strain sensor for structural health monitoring. For 0.02% strains, a voltage change of ~ 15.2 mV was observed in the specimen and was further

increased monotonically up to 0.085% of strain with a voltage change of 19.5 mV. This behavior leads to a nonlinear feature of voltage change when the specimen goes into the inelastic region [31]. PAN pre-carbonized fibers are advantageous for the enhancement of thermal and electrical properties of composites [38]. After the stabilization process, carbonization is carried out at a higher temperature (800–3000°C) in an inert atmosphere [39].

The oxidization of PAN is performed by increasing the temperature up to 270°C in an ambient condition, thus achieving cyclization/oxidation. The carbonization of PAN fibers can be performed by heating at different temperatures, such as 750°C, 850°C, and 950°C. The important aspect for a better mechanical strength of PAN-based carbon fibers is the systematic stability of the fibers in various conditions. Activation of the carbons was leached with 1% hydrochloric acid (HCl) for 2 hrs and then washed in distilled water (see Table 1.1) [40]. Using 0.1 mol L⁻¹ and deionized (DI) water, NaOH was used to activate the carbonized fibers in different concentrations [40]. The carbonized material (20 g) portion was mixed with 200 cm³ KOH solution in an impregnation ratio of 1:1 (KOH pallet: Char). Impregnation at 80°C with continuous stirring for 2 hours was employed [41].

During this dissertation study, the author collaborated with a number of undergraduate and graduate students in his area of expertise, and jointly they published 26 journal papers, conference proceedings, and book chapters. Some of those technical articles are provided in the reference list [42-67].

TABLE 1.1

ELECTRICAL CONDUCTIVITY K IN MS/CM FOR INDICATED CONCENTRATION IN MASS PERCENT

Name	Formula	0.5%	1%	2%	5%	10%	15%	20%	25%	30%	40%	50%
Acetic acid	CH ₃ COOH	0.3	0.6	0.8	1.2	1.5	1.7	1.7	1.6	1.4	1.1	0.8
Ammonia	NH ₃	0.5	0.7	1.0	1.1	1.0	0.7	0.5	0.4			
Ammonium chloride	NH ₄ Cl	10.5	20.4	40.3	95.3	180						
Ammonium sulfate	(NH ₄) ₂ SO ₄	7.4	14.2	25.7	57.4	105	147	185	215			
Barium chloride	BaCl ₂	4.7	9.1	17.4	40.4	76.7	109.0	137.0				
Calcium chloride	CaCl ₂	8.1	15.7	29.4	67.0	117	157	177	183	172	106	
Cesium chloride	CsCl	3.8	7.4	13.8	32.9	65.8	102	142				
Citric acid	H ₃ C(OH)(COO) ₃	1.2	2.1	3.0	4.7	6.2	7.0	7.2	7.1			
Copper(II) sulfate	CuSO ₄	2.9	5.4	9.3	19.0	32.2	42.3					
Formic acid	HCOOH	1.4	2.4	3.5	5.6	7.8	9.0	9.9	10.4	10.5	9.9	8.6
Hydrogen chloride	HCl	45.1	92.9	183								
Lithium chloride	LiCl	10.1	19.0	34.9	76.4	127	155	170	165	146		
Magnesium chloride	MgCl ₂	8.6	16.6	31.2	66.9	108	129	134	122	98		
Magnesium sulfate	MgSO ₄	4.1	7.6	13.3	27.4	42.7	54.2	51.1	44.1			
Manganese(II) sulfate	MnSO ₄		6.2	10.6	21.6	34.5	43.7	47.6				
Nitric acid	HNO ₃	28.4	56.1	108								
Oxalic acid	H ₂ C ₂ O ₄	14.0	21.8	35.3	65.6							
Phosphoric acid	H ₃ PO ₄	5.5	10.1	16.2	31.5	59.4	88.4	118	146	173	209	
Potassium bromide	KBr	5.2	10.2	19.5	47.7	95.6	144	194				
Potassium carbonate	K ₂ CO ₃	7.0	13.6	25.4	58.0	109	152	188	223			
Potassium chloride	KCl	8.2	15.7	29.5	71.9	143	208					
Potassium dihydrogen phosphate	KH ₂ PO ₄	3.0	5.9	11.0	25.0	44.6						
Potassium hydrogen carbonate	KHCO ₃	4.6	8.9	17.0	38.8	72.4	101	128				
Potassium hydrogen phosphate	K ₂ HPO ₄	5.2	9.9	18.3	40.3							
Potassium hydroxide	KOH	20.0	38.5	75.0	178							
Potassium iodide	KI	3.8	7.5	14.2	35.2	71.8	110	188	224			
Potassium nitrate	KNO ₃	5.5	10.7	20.1	47.0	87.3	124	157	182			
Potassium permanganate	KMnO ₄	3.5	6.9	13.0	30.5							
Potassium sulfate	K ₂ SO ₄	5.8	11.2	21.0	48.0	88.6						
Silver(I) nitrate	AgNO ₃	3.1	6.1	12.0	26.7	49.8	72.0	92.8	112	129	162	
Sodium acetate	NaCH ₃ COO	3.9	7.6	14.4	30.9	53.4	64.1	69.3	69.2	64.3		
Sodium bromide	NaBr	5.0	9.7	18.4	44.0	84.6	122	157	191	216		
Sodium carbonate	Na ₂ CO ₃	7.0	13.1	23.3	47.0	74.4	88.6					
Sodium chloride	NaCl	8.2	16.0	30.2	70.1	126	171	204	222			
Sodium citrate	Na ₃ C ₆ H ₅ O ₇		7.4	12.8	26.2	42.1	52.0	57.1	57.3	53.5		
Sodium dihydrogen phosphate	NaH ₂ PO ₄	2.2	4.4	9.1	21.0	33.2	43.3	49.6	53.1	54.0	46.1	
Sodium hydrogen carbonate	NaHCO ₃	4.2	8.2	15.0	31.4							
Sodium hydrogen phosphate	Na ₂ HPO ₄	4.6	8.7	15.6	31.4							
Sodium hydroxide	NaOH	24.8	48.6	93.1	206							
Sodium nitrate	NaNO ₃	5.4	10.6	20.4	46.2	82.6	111	134	152	165	178	
Sodium phosphate	Na ₃ PO ₄	7.3	14.1	22.7	43.5							
Sodium sulfate	Na ₂ SO ₄	5.9	11.2	19.8	42.7	71.3	91.1	109				
Sodium thiosulfate	Na ₂ S ₂ O ₃	5.7	10.7	19.5	43.3	76.7	104	123	134	136	118	
Strontium chloride	SrCl ₂	5.9	11.4	22.0	49.1	91.5	127	153	168	178		
Sulfuric acid	H ₂ SO ₄	24.3	47.8	92	211							
Trichloroacetic acid	CCl ₃ COOH	10.3	19.6	37.2	84.7	148	193	221				
Zinc sulfate	ZnSO ₄	2.8	5.4	10.0	20.5	33.7	43.3					

1.7 References for Chapter 1

- [1] Farrar, C. R., and Worden, K., “An Introduction to Structural Health Monitoring,” *Philosophical Transactions of the Royal Society of London A: Mathematical, Physical and Engineering Sciences*, Vol. 365, 2007, pp. 303-315.
- [2] Giurgiutiu, V., “Tuned Lamb Wave Excitation and Detection with Piezoelectric Wafer Active Sensors for Structural Health Monitoring,” *Journal of Intelligent Material Systems and Structures*, Vol. 16, No. 4, 2005, pp. 291-305.
- [3] Kang, I., Schulz, M. J., Kim, J. H., Shanov, V., and Shi, D., “A Carbon Nanotube Strain Sensor for Structural Health Monitoring,” *Smart Materials and Structures*, Vol. 15, 2006, pp. 737-748.
- [4] Chang, F. K., Ed., “Structural Health Monitoring 2013: A Roadmap to Intelligent Structures,” *Proceedings of the Ninth International Workshop on Structural Health Monitoring, September 10–12, 2013*, DEStech Publications, Inc., Vols. 1 and 2, 2013.
- [5] Diamanti, K., and Soutis, C., “Structural Health Monitoring Techniques for Aircraft Composite Structures,” *Progress in Aerospace Sciences*, Vol. 46, No. 8, 2010, pp. 342-352.
- [6] Rezende, M. C., and Botelho, E. C., “O Uso de Compósitos Estruturais na Indústria Aeroespacial,” *Polímeros*, Vol. 10, No. 2, 2000, pp. e4-e10.
- [7] Kashtalyan, M., and Soutis, C., “Stiffness and Fracture Analysis of Laminated Composites with Off-Axis Ply Matrix Cracking,” *Composites Part A: Applied Science and Manufacturing*, Vol. 38, No. 4, 2007, pp. 1262-1269.
- [8] Masaki, H., Yasuo, H., Takayuki, K., and Masaaki, N., “Recent Advances in Carbon Fiber Reinforced Plastics,” *Third International Conference on Sustainable Construction Materials and Technologies*, 2013, Kyoto Research Park, Kyoto, Japan, 9 pages.
- [9] Paul, D., Kelly, L., Venkayya, V., and Hess, T., “Evolution of U.S. Military Aircraft Structures Technology,” *Journal of Aircraft*, Vol. 39, 2002, pp.18–29.
- [10] Hojo, M., Matsuda, S., Tanaka, M., Ochiai, S., and Murakami, A., “Mode I Delimitation Fatigue Properties of Interlayer-Toughened CF/Epoxy Laminates,” *Composites Science and Technology*, Vol. 66, No. 5, 2006, pp. 665-675.

- [11] Chong, A. Y. B., Salski, B., Theodorakeas, P., Hatzioannidis, I., Kappatos, V., Selcuk, C., and Gan, T. H., "Inspection of Carbon-Fiber-Reinforced Polymer Composites Using Radio Frequency Inductive Sensors and Ultrasonic Techniques," *6th International Symposium on NDT in Aerospace*, 2014, Madrid, Spain, 10 pages.
- [12] Irving, P. E., and Soutis, C., Eds., *Polymer Composites in the Aerospace Industry*, Woodhead Publishing, 2014.
- [13] Takeda, N., "Recent Developments of Structural Health Monitoring Technologies for Aircraft Composite Structures," *Proceedings of the 26th International Congress of the Aeronautical Sciences*, 2008, Anchorage, Alaska, 12 pages.
- [14] N. Takeda, "Aircraft Composite Structures in Japan," *26th Congress of International Council of the Aeronautical Sciences including the 8th AIAA Aviation Technology, Integration, and Operations (ATIO) Conference*, 2008, Anchorage, Alaska. 11 pages.
- [15] Kessler, S. S., Spearing, S. M., and Soutis, C., "Structural Health Monitoring in Composite Materials Using Lamb Wave Methods," Sixteenth Technical Conference of the American Society for Composites, 2001.
- [16] Guo, H., Xiao, G., Mrad, N., and Yao, J., "Fiber Optic Sensors for Structural Health Monitoring of Air Platforms," *Sensors*, Vol. 11, 2011, pp. 3687-3705.
- [17] Udd, E., "An Overview of Fiber-Optic Sensors," *Review of Scientific Instruments*, Vol. 66, No. 8, 1995, pp. 4015-4030.
- [18] Edwards, A. T., "Comparison of Strain Gage and Fiber Optic Sensors on a Sting Balance in a Supersonic Wind Tunnel," Dissertation, Virginia Polytechnic Institute and State University, Blacksburg, VA, 2000.
- [19] Kersey, A. D., Davis, M. A., Patrick, H. J., LeBlanc, M., Koo, K. P., Askins, C. G., and Friebele, E. J., "Fiber Grating Sensors," *Journal of Lightwave Technology*, Vol. 15, No. 8, 1997, pp. 1442-1463.
- [20] Satori, K., Fukuchi, K., Kurosawa, Y., Hongo, A., and Takeda, N., "Polyimide-Coated Small-Diameter Optical Fiber Sensors for Embedding in Composite Laminate Structures," *Proceedings of the SPIE*, Vol. 4328, 2001, pp. 285-294.
- [21] Mizutani, T., Okabe, Y., and Takeda, N., "Quantitative Evaluation of Transverse Cracks in Carbon Fiber Reinforced Plastic Quasi-Isotropic Laminates with Embedded Small-Diameter Fiber Bragg Grating Sensors," *Smart Materials and Structures*, Vol. 12, No. 6, 2003, pp. 898-903.

- [22] Kreuzer, M., "Strain Measurement with Fiber Bragg Grating Sensors," White Paper, HBM, Darmstadt, 2006, 9 pages.
- [23] Morey, W. W., Meltz, G., and Glenn, W. H., "Fiber Optic Bragg Grating Sensors," *Proceedings of the SPIE*, Fiber Optic and Laser Sensors VII, 98 (February 13, 1990), pp. 98-107.
- [24] Beese, A. M., Papkov, D., Li, S., Dzenis, Y., and Espinosa, H. D., "In Situ Transmission Electron Microscope Tensile Testing Reveals Structure–Property Relationships in Carbon Nanofibers." *Carbon*, Vol. 60, 2013, pp. 246-253.
- [25] Nataraj, S. K., Yang, K. S., and Aminabhavi, T. M., "Polyacrylonitrile-Based Nanofibers—A State-of-the-Art Review." *Progress in Polymer Science*, Vol. 37, No. 3, 2012, pp. 487-513.
- [26] Chand, S., "Review Carbon Fibers for Composites," *Journal of Materials Science*, Vol. 35, No. 6, 2000, pp. 1303-1313.
- [27] Taylor, G., "Electrically Driven Jets," *Proceedings of the Royal Society of London A: Mathematical and Physical Sciences*, Vol. 313, 1969, pp. 453-475.
- [28] Waseem, S., Khan, Asmatulu, R., Ahmed, I., and Ravigururajan, T. S., "Thermal Conductivities of Electrospun PAN and PVP Nanocomposite Fibers Incorporated with MWCNTs and NiZn Ferrite Nanoparticles," *International Journal of Thermal Sciences*, Vol. 71, 2013, pp. 74-79.
- [29] Kalayci, V. E., Patra, P. K., Buer, A., Ugbolue, S. C., Kim, Y. K., and Warner, S. B., "Fundamental Investigations on Electrospun Fibers," *Journal of Advanced Materials*. Vol. 36, no. 4, October 2004, pp. 43-47.
- [30] Alarifi, I. M., Alharbi, A., Khan, W. S., and Asmatulu, R., "Electrospun Nanofibers for Improved Electrical Conductivity of Fiber Reinforced Composites," *SPIE Smart Structures/Non-Destructive Evaluation Conference*, San Diego, CA, March 8-12, 2015, 8 pages.
- [31] Eswaraiah, V., Balasubramaniam, K., and Ramaprabhu, S., "Functionalized Graphene Reinforced Thermoplastic Nanocomposites as Strain Sensors in Structural Health Monitoring," *Journal of Material Chemistry*, Vol. 21, No. 34, 2011, pp. 12626-12628.
- [32] Dharap, P., Li, Z., Nagarajaiah, S., and Barrera, E. V., "Nanotube Film Based on a Single-Wall Carbon Nanotube for Strain Sensing," *Nanotechnology*, Vol. 15, 2004, pp. 379-382.

- [33] Nuraje, N., Khan, W.S., Ceylan, M., Lie, Y., and Asmatulu, R., "Superhydrophobic Electrospun Nanofibers," *Journal of Materials Chemistry A*, Vol. 1, 2013, pp. 1929-1946.
- [34] Motaghi, A., Hrymak, A., and Motlagh, G. H., "Electrical Conductivity and Percolation Threshold of Hybrid Carbon/Polymer Composites," *Journal of Applied Polymer Science*, Vol. 132, No. 13, 2015.
- [35] Brigandi, P. J., Cogen, J. M., and Pearson, R. A., "Electrically Conductive Multiphase Polymers Blend Carbon-Based Composites," *Polymer Engineering & Science*, Vol. 54, No. 1, 2014, pp. 1-16.
- [36] Taipalus, R., Harmia, T., Zhang, M. Q., and Friedrich, K., "The Electrical Conductivity of Carbon-Fiber-Reinforced Polypropylene/Polyaniline Complex-Blends: Experimental Characterization and Modeling," *Composites Science and Technology*, Vol. 61, No. 6, 2001, pp. 801-814.
- [37] Mun, S. Y., Lim, H. M., and Lee, D. J., "Preparation and Thermal Properties of Polyacrylonitrile-Based Carbon Fiber–Silicon Carbide Core–Shell Hybrid," *Thermochemical Acta*, Vol. 600, 2015, pp. 62-66.
- [38] Ko, T.-H., Day, T.-C., Perng, J.-A., and Lin, M.-Fong, "The Characterization of PAN-Based Carbon Fibers Developed by Two-Stage Continuous Carbonization," *Carbon*, Vol. 31, 1993, pp. 765-771.
- [39] Nsami, J. N., and Mbadcam, J. K., "The Adsorption Efficiency of Chemically Prepared Activated Carbon from Cola Nut Shells by ZnCl₂ on Methylene Blue," *Journal of Chemistry*, Vol. 2013, 2013, 7 pages.
- [40] Rodrigues, L. A., de Sousa Ribeiro, L. A., Thim, G. P., Ferreira, R. R., Alvarez-Mendez, M. O., and dos Reis Coutinho, A., "Activated Carbon Derived from Macadamia Nut Shells: An Effective Adsorbent for Phenol Removal," *Journal of Porous Materials*, Vol. 20, No. 4, 2013, pp. 619-627.
- [41] Abechi, S. E., Gimba, C. E., Uzairu, A., and Dallatu, Y. A., "Preparation and Characterization of Activated Carbon from Palm Kernel Shell by Chemical Activation," *Research Journal of Chemical Sciences*, Vol. 3, No. 7, 2013, pp. 54-61.
- [42] Alarifi, I. M., Alharbi, A., Khan, W. S., and Asmatulu, R., "Carbonized Electrospun Polyacrylonitrile Nanofibers as Highly Sensitive Sensors in Structural Health Monitoring of Composite Structures," *Journal of Applied Polymer Science*, Vol. 133, No. 13, 2016, 7 pages.

- [43] Alarifi, I. M., Alharbi, A., Khan, W. S., Swindle, A., and Asmatulu, R., "Thermal, Electrical and Surface Hydrophobic Properties of Electrospun Polyacrylonitrile Nanofibers for Structural Health Monitoring," *Materials*, Vol. 8, No. 10, 2015, pp. 7017-7031.
- [44] Alarifi, I. M., Alharbi, A., Samsur, R., Potagani, A. G., and Asmatulu, R., "Synthesis, Analysis and Simulation of Carbonized Electrospun Nanofibers Infused Carbon Prepreg Composites for Improved Mechanical and Thermal Properties," *Fibers and Polymers*, Vol. 17, Iss. 9, 2016, pp. 1449-1455.
- [45] Alarifi, I. M., Alharbi, A., Khan, W. S., Samsur, R., and Asmatulu, R., "Mechanical and Thermal Properties of Carbonized PAN Nanofibers Cohesively Attached to Surface of Carbon Fiber Reinforced Composites," *Macromolecular Symposia*, Vol. 365, Iss. 1, 2016, pp. 140-150.
- [46] Alarifi, I. M., Alharbi, A., Khan, W., and Asmatulu, R., "Structural Health Monitoring of Composite Aircraft," Chapter 5 in *Advances in Materials Science Research*, Vol. 21, Nova Science Publishers, Inc., 2015, pp. 111-132.
- [47] Alarifi, I. M., Alharbi, A., and Asmatulu, R., "Fabrication and Characterization of Carbonized Polyacrylonitrile Nanofibers for Composite Aircraft and Wind Turbine Manufacturing," 12th Graduate Research and Scholarly Projects (GRASP) Symposium, Wichita State University, Wichita, KS, April, 2016 (extended abstract published).
- [48] Alarifi, I. M., Alharbi, A., Alsaiani, O., and Asmatulu, R., "Training the Engineering Students on Nanofibers-Based SHM Systems," American Society for Engineering Education (ASEE), Zone III Conference, 2015.
- [49] Alarifi, I. M., Alharbi, A., Khan, W. S., and Asmatulu, R., "Electrospun Carbon Nanofibers for Improved Electrical Conductivity of Fiber Reinforced Composites," *Proceedings of the SPIE*, Electroactive Polymer Actuators and Devices, 943032, April 1, 2015.
- [50] Alarifi, I. M., Alharbi, A., Khan, W. S., and Asmatulu, R., "Thermal and Electrical Properties of Carbonized PAN Nanofibers for Improved Surface Conductivity of Carbon Fibers Composites," *CAMX/SAMPE Conference*, Dallas, TX, October 27-29, 2015, 13 pages.
- [51] Alarifi, I. M., Khan, W. S., Rahman, A. K. M. S. Rahman, Kostogorova-Beller, Y., and Asmatulu, R., "Synthesis, Analysis and Simulation of Carbonized Electrospun Nanofibers Infused Carbon Prepreg Composites for Improved Mechanical and Thermal Properties," *Fibers and Polymers*, Vol. 17, No. 9, 2016, pp. 1449-1455.

- [52] Mahat, K. B., Alarifi, I. M., Alharbi, A., and Asmatulu, R., "Effects of UV Light on Mechanical Properties of Carbon Fibers Reinforced PPS Thermoplastic Composites," *Macromolecular Symposia*, Vol. 365, Iss. 1, 2016, pp. 157-168.
- [53] Asmatulu, R., Alharbi, A., Alarifi, I. M., and Shinde, M. A., "Electrospun Nanofibers Incorporated with C₆₀ Nanoparticles for Solar Energy Conversions," *Macromolecular Symposia*, Vol. 365, Iss. 1, 2016, pp. 128-139.
- [54] Asmatulu, R., Yeoh, J., Alarifi, I. M., and Alharbi, A., "Effects of Edge Grinding and Sealing on Mechanical Properties of Machine Damaged Laminate Composites," *SPIE Smart Structures/Non-Destructive Evaluation Conference*, Las Vegas, NV, March 21-24, 2016, 10 pages.
- [55] Faisal, M. S. S., Njoku, U., and Asmatulu, R., "Nanocomposite Sealants for the Edge and Hole Treatment of Aircraft Carbon Fiber Composites," *CAMX/SAMPE Conference*, Dallas, TX, October 27-29, 2015, 13 pages.
- [56] Alharbi, A., Alarifi, I. M., Khan, W., and Asmatulu, R., "Semiconductor Nanomaterials for Water Splitting," Chapter 6 in *Advances in Materials Science Research*, Vol. 21, Nova Science Publishers, Inc., 2015, pp. 133-156.
- [57] Alharbi, A., Alarifi, I. M., Khan, W. S., and Asmatulu, R., "Highly Hydrophilic Electrospun Polyacrylonitrile/Polyvinylpyrrolidone Nanofibers Incorporated with Gentamicin as Filter Medium for Dam Water and Wastewater Treatment," *Journal of Membrane and Separation Technology*, Vol. 5, No. 2, 2016, pp. 38-56.
- [58] Shinde, M. A., Alarifi, I.M., Alharbi, A., and Asmatulu, R., "Electrospun TiO₂ Nanofibers Incorporated with Graphene Nanoflakes for Energy Conversion," *Proceedings of the SPIE, Smart Materials and Nondestructive Evaluation for Energy Systems 2015*, 94390Z, March 27, 2015.
- [59] Alharbi, A., Alarifi, I. M., Khan, W. S., and Asmatulu, R., "Synthesis and Analysis of Electrospun SrTiO₃ Nanofibers with NiO Nanoparticles Shells as Photocatalysts for Water Splitting," *Macromolecular Symposia*, Vol. 365, Iss. 1, 2016, pp. 246-257.
- [60] Alharbi, A., Alarifi, I. M., Khan, W. S., Swindle, A., and Asmatulu, R., "Synthesis and Characterization of Electrospun Polyacrylonitrile/Graphene Nanofibers Embedded with SrTiO₃/NiO Nanoparticles for Water Splitting," *Journal of Nanoscience and Nanotechnology*, Vol. 17, 2017, pp. 1-9.
- [61] Alharbi, A., Alarifi, I. M., Khan, W. S., and Asmatulu, R., "Electrospun Strontium Titanate Nanofibers Incorporated with Nickel Oxide Nanoparticles for Improved Photocatalytic Activities," *Proceedings of the SPIE, Smart Materials and Nondestructive Evaluation for Energy Systems 2015*, 9439F, March 27, 2015.

- [62] Alharbi, A., Alarifi, I. M., Khan, W. S., and Asmatulu, R., "Co-Axial Electrospinning of Strontium Titanate Nanofibers Associated with Nickel Oxide Nanoparticles for Water Splitting," *CAMX/SAMPE Conference*, Dallas, TX. October 27-29, 2015, 13 pages.
- [63] Alharbi, A., Alarifi, I. M., and Asmatulu, R., "Comparative Studies between Different Nanofiber Photocatalysts for Water Splitting," *SPIE Smart Structures/Non-Destructive Evaluation Conference*, Las Vegas, NV, March 21-24, 2016, 10 pages.
- [64] Alharbi, A., Alarifi, I.M., and Asmatulu, R., "Highly Hydrophilic Electrospun Polyacrylonitrile/Polyvinylpyrrolidone Nanofibers Incorporated with Gentamicin as Filter Mediums for Drinking and Wastewater Treatments," 12th Graduate Research and Scholarly Projects (GRASP) Symposium, Wichita State University, Wichita, KS, April, 2016 (extended abstract published).
- [65] Seewoogolam, V., Alarifi, I.M., Mohammed, A., and Asmatulu, R., "Highly Robust Electrospun Nanofibers Films for the Fabrication of MAV Wings," *CAMX Conference*, Anaheim, CA, October 26-29, 2016.
- [66] Swarna, V. S., Alarifi, I. M., Mohammed, A., Patlolla, V. R., and Asmatulu, R., "Improving the Strengths of Metal-Metal Bonding Via Inclusion of Graphene Nanoflakes Into Adhesive Joints," *CAMX Conference*, Anaheim, CA, October 26-29, 2016.
- [67] Shagor, R. M. R., Alarifi, I. M., and Asmatulu, R., "Effects of Silanized Graphene Nanoflakes on Mechanical Properties of Carbon Fiber Reinforced Laminate Composites," *CAMX Conference*, Anaheim, CA, October 26-29, 2016.

CHAPTER 2

CARBONIZED ELECTROSPUN PAN NANOFIBERS AS HIGHLY SENSITIVE SENSORS IN STRUCTURAL HEALTH MONITORING OF COMPOSITE STRUCTURES

2.0 Abstract

Carbon fibers are novel high-performance materials. They can be described as fibers containing at least 90% carbon. Polyacrylonitrile is the main precursor for approximately 90% of carbon fibers manufactured today. Carbon fibers produced from the PAN copolymer precursor contain approximately 0.5–8 wt% co-monomers. The addition of co-monomers partially disrupts the nitrile-nitrile interactions in PAN macromolecules, rendering the copolymer more readily soluble in spinning solvents, thereby allowing better macromolecular chain orientation in the precursor fibers, and making the stabilized and carbonized fibers more structurally homogeneous.

Strain sensors have been studied extensively by researchers. They are widely used in industries such as in automobile, aerospace, medical, and household applications. Strain gauges work on the principle of piezoresistivity. They transform mechanical changes into electrical signals, meaning that the change in resistance, capacitance, or inductance is proportional to the strain experienced by the sensor. A good strain sensor has high sensitivity, exhibiting large resistance corresponding to small strains. Sensitivity largely depends on the properties of materials used in the fabrication of sensors. Carbonaceous materials have good piezoresistivity and therefore are widely used in sensor applications. In this study, PAN-derived electrospun nanofibers were carbonized to be transformed into pure carbonaceous materials, and they were used as sensors in SHM application for composite structures.

Electrospun PAN nanofibers were stabilized at 280°C for 1 hr in an ambient condition and then carbonized at 850°C in inert argon gas for an additional 1 hr in order to fabricate highly pure carboneous nanofibers for the development of highly sensitive sensors in the structural health monitoring of composite aircraft and wind turbines. Nanotechnology has brought unprecedented changes in the properties of these materials. The applications of composite materials have increased extensively in industries such as aerospace, defense, and automobile. The specific modulus and high specific strength characteristics of these materials make them attractive in aerospace, automotive, defense, and structural applications. The high strength, lightweight, continuous-fiber reinforced polymer matrix of composites has been key to it being a performance enabler for these platforms.

This study manifests the real-time strain response of the carbonized PAN nanofibers under various tensile loadings. The prepared carbon nanofibers were placed on top of a carbon fiber prepreg composite as a single layer using a hand lay-up method, and then co-cured with the prepreg composites in a vacuum oven following the curing cycle of the composite. Electric wires were connected to the top surface of the composite panels where the cohesively bonded conductive nanofibers were placed prior to the tensile and compression loadings in the tensile unit. Testing results clearly showed that the carbonized electrospun PAN nanofibers on the carbon fiber composites were performed remarkably well. Even the small strain rates (e.g., 0.020% strain) on the composite panels were easily detected through voltage and resistance changes of the panels. The change in voltage is mainly attributed to the breakage/deformation of the conductive network of the carbonized PAN nanofibers under the loadings. The main goal of

this study was to develop a cost-effective, lightweight, and flexible strain sensor for the SHM of composite aircraft and wind turbines.

2.1 Introduction

There has been an increasing perception of the significance of prognosis damage systems in mechanical, civil, energy, and aerospace structures [1]. The idea behind prognosis is to contemplate the prevailing health structures in real time and recommend an approximate estimation of the remaining utilitarian life of the structures. Structural health monitoring is a fundamental aspect of prognosis damage systems. A wide variety of non-destructive tools and materials are being used for SHM. The interest in SHM for consequential life-safety and economics has stimulated researchers to further investigate this issue. It is anticipated that a prognosis damage system embedded in a structure would assess the structure's health and inform the user about the emergent loss in real life [1].

As SHM technology transforms and becomes a fully-fledged method, it will be unsegregated into a comprehensive process known as damage prognosis, which is the estimation of the remaining useful life of an engineered system [2-3]. This estimation is based on the output of models that show behavioral progress by integrating information from monitoring current and past operating conditions and predicting future environmental and operating consequences. The process of designing a damage-identification strategy for all kinds of infrastructures, such as bridges, tunnels, aircraft, wind turbines, ships, skyscrapers, and towers, is generally referred to as SHM [2-4]. SHM allows engineers to use the sensing of structural responses against all types of loading during service in combination with proper data acquisition and model updating techniques to appraise the condition of a structure.

The purpose of SHM is to monitor the damage in infrastructures effectively and take preventive measures before a catastrophic failure occurs [1]. Owing to its usefulness and economic advantages, SHM has been a topic of recent interest for many years, and a large number of published articles quantify its importance. The prospective advantages of SHM are mammoth since the maintenance procedures for structures can change from schedule-based to condition-based, resulting in reducing the period of time that the structure is out of service, corresponding cost savings, and a reduction in labor requirements.

SHM technology can be classified into active and passive schemes. Passive technology includes acoustic emission and strain/load monitoring, which has already been reported by many researchers with a good degree of success [5-10]. Active schemes are capable of exciting the structures, thereby detecting damage at precise locations within a very short period of time. The factors that must be considered before selecting a technology for SHM applications are low cost, large area processability, seamless integration with the composite structure, and ease of signal detection and processing [12,13].

Considering the cost and large area integration with composite structures, PAN nanofibers are promising candidates for being strain sensors in composite structures. Recently, there has been significant interest in strain sensing using polymer nanocomposites due to their unique designs and properties [14]. Carbon nanofibers possess high strength and stiffness, and also display unique thermal and electrical properties for a wide range of applications in structural components, composite reinforcement, protective textiles, filtration membranes, electronics, wound dressings, and lithium ion batteries [15-19]. Carbon fibers are defined as fibers containing a minimum of 92% carbon by weight, while graphitic fibers are defined as those containing

around 99% carbon by weight [20]. The primary precursor used for the bulk production of carbon nanofibers is polyacrylonitrile, which contains 68% carbon [20].

The most promising technique for the synthesis of carbon nanofibers is electrospinning with PAN, polyvinyl alcohol (PVA), or polyvinyl chloride, which are the main polymeric precursors [15,16]. Electrospinning presents a potential breakthrough in fiber-forming technology by dramatically reducing the fiber diameters resulting in an outstanding improvement in fiber mechanical properties. The diameter of fibers via electrospinning is in the range of 10 nm to approximately 200 nm, which is nearly two to three orders less than that produced by the conventional spinning process. The reduction in fiber diameter results in an increased aspect ratio and effective surface area of the fibers.

In this study, PAN-derived carbon fibers were fabricated through the electrospinning process followed by stabilization and carbonization to remove the non-carboneous material and ensure mainly pure carbon formations. Electrospun fibers have diameters between 10 nm and 10 μm , which are ideal for SHM [21, 22]. The major advantage of carbon fibers is the high surface area (100 to 1,000 times higher than regular fibers) due to the nanoscale size, flexibility, and enormous sensing ability under small physical changes [23]. Precursor materials largely determine the properties of carbon fibers, and the process parameters are used to generate various size and shape of fibers. Heat-treatment significantly refines the as-spun structure. The orientation of fibers is basically established during electrospinning [24]. The major objective of this study was to fabricate carbonized PAN nanofibers via electrospinning process, heat-treat them to remove all non-carboneous material, and finally use them for SHM in composite aircraft and wind turbines.

2.2 Experimental Materials and Methods

2.2.1 Materials

Polyacrylonitrile having a molecular weight of 150,000 g/mole (CAS no. 25014-41-9, 0.2%) and dimethylformamide (CAS no. 68-12-2, 99.8%) were purchased from Sigma-Aldrich and used without any further purification. Pre-preg carbon fibers were purchased from Cytec Engineering Materials (Part No. 5320-1) and cured according to the manufacturer's instructions. The epoxy resin system of the pre-preg carbon fibers, according to the manufacturer, is specified in Table 2.1.

TABLE 2.1
CHARACTERISTICS OF EPOXY RESIN SYSTEM FOR PRE-PREG
CARBON FIBERS (5320-1)

Shelf Life	1 year at < 10°F (-12°C)
Track Life	20 days at room temperature
Shop Life	30 days minimum at room temperature
Cured Resin Density	1.31 g/cc
Wet Glass Transition Temperature	324°F (163°C)
Average Moisture Uptake	0.55 wt%

2.2.2 Fabrication and Carbonization of PAN Nanofibers

PAN powder was dissolved in DMF solvent at 90:10% weight ratios, and the mixture was subjected to shear mixing at 500 rpm for 1 hr on a hot plate. Particular care was taken to ensure a homogeneous blend/dissolution of the polymeric solution. This mixture was then transformed to a 10-ml syringe with an inside diameter of 10 mm. Nanofibers were fabricated using an electrospinning process carried out at 25 kV DC with a 1 ml/hr feed rate at a 25cm

distance between the capillary tube and collector screen. The as-produced PAN nanofibers were converted to carbon nanofibers by stabilizing them in an ambient environment at 280°C for 1 hr, and then subsequently carbonizing them at 850°C for 1 hr in an argon atmosphere.

During stabilization, a cyclization reaction takes place, in which the nitrile groups in the precursor fibers form a ladder-like structure with adjacent groups, thereby strengthening the stability of the polymeric structure. This ladder-like structure can sustain high temperature and improves the carbon yield of the PAN fibers [25]. The cyclization of nitrile groups in PAN is highly exothermic, accompanied by rapid heat build-up in the sample and leading to fragmentation of the polymeric chains. The heat does not dissipate rapidly. The intermolecular oligomerization of the nitrile groups leads to a cross-linking structure, which is possibly more important than the intramolecular reaction, resulting in a ladder-like structure because of the high PAN temperature. The nitrile group oligomerization becomes dominant at a temperature above 200°C, a temperature at which a radical mechanism most likely takes place. Since the carbon-carbon bonds are the weakest in the PAN polymer, a hemolytic main chain scission may be assumed as the consequential outcome of the heat treatment. The radicals formed as a result then initiate the carbon-nitrogen (C-N) oligomerization. During carbonization, the carbon chain substances are condensed into carboneous materials, thereby increasing carbon yields and releasing gasses such as nitrogen and hydrogen, as well as other compounds. In this process, almost all elements other than carbon are eliminated in the form of appropriate byproducts, and a graphite-like structure containing approximately 90% carbon is formed.

Scanning electron microscopy (SEM) was used to determine the surface morphology and diameters of the PAN nanofibers. Figure 2.1 shows SEM images of electrospun PAN nanofibers

before and after carbonization at 850°C. As shown in Figure 2.1(a), the average diameter of the PAN fibers was around 550 ± 50 nm before carbonization; however, after the carbonization, the diameter was reduced to 400 ± 50 nm, retaining their shape and morphology. Shrinkage occurs entropically and chemically. Entropic shrinkage is caused mainly by the retraction of stretched polymer chains, while chemical shrinkage is caused primarily by the formations of dense structures after the chemical reactions [25]. Entropic shrinkage constitutes physical changes and is independent of the heating rate; however, chemical shrinkage can be increased by increasing the heating rate [25].

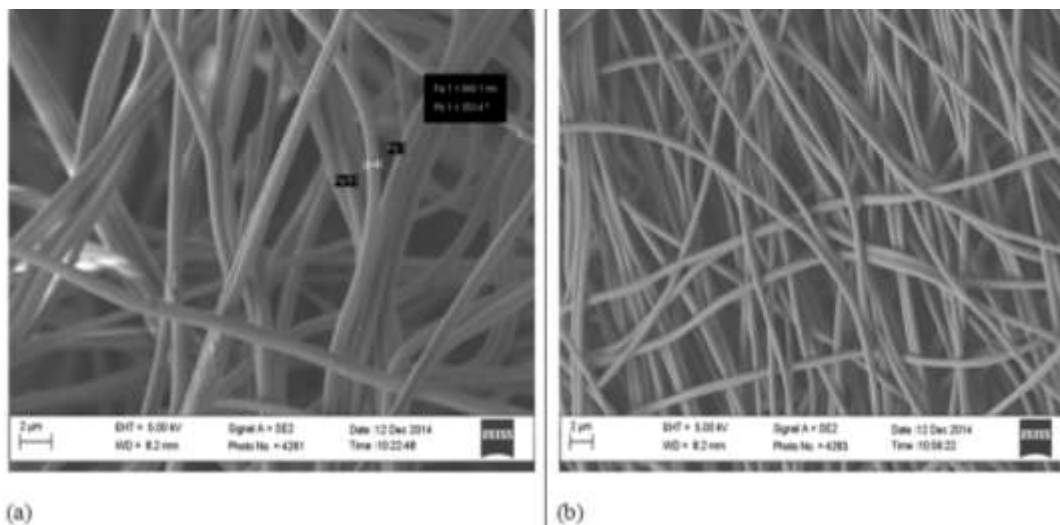


Figure 2.1. SEM images of electrospun PAN nanofibers: (a) before carbonization process; (b) after carbonization process.

Micro-combustion and pyrolysis of the PAN fibers revealed that the carbonized nanofibers contained around 89.47% carbon, 3.93% nitrogen, 3.08% oxygen, and 0.33% hydrogen (minute amount) [24]. The presence of nitrogen is due to the C-N bonds that are found in PAN when the heat treatment is carried out at a temperature below 2,000°C and molecular

entrapments occur during the reaction [24]. Table 2.2 lists the properties of the carbonized electrospun PAN nanofibers.

TABLE 2.2

PROPERTIES OF CARBONIZED ELECTROSPUN PAN NANOFIBERS.

Properties	Values
Thickness	1.26 mm
Resistivity	0.00075 m.Ω
Strain	0.085%
Yield Stress	350 MPa
Modulus of Elasticity	4546.9 MPa
Peak Load	2.3882.56 N

2.2.2 Fabrication of Conductive PAN Nanofibers on Composites

The prepreg technique was employed to fabricate carbon fiber composite panels (5320-1) incorporated with carbonized PAN nanofibers as top layers. The manufacturer’s recommended cure cycles for flexible capability are listed in Table 2.3, and the tensile properties of the manufacturer’s 5320-1 epoxy resin system are listed in Table 2.4.

TABLE 2.3

RECOMMENDED CURE CYCLES FOR PRE-PREG CARBON FIBERS (5320-1)

Parameter	Cure Cycle A	Cure Cycle B
Ramp Rate	1 – 3 °F/minute (0.6 – 1.7°C/minute)	1 – 5 °F/minute (0.6 – 2.8°C/minute)
Cure Temperature	200 ±10°F (93 ± 6°C)	250 ±10°F (121 ± 6°C)
Cure Time	12 hours	3 hours
Free-Standing Post Cure	2 hours at 350°F (177°C)	2 hours at 350°F (177°C)

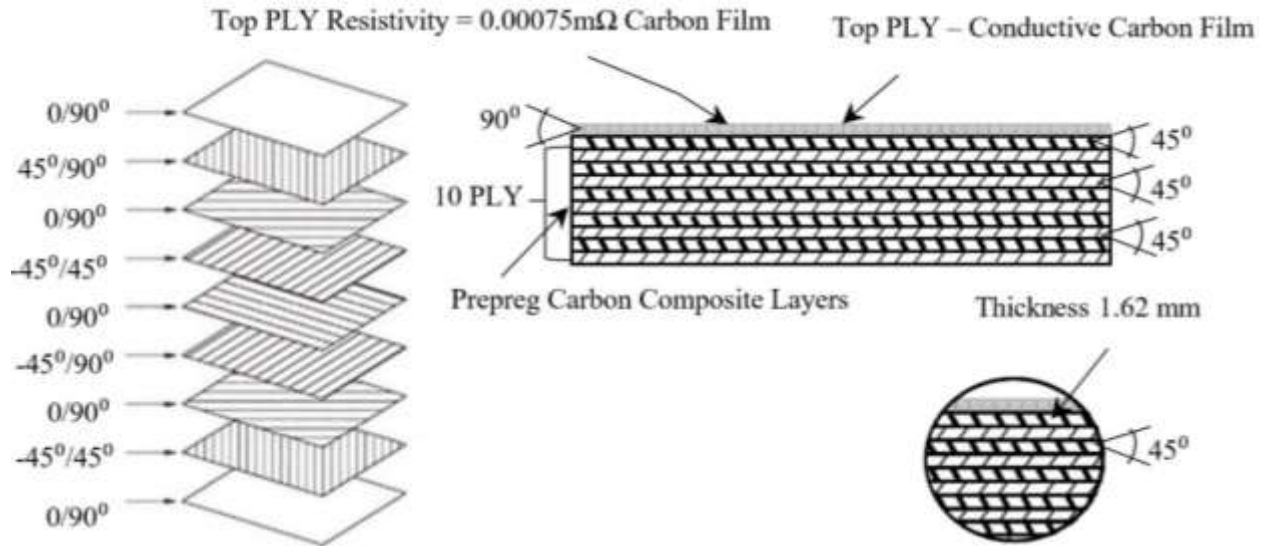
TABLE 2.4

TENSILE PROPERTIES OF 5320-1 EPOXY RESIN SYSTEM

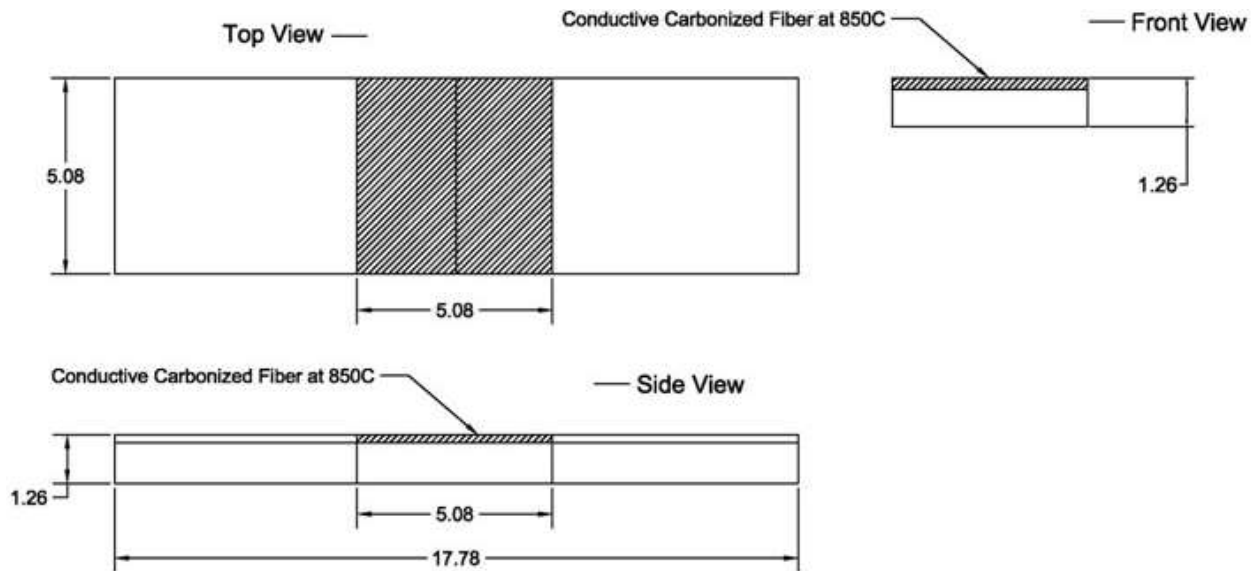
Properties (Cure Cycle A) ¹	Test Method Lay Up	Condition	Results ²
0° Tension Strength, ksi (MPa) Modulus Msi (GPa) Poisson's Ratio	ASTM D3039 [0]8	-100°F (-73°C) DRY	372 (2565) 22.6 (156) 0.258
		RTA	392 (2703) 22.7 (156) 0.344
90° Tension Strength, ksi (MPa) Modulus Msi (GPa)	ASTM D3039 [90]16	-100°F (-73°C) DRY	12.1 (83) 1.6 (11.0)
		RTA	11.7 (81) 1.4 (9.7)
		220°F (104°C) WET ³	7.9 (54) 1.2 (8.1)
90°/0° Tension Strength, ksi (MPa) Modulus Msi (GPa)	ASTM D3039 [90,0]4S	RTA	190 (1310) 11.9 (82.0)
Un-notched Tension Strength, ksi (MPa) Modulus Msi (GPa)	ASTM D3039 [45,90,-45,0]3S	-100°F (-73°C) DRY	124 (857) 8.5 (58.4)
		RTA	135 (931) 8.4 (57.6)
Open Hole Tension Strength, ksi (MPa) Modulus, Msi (GPa)	ASTM D5766 [45,90,-45,0]3S	-100°F (-73°C) DRY	67.5 (465) 8.9 (61.2)
		RTA	72.3 (498) 8.6 (59.0)
Filled Hole Tension Strength, ksi (MPa) Modulus, Msi (GPa)	ASTM D6742 [45,0,-45,0,0,45,90,- 45,0,0,45,0,-45,0]S	-100°F (-73°C) DRY	99.1 (683) 14.1 (97.2)

Ten plies of the prepreg carbon fibers were laid up in a 0-, 45-, -45-, and 90-degree stacking sequence on a flat and smooth aluminum mold, and then the carbonized PAN nanofiber mat was laid on the top portion of the pre-preg composites. Figure 2.2(a) shows the layup fabrication scheme of the composite incorporated with carbonized PAN nanofibers mats as top layers used for strain testing. Figure 2.2(b) shows the specimen used in strain-sensing tests used in this study. The curing cycle involved four major steps: (1) heating the composite at 50°C for 30 min, (2) heating the composite at 120°C for 60 min, (3) heating the composite at 180°C for

120 min, and (4) reducing the heat of the composite to 50°C for 30 min. Table 2.3 shows the curing cycle of the carbon fiber pre-preg with the carbonized PAN nanofiber mat for fabricating the conductive carbon fiber composite.



(a)



(b)

Figure 2.2. Schematic images of testing setups: (a) layup fabrication scheme of carbon fiber composite incorporated with carbonized PAN nanofibers; (b) specimen used in strain sensing.

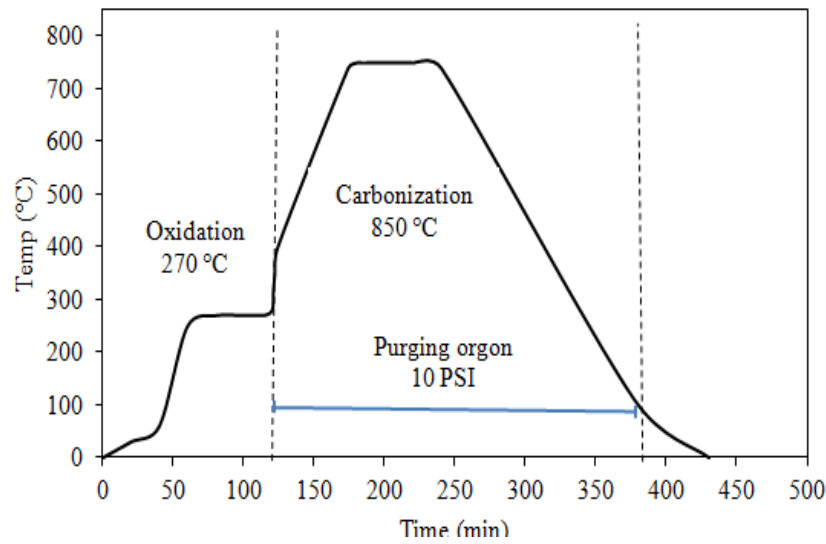


Figure 2.3. Curing cycle of carbon fiber pre-preg with carbonized PAN nanofibers mat.

2.2.3 Strain-Sensing Tests for SHM

Figure 2.4 shows views of the experimental test setup for determining the strain-sensing response of the prepared composite coupons.

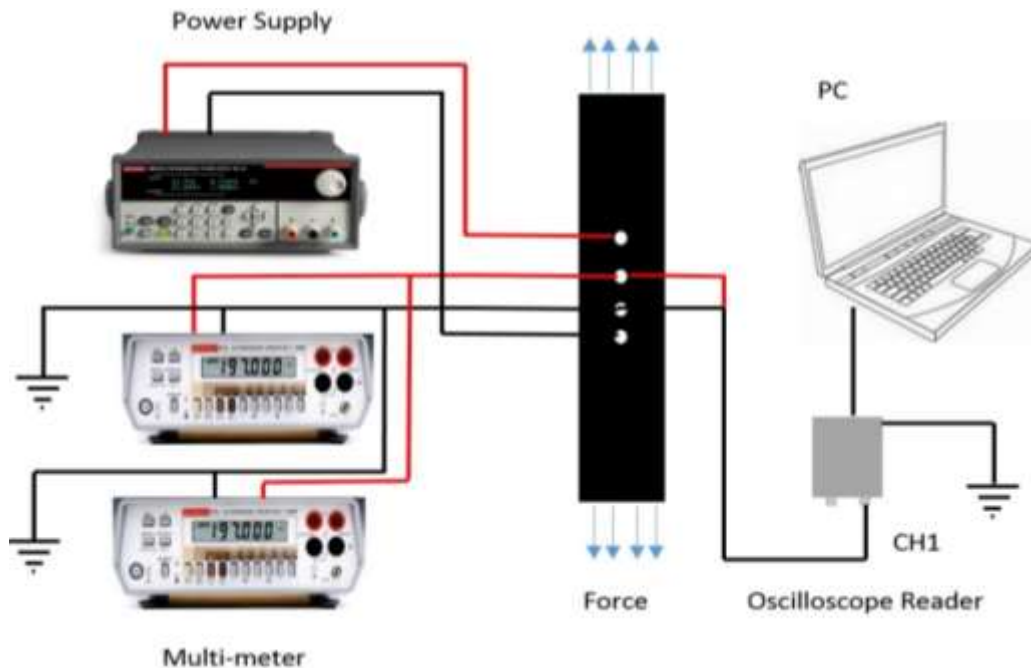


Figure 2.4. Experimental views of test setup for strain-sensing response studies on prepared composite coupons.

The composite specimen had a length of 177.8 mm, width of 50.8 mm, and thickness of 1.26 mm, the same as used for the tensile tests. A four-circumferential ring probe was employed to measure resistance in the nanocomposite sample. The composite specimen was sanded at locations where the probes were to be attached. Then the probes were attached to the PAN fiber mat, and a silver conductive epoxy adhesive was applied in order to avoid contact resistance. A constant current was applied along the axial direction via outer probes, and the corresponding voltage drop between inner probes was measured for various strains along the axial direction.

Data was continuously acquired using a LabVIEW software program. The sample was subjected to both tensile and compression ramping loads. The specimen was loaded at a constant rate of 1 mm/min. The displacement as the result of loading was used to calculate the strains under quasi-static loading rates. The specimen was subjected to tension as well as compression cycles in a servo-hydraulic test frame. A good contact between specimen and probes was ensured in order to stabilize voltage across the inner probes. The load was applied in increments and held constant for several seconds so that stable readings could be obtained for each test. The input current across the two outer probes was kept constant during the time of measuring the voltage reading across the two inner probes and strains from the strain gauge. For each test, at least three readings were performed, and the test results were averaged for the data point.

2.3 Results and Discussion

Figure 2.5 shows the engineering stress-strain curve of the carbon fiber composites co-bonded with the carbonized electrospun PAN nanofibers. It can be seen that with a 0 strain rate, the composite panel linearly deforms until fracture failure occurs [15]. The carbon fiber composites usually provide linear behavior because of their brittle structures, so adding

carbonized PAN nanofibers can change the overall behavior of the samples [15]. Arshad et al. previously reported that the modulus of elasticity considerably increased with a decrease in the fiber diameter [26]. The dependence of fiber strength on diameter has also been studied in various fibers, and it has been found that decreasing the fiber diameter resulted in lower fiber volume and a reduced number of defects and cracks, thus causing a significant decline in the probability of failure [27, 28]. As shown in Figure 2.5, the percentage elongation at failure is 0.085, which corresponds to a stress value of 350 MPa.

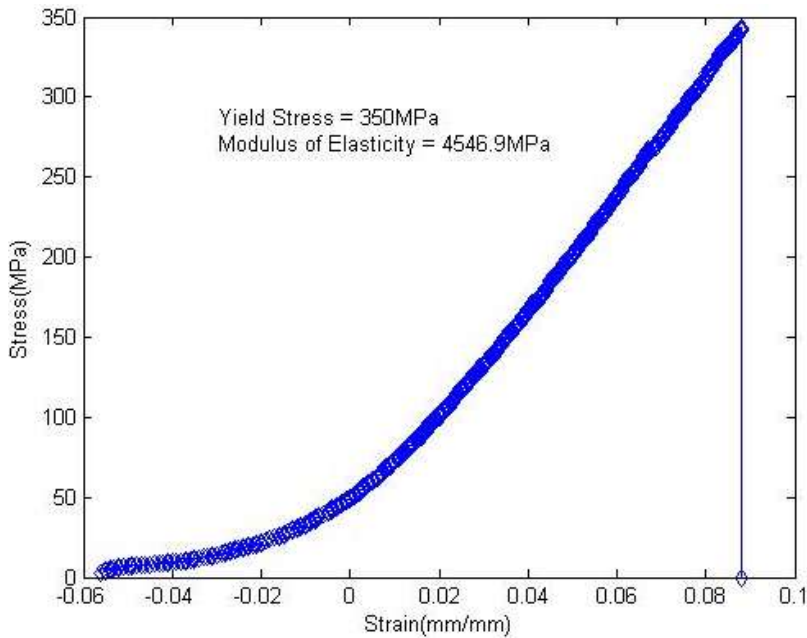


Figure 2.5. Engineering stress-strain curve for carbon fiber composites co-bonded with carbonized electrospun PAN nanofibers.

Figure 2.6 shows the monotonic increment of stress vs. time on the composite specimen co-bonded with the carbonized electrospun PAN nanofibers, while Figure 2.7 shows strain vs. time on the same samples. When the external load was applied to the composite specimen, the carbonized PAN nanofibers on the specimen experienced some deformation based on both stress and strain rates.

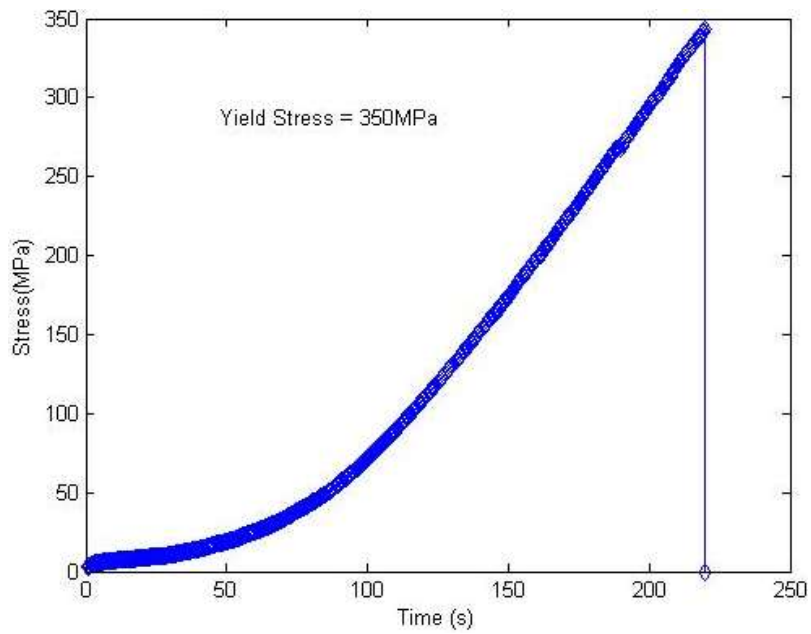


Figure 2.6. Monotonic increment of stress vs. time of composite specimen co-bonded with carbonized electrospun PAN nanofibers.

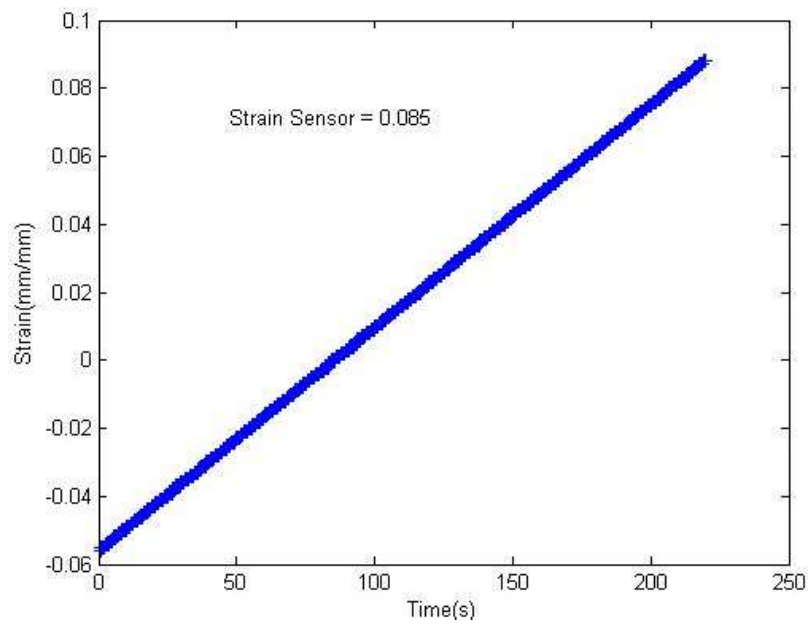


Figure 2.7. Strain vs. time curve of composite specimen co-bonded with carbonized electrospun PAN nanofibers.

When the nanofibers were electrospun at higher distances between the capillary tube and the collector screen, they displayed higher modulus and higher tensile strength since they possess better molecular orientation and fewer defects. Recent studies have reported that PAN nanofibers fabricated at 25 kV and a distance of 25 cm between the target and the collector have the highest tensile strength and modulus; however, the strain failure under those electrospinning conditions could be around 200% [29]. The high modulus of the carbonized PAN nanofibers on the carbon composites might be due to the stabilization at high temperature, which results in a high capacity fraction of a purely ordered phase, possibly caused by additional cross-linking reactions and fewer defects [25].

Figure 2.8 shows the change in voltage during the loading of the composite specimen co-bonded with carbonized electrospun PAN nanofibers. Figure 2.7 previously showed a linear relation between the changes in strain during loading. The change in voltage across the two inner probes might be due to the change in dimensions (change in length along the direction of loadings) of the carbon fiber specimen and can be recognized by the change in resistivity of the specimen [36]. The other reason for the change in voltage might be the loss of contact with the fibrous nanomaterial (carbonized electrospun PAN nanofibers). This may also be related to the external tensile loading and the change in the electrical properties of the carbonized PAN nanofibers under tensile testing that greatly changes the voltage. The change in voltage was observed when the specimen experienced a continuous increment in the loading. As soon as the tensile stress/strains increased, the change in voltage also increased linearly in the elastic region. Strain sensing using carbonaceous material (carbon nanotubes) was studied by Dharap et al. [36], who found a linear change in voltage across a film subjected to tension and compression.

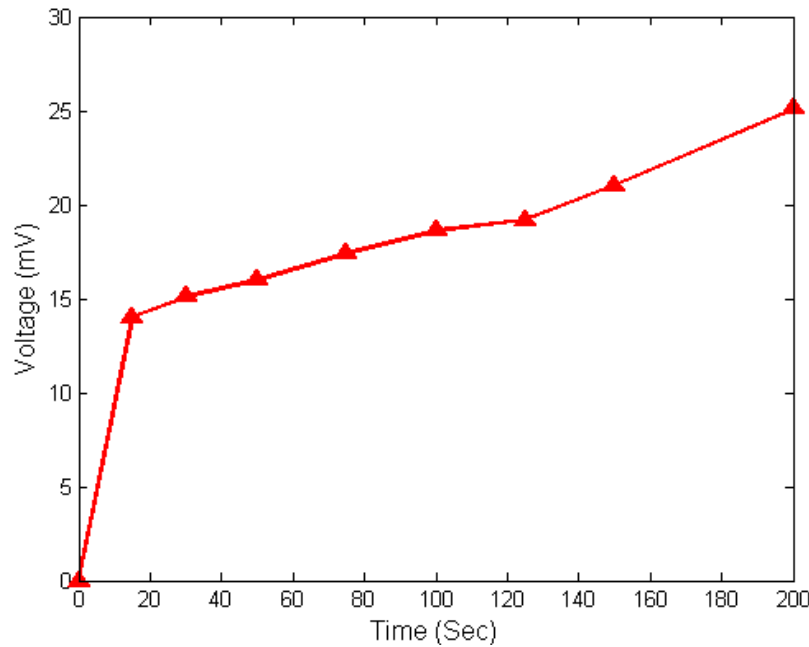


Figure 2.8. Change in voltage during loading of composite specimen co-bonded with carbonized electrospun PAN nanofibers.

From Figures 2.6, 2.7, and 2.8, it can be seen that the initial rise in voltage in 20s is 14.8 mV, corresponding to a stress of 10 MPa and a strain rate of -0.03 mm/min. A study was conducted on a functionalized graphene-reinforced nanocomposite of polyvinylidene difluoride (PVDF) as strain sensor for structural health monitoring [14]. In that study, the PVDF nanocomposite sample containing 2 wt% of the functionalized graphene showed that at strains of 0.02% and 0.85%, voltage changes of about 9 mV and 24 mV, respectively, were observed in the carbon fiber films [14]. As can be seen in Figures 2.6 and 2.7, studies here showed that at strains of 0.02% and 0.85%, voltage changes of about 18 mV and 25 mV, respectively, were observed in the carbonized PAN nanofibers on the carbon fiber composites. This behavior results in a nonlinear feature of voltage change in the inelastic region of the specimen [14]. The change in voltage can be attributed to the loss of contact with the specimen (carbonized electrospun PAN

nanofibers) due to tensile loading, internal and external fractures on the nanofibers, initial defects, and the change in electrical properties of carbonized PAN nanofibers under tensile loading. The heat treatment can condense/integrate the PAN nanofibers on the composites and develop a conducting network since the fibers contain only carbonaceous matter. However, as the compression and tensile loads were applied, this conductive network was apparently disturbed, thereby resulting in voltage, conductivity, and resistivity changes.

Figure 2.9 shows the changes in resistance vs. time of the composite specimen co-bonded with the carbonized electrospun PAN nanofibers. As can be seen, the specimen had an initial resistance of 30 ohms measured with a four-point probe. The contact resistance was not taken into account, and the high-precision equipment usually allows voltage reading in mV ranges. Recent studies have shown that the change in voltage due to the change in dimension was small compared to the change in resistivity of the specimen due to external loadings [36]. Thus, the change in voltage is mainly attributed to the change in resistivity/conductivity values. The contribution of Poisson's effect also plays a significant role [36]. The resistivity and changes in dimension may be related to when the material contains cracks, internal defects, and secondary phase formations [30, 31]. However, the relationship between dimensional changes and resistivity changes due to loading and unloading requires more research. Li et al. [35] investigated the strain-dependent electrical resistance of MWCNT/polyethylene oxide (PEO) composite film using an experimental setup to measure the electrical resistance and strain simultaneously and found repeated relations in resistance versus strain. Dharap et al. [36] conducted an experimental work on MWCNT film as strain sensors and studied its response to elastic loading and electrical response against dynamic loading.

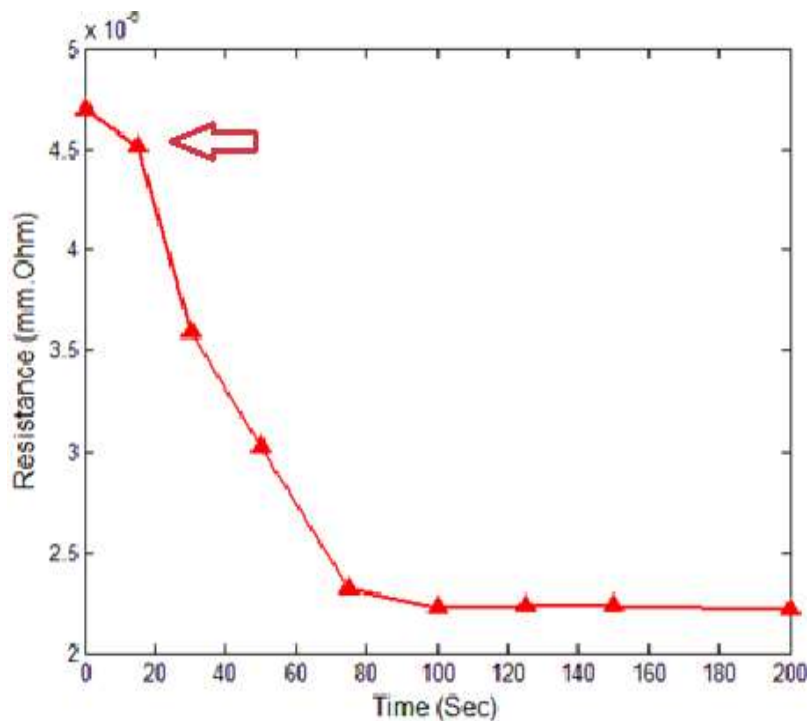


Figure 2.9. Change in resistance vs. time of composite specimen co-bonded with carbonized electrospun PAN nanofibers.

Figure 2.10 shows the current (mA) vs. voltage (mV) of the composite specimen co-bonded with carbonized electrospun PAN nanofibers. Nanofibers may not be homogeneous materials, so the data presented here mainly show non-ohmic behavior. Even after heat treatment below 1,000°C, the fibers are not entirely composed of carbon, and other elements remaining in the carbon fiber structures can substantially cause heterogeneity, hence the reason for observing non-ohmic behavior. When the PAN nanofibers were, heat treated between 600°C and 800°C, they acted more like conductors. Thus, heterogeneity was evidently the most pivotal factor in determining the properties [32].

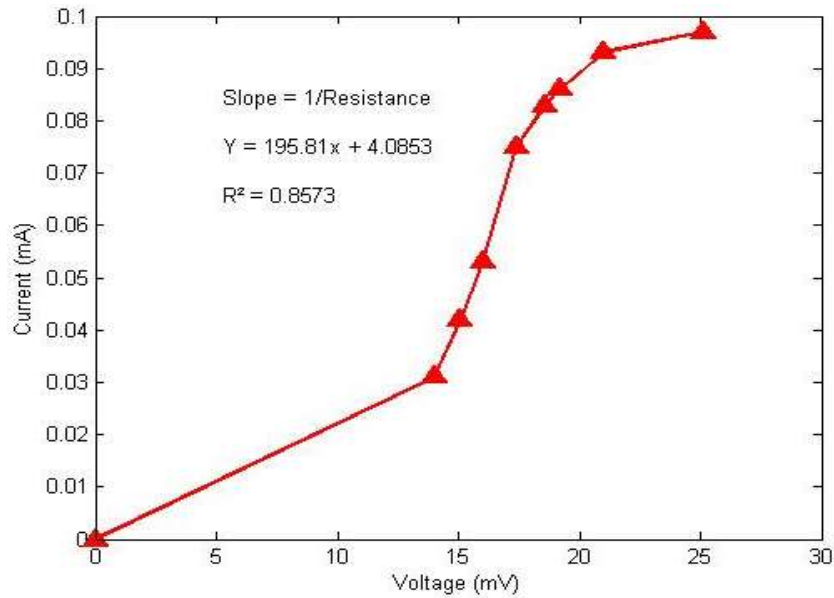


Figure 2.10. Current (mA) vs. voltage (mV) of composite specimen co-bonded with carbonized electrospun PAN nanofibers.

Vilaplana et al. stated that carbon fibers decreased electrical properties under applied loads, reporting an electrical resistivity value of $0.0000152 \text{ m}\cdot\Omega$ [32]. Luhrs et al. studied the oxidation and carbonization processes in an ambient condition at 300°C and in an inert atmosphere at 750°C , respectively [33]. The strain gauge of their test setup provided a linear relationship between electrical resistances and strain values. The electrical resistance values were drastically reduced as a function of time [33]. The electrical conductivity values of carbonized electrospun PAN nanofibers can be significantly changed when they are mechanically loaded [34]. These changes are mainly related to the degrees of stress and strain rates, internal and external deformations, time, and other environmental conditions. Highly conductive materials with other superior physical properties can be ideal materials for use as sensing elements and nanoprobbers in the SHM of composite aircraft and wind turbine structures. The resistivity and conductivity changes on the carbonized PAN nanofibers may indicate the degree of aging

process of the composites, the level of maneuvering during the flights/operations, impacts of environmental conditions (e.g., storm, tornado, hurricane, heavy rain and snow, hail, etc.) and other internal and external loads.

2.4 Conclusions

Electrospun PAN nanofibers were stabilized at 280°C for 1 hr in an ambient condition and then carbonized at 850°C in inert argon gas for 1 hr to produce highly conductive carbon nanofibers for the structural health monitoring of composite aircraft and wind turbines. The carbonized PAN nanofibers that were cohesively bonded on the surface of the carbon fiber composite panels were loaded under different tensile and compression loads. A four-circumferential probe measurement system was used to determine the electrical response of the composite panels during the uniaxial loadings. The prepared samples detected very small strain rates that formed on the composite panels in the form of electrical voltage, resistivity, and conductivity changes. This may be because of the extremely high surface area of the carbonized PAN nanofibers. Also, Poisson's effect and internal defects such as pores, cracks, and beads can also play a significant role in electrical signal changes of the composite panels.

This study showed that at 0.02% and 0.85% of strain, voltage changes of about 18 mV and 25 mV, respectively, were observed in the carbonized PAN nanofibers on the carbon fiber composites. This behavior leads to a nonlinear feature of voltage change when in the inelastic region of the specimen. The change in voltage can be attributed to tensile loading, internal and external fractures on the nanofibers, initial defects, and the change in electrical properties of carbonized PAN nanofibers under tensile loadings. The shear stress tests can be applied to the composite panels to further characterize properties of the novel nanomaterials. These

nanomaterials and methods may open up new possibilities for developing highly sensitive SHM devices for composite aircraft, wind turbines, and other infrastructures.

2.5 References for Chapter 2

- [1] Raghavan, A., and Cesnik, C. E., "Review of Guided-Wave Structural Health Monitoring," *Shock and Vibration Digest*, Vol. 39, No. 2, 2007, pp. 91-116.
- [2] Farrar, C. R., and Lieven, N. A., "Damage Prognosis: The Future of Structural Health Monitoring," *Philosophical Transactions of the Royal Society of London A: Mathematical, Physical and Engineering Sciences*, Vol. 365, 2007, pp. 623-632.
- [3] Farrar, C. R., "Damage Prognosis: Current Status and Future Needs," Los Alamos National Laboratory Report, 2003, LA-14051-MS.
- [4] Farrar, C. R., and Worden, K., "An Introduction to Structural Health Monitoring," *Philosophical Transactions of the Royal Society of London A: Mathematical, Physical and Engineering Sciences*, Vol. 365, 2007, pp. 303-315.
- [5] Rees, D., Chiu, W. K., and Jones, R., "A Numerical Study of Crack Monitoring in Patched Structures Using a Piezoelectric Sensor," *Smart Materials and Structures*, Vol. 1, No. 3, 1992, pp. 202.
- [6] Marantidis, C., Van Way, C. B., and Kudva, J. N., "Acoustic-Emission Sensing in an On-Board Smart Structural Health Monitoring System for Military Aircraft," *1994 North American Conference on Smart Structures and Materials*, 1994, pp. 258-264.
- [7] Ellerbrock, P. J., "DC-XA Structural Health-Monitoring Fiber Optic-Based Strain Measurement System." *Proceedings of the SPIE 3044, Smart Structures and Materials 1997: Industrial and Commercial Applications of Smart Structures Technology*, 207, 1997, Vol. 97, 1997, pp. 207-218.
- [8] Kollar, L. P., and Van Steenkiste, R. J., "Calculation of the Stresses and Strains in Embedded Fiber Optic Sensors," *Journal of Composite Materials*, Vol. 32, No. 18, 1998, pp. 1647-1679.
- [9] Schoess, J. N., and Zook, J. D., "Test Results of a Resonant Integrated Microbeam Sensor (RIMS) for Acoustic Emission Monitoring," *5th Annual International Symposium on Smart Structures and Materials*, Vol. 9, No. 11, 1998, pp. 947-951.

- [10] Hautamaki, C., Zurn, S., Mantell, S. C., and Polla, D. L., "Experimental Evaluation of MEMS Strains Sensors Embedded in Composites," *Journal of Microelectromechanical Systems*, Vol. 8, No. 3, 1999, pp. 272-279.
- [11] Seydel, R. E., and Chang, F. K., "Implementation of a Real-Time Impact Identification Technique for Stiffened Composite Panels," *Proceedings of the 2nd International Workshop on Structural Health Monitoring*, Stanford University, CA, 1999, pp. 225-233.
- [12] Chiu, W. K., Galea, S. C., Koss, L. L., and Rajic, N., "Damage Detection in Bonded Repairs Using Piezoceramics," *Smart Materials and Structures*, Vol. 9, No. 4, 2000, pp. 466-475.
- [13] Chang, F. K., "Structural Health Monitoring: A Road to Intelligent Structures," *Proceedings of the 9th International Workshop on Structural Monitoring*, Stanford University, CA, 2013.
- [14] Eswaraiah, V., Balasubramaniam, K., and Ramaprabhu, S., "Functionalized Graphene Reinforced Thermoplastic Nanocomposites as Strain Sensors in Structural Health Monitoring," *Journal of Materials Chemistry*, Vol. 21, No. 34, 2011, pp. 12626-12628.
- [15] Beese, A. M., Papkov, D., Li, S., Dzenis, Y., and Espinosa, H. D., "In situ Transmission Electron Microscope Tensile Testing Reveals Structural-Property Relationship in Carbon Nanofibers," *Carbon*, 2013, Vol. 60, pp. 246-253.
- [16] Nataraj, S. K., Yang, K. S., and Aminabhavi, T. M., "Polyacrylonitrile-Based Nanofibers-a State-of-the-Art Review," *Progress in Polymer Science*, Vol. 37, No. 3, 2012, pp. 487-513.
- [17] Chand, S., "Review Carbon Fibers for Composites," *Journal of Materials Science*, Vol. 35, No. 6, 2000, pp. 1303-1313.
- [18] Yun, K. M., Hogan, C. J., Matsubayashi, Y., Kawabe, M., Iskandar, F., and Okuyama, K., "Nanoparticle Filtration by Electrospun Polymer Fibers." *Chemical Engineering Science*, 2007, Vol. 62.17, pp. 4751-4759.

- [19] Musale, D. A., and Kumar, A., "Solvent and pH Resistance of Surface Crosslinked Chitosan/Poly (Acrylonitrile) Composite Nanofiltration Membranes," *Journal of Applied Polymer Science*, Vol. 77, No. 8, 2000, pp. 1782-1793.
- [20] Huang, X., "Review: Fabrication and Properties of Carbon Fibers," *Materials*, Vol. 2, 2009, pp. 2369-2403.
- [21] Jayaraman, K., Kotaki, M., Zhang, Y., Mo, X., and Ramakrishna, S., "Recent Advances in Polymer Nanofibers." *Journal of Nanoscience and Nanotechnology*, Vol. 4, No. 1-2, 2004, pp. 52-65.
- [22] Anton, F., "Process and Apparatus for Preparing Artificial Threads," U.S. Patent No. 1,975,504, Oct. 2, 1934.
- [23] Huang, Z. M., Zhang, Y. Z., Kotaki, M., and Ramakrishna, S., "A Review on Polymer Nanofibers by Electrospinning and Their Applications in Nanocomposites," *Composites Science and Technology*, Vol. 63, No. 15, 2003, pp. 2223-2253.
- [24] Zussman, E., Chen, X., Ding, W., Calabri, L., Dikin, D. A., Quintana, J. P., and Ruoff, R. S., "Mechanical and Structural Characterization of Electrospun PAN-Derived Carbon Nanofibers," *Carbon*, Vol. 43, 2005, pp. 2175-2185.
- [25] Liu, Y., "Stabilization and Carbonization Studies of Polyacrylonitrile/Carbon Nanotube Composite Fibers," Ph.D. Dissertation, School of Polymer, Textile and Fiber Engineering, Georgia Institute of Technology, Atlanta, GA, 2010.
- [26] Arshad, S. N., Naraghi, M., and Chasiotis, I., "Strong Carbon Nanofibers from Electrospun Polyacrylonitrile," *Carbon*, Vol. 49, No. 5, 2011, pp. 1710-1719.
- [27] Griffith, A. A., "Phenomena of Rupture and Flow in Solids," *ASM Transactions Quarterly*, Vol. 61, No. 4, 1968, pp. 871-906.
- [28] Tagawa, T., and Miyata, T., "Size Effect on Tensile Strength of Carbon Fibers," *Material Science and Engineering A-Structural Materials Properties Microstructure and Processing*, Vol. 238, No. 2, 1997, pp. 336-342.
- [29] Arshad, S. N., Naraghi, M., and Chasiotis, I., "Strong Carbon Nanofibers from Electrospun Polyacrylonitrile," *Carbon*, Vol. 49, No. 5, 2011, pp. 1710-1719.

- [30] Zhang, W., Sakalkar, V., and Koratkar, N., "In Situ Health Monitoring and Repair in Composites Using Carbon Nanotube Additives," *Applied Physics Letters*, Vol. 91, No. 13, 2007, pp. 133102.
- [31] Li, Z., Dharap, P., Sharma, P., Nagarajaiah, S., and Yakobson, B. I., "Continuum Field Model of Defect Formation in Carbon Nanotubes," *Journal of Applied Physics*, Vol. 97, No. 7, 2005, pp. 074303.
- [32] Vilaplana, J. L., Baeza, F. J., Galao, O., Zornoza, E., and Garcés, P., "Self-Sensing Properties of Alkali Activated Blast Furnace Slag (BFS) Composites Reinforced with Carbon Fibers," *Materials*, Vol. 6, No. 10, 2013, pp. 4776-4786.
- [33] Luhrs, C. C., Daskam, C. D., Gonzalez, E., and Phillips, J. "Fabrication of a Low Density Carbon Fiber Foam and Its Characterization as a Strain Gauge," *Materials*, Vol. 7, No. 5, 2014, pp. 3699-3714.
- [34] Alexopoulos, N. D., Bartholome, C., Poulin, P., and Marioli-Riga, Z., "Structural Health Monitoring of Glass Fiber Reinforced Composites Using Embedded Carbon Nanotube (CNT) Fibers," *Composites Science and Technology*, Vol. 70, No. 2, 2010, pp. 260-271.
- [35] Li, X., Levy, C., and Elaadil, L., "Multiwalled Carbon Nanotube Film for Strain Sensing," *Nanotechnology*, Vol. 19, No. 4, 2008, pp. 045501-045507.
- [36] Dharap, P., Li, Z., Nagarajaiah, S., and Barrera, E. V., "Nanotube Film Based on Single-Wall Carbon Nanotubes for Strain Sensing," *Nanotechnology*, Vol. 15, No. 3, 2004, pp. 379-382.

CHAPTER 3

THERMAL, ELECTRICAL, AND SURFACE HYDROPHOBIC PROPERTIES OF ELECTROSPUN POLYACRYLONITRILE NANOFIBERS FOR STRUCTURAL HEALTH MONITORING

3.0 Abstract

In this chapter, thermal, electrical, and surface properties of electrospun polyacrylonitrile fibers are highlighted. Electrospun PAN fibers are lightweight, less costly, and do not interfere with the functioning of infrastructure. This study deals with the fabrication of PAN-based nanofibers via electrospinning followed by stabilization and carbonization in order to remove all non-carbonaceous material and ensure pure carbon fibers as the resulting material to be used as strain sensors in structural health monitoring applications. SHM refers to the use of in-service embedded monitoring by means of sensors for effectively managing structural systems against all kinds of damages on a real-time basis. A material that displays a change in resistance with the change in its dimension is called as a piezoresistive material. Carbon nanofibers, like other quasi-one-dimensional nanostructures such as nanowires and nanotubes, have recently been receiving considerable attention due to their applications in composite reinforcement, membrane-based separation, and heat-management materials, and more recently as strain sensors due to their piezoresistive properties. Carbon-based piezoresistive sensors such as graphite, graphene, and carbon nanotubes are developing as an alternative for conventional metal/silicon-based microelectromechanical systems (MEMS) due to their high performance and easy manufacturing process with applications ranging from industrial to medical fields.

These sensors can be used in in-situ structural health monitoring in industries and in prosthesis applications due to their small size and high sensitivity to minuscule forces.

Electromechanical sensors such as pressure sensors, force sensors, strain gages, etc., work on the principle of piezoresistivity. Some industrial and medical applications require devices that sense very small scale forces and produce output signals. In those cases, small-sized and highly sensitive materials are required. Traditional silicon/metal-based sensors are marred with low sensitivity, a time-consuming fabrication process, and susceptible to influences due to external electrical and mechanical fields. In this context, researchers are very interested in carbon-based materials like carbon nanotubes, graphene, and graphite for piezoresistive applications due to their unique electromechanical properties that exhibit a change in resistance with a change in dimension on a very small scale.

In this chapter, PAN-derived carbon fibers are discussed as a possible alternative for conventional sensors because of their thermal, electrical, and surface properties. Electrochemical impedance spectroscopy was used to determine the ionic conductivity of PAN fibers. X-ray diffraction (XRD) analysis indicates that the repeated peaks near 42° on the activated nanofiber film were α and β phases with crystalline forms. Contact angle, thermogravimetric analysis (TGA), differential scanning calorimetry (DSC), and Fourier transform infrared spectroscopy (FTIR) were also employed to examine the surface, thermal, and chemical properties of the carbonized electrospun PAN fibers. Test results indicate that the carbonized PAN nanofibers have superior physical properties, which may be useful for SHM applications in different industries.

3.1 Introduction

The process of employing an organized damage detection system for various types of infrastructure is generally referred to as structural health monitoring [1]. SHM provides

continuous monitoring of structures in real time, thereby increasing public safety, especially for aging structures that are still in use [2-5]. SHM ensures early detection of routine damage and reduces the costs and downtime associated with maintenance. SHM can predict unusual behavior of various structures, providing advanced warning and allowing for the removal/repair of structural parts for the public's protection [5]. In addition to monitoring any unsafe structural behavior, SHM also allows for the assessment of structural integrity after natural disasters, such as earthquakes, floods, tornados, and hurricanes. The need for SHM is obviously important, with the primary objectives of such a system being to increase further safety and reliability, and to reduce repair and inspection costs [5].

Carbon nanofibers possess high stiffness and strength with outstanding electrical and thermal properties; therefore, they have numerous applications in a wide range of fields, such as structural components, electronics, medical, filtration, and lithium-ion batteries [6-10]. Carbon fibers are also being used as reinforcement in manufacturing lightweight composites for aircraft and wind turbines. Tse-Hao first developed modern PAN-derived carbon fibers after pyrolyzing polyacrylonitrile (PAN) fibers at elevated temperatures in an inert atmosphere [11]. After this, the development of commercial carbon fibers was reported by Watt or Tse-Hao et al. [11].

The main precursor for the production of carbon fibers is polyacrylonitrile. Electrospinning, which involves using an electric current to draw a liquid into a thin fiber, is a promising technique for the production of carbon nanofibers from a PAN polymer precursor [6-7]. PAN-derived carbon nanofibers were synthesized via electrospinning followed by stabilization/oxidation and carbonization to remove all non-carbonaceous matter and ensure a high percentage of carbon in the resulting material. The stabilization process of PAN fibers is

extremely important in order to fabricate high-quality carbon fibers. In this process, a lower temperature treatment (200–300°C) in an ambient condition results in the formation of the ladder-like structure of PAN [11]. During the stabilization process, PAN precursor fibers undergo significant physical and chemical changes and become physically, chemically, and thermally stable when exposed to a high temperature [12]. The PAN fibers are transformed from thermoplastic to thermosetting and change color as well during the heating process. Additionally, PAN fibers are shrunk during the stabilization process, resulting in weight loss and fiber-diameter reductions. The critical parameters in stabilization are temperature, heating steps, heating rate, inert atmosphere and holding time.

After the stabilization process, carbonization is carried out at a higher temperature (800–3000°C) in an inert atmosphere [11]. The carbonization temperature depends upon the types of carbon fibers required. The properties of the carbon fibers depend on the nature of the precursor fibers and the process parameters used in stabilization and carbonization [11]. In the present study, electrospun PAN nanofibers were converted into carbon fibers by stabilizing and carbonizing at high temperatures, which results in high-strength materials resulting from the higher carbon content. PAN contains around 68 wt% carbon, and after heat treatment, the carbon content escalates to around 92 wt%. The aim of this study was to fabricate electrospun PAN nanofibers (PAN-derived carbon fibers), heat-treat them to remove all non-carboneous material, and investigate their thermal, electrical, surface, and structural properties for potential applications in SHM systems.

3.2 PAN Electrospun Fibers as a Strain Sensor in SHM Applications

SHM has gained tremendous attention recently as a means to accurately monitor structures and provide an early warning of any detrimental condition using real-time response data. By using structurally integrated sensors, the health of a structure can be interpreted by means of sensor signals, and real-time data inspection can reduce the extra cost of inspection. Strain, is one of the most important parameters to investigate in the health of a structure [37]. Repetitive strains with high magnitudes may lead to fatigue or yielding in the material [37]. Mechanical strains can be used to determine structural loads and stresses in the structure [37]. Conventional strain sensors, which are generally made from metal foils, possess several drawbacks such as limited sensitivity, high-temperature dependence, and large power consumption [37]. Therefore, they are deficient in terms of low power consumption and high performance [37-39]. An efficient sensor for SHM has great potential for applications in monitoring aerospace structures subject to fatigue, impact, severe loads, and structural disintegration.

Strain sensing is generally attained by attaching strain gauges to the structure [40]. Wen and Chung [40] used carbon fibers in a cement structure and studied their sensing performance. Recently, many studies have been done with carbon nanotubes embedded in a polymer matrix to investigate sensing performance. Among various carbon fiber precursors, polyacrylonitrile has been used extensively in the last several decades for producing carbon fibers, owing to its large carbon yield. With the advent of the electrospinning technique for producing fibers, ultrafine nano-sized fiber webs with a much smaller diameter in comparison to conventional PAN-based carbon fibers and higher specific surface area have been produced. Carbon fibers are electrically

conductive, and when subject to loads or strains, they experience a change in the electrical resistance, thus enabling strain sensing [41]. The electrical conduction of carbon fiber is due to its high-order graphite microstructure [42]. Loadings or strains therefore induce a shift in electrical resistance within the fiber, thus enabling it to be used as a sensor [42]. Moreover, carbon fibers display piezoresistive properties [42]. Mäder et al. [42] studied the strain-sensing performance of single carbon fibers coated with conductive material for structural health monitoring applications. The strain-sensing performance of carbon fiber composites depends on several factors such as fiber volume fraction, continuous fibers, discontinuous fibers, randomly oriented fibers, short fibers, and unidirectional fibers. When highly thermal and electrical conductive carbon fibers are used in composites with a higher volume fraction, the carbon fiber-reinforced plastic becomes somewhat conductive. Epoxy is an insulator, whereas carbonized PAN-derived carbon fibers are conductive. Electrical SHM depends on materials behaving like sensors. When microcracks and/or delamination occurs during service of a composite structure, the electrical conduction is impeded because the damaged area restricts the flow of electrons. When carbonized PAN-derived carbon fibers are used in the composite structure, they can serve as sensors to detect microcracks and/or delamination.

3.3 Experimental Materials and Methods

3.3.1 Materials

Polyacrylonitrile (CAS no. 25014-41-9, 0.2%, molecular weight 150,000 g/mole) and dimethylformamide (CAS no. 68-12-2, 99.8%) were purchased from Sigma-Aldrich and used in the tests without any further purification or modifications.

3.3.2 Carbonization of PAN Nanofibers

PAN powder was dissolved in DMF in a 90:10 weight ratio at 500 rpm for 1 hr. Special care was taken to ensure a homogeneous blend (polymeric solution). Nanofibers were fabricated using electrospinning at 25 kV with 1 ml/hr feed rate and a tip-to-collector distance of 25 cm. The as-produced nanofibers were later converted into carbon nanofibers by first stabilizing (or oxidizing) in an oxygen atmosphere at 270°C for 1 h. Then, the carbonization of PAN fibers was performed by heating the stabilized PAN fibers at 750°C, 850°C, and 950°C in an inert (argon) atmosphere for 1 hr. The heating ramp rate was 5°C/min. After the heat treatment, the non-carbon elements, such as hydrogen, oxygen, nitrogen, and sulfur, were eliminated and released as volatile matter, leaving behind nanofibers with a high carbon content [12-16]. Prior to the electrical and thermal tests, the carbonized nanofibers were treated with HCl in order to activate the carbon fibers and enhance electrical and thermal conductivities. The acid solution was prepared by mixing 3.5 g of HCl into 100 ml of DI water (see Table 1.1 shown previously). Scanning electron microscopy was used to determine the surface morphology of the PAN-derived carbon fibers. Figure 3.1 shows SEM images of the PAN fibers before and after carbonization at different temperatures.

A Rigaku MiniFlex II XRD system was used for the structural characterization tests. FTIR analysis was done by using a Thermo Scientific™ Nicolet™ iN10 infrared microscope in the range of 500–3500 cm^{-1} with an attenuated total reflectance mode. The thermal stability of PAN fibers was studied with TGA using a Q500 TA instrument. A DSC Q1000 (TA instrument) interfaced with a PC was used to measure the thermal properties of PAN fibers. A Gamry Instruments Potentiostat/Galvanostat, ZRA, Reference 600, was employed to measure the ionic

conductivity of PAN samples. The tensile test was done with an MTS Criterion Model 44 Advantage™ high elongation extensometer. The contact angle values of PAN fibers were measured with a water contact angle goniometer (KSV Instruments Ltd., Model #CAM 100). The contact angle goniometer is a compact video-based instrument that measures contact angles between 1° and 180° with an accuracy of $\pm 1^\circ$. Computer software provided by KSV Instruments Ltd. precisely recorded and measured the contact angles, and also took pictures of the measured contact angles.

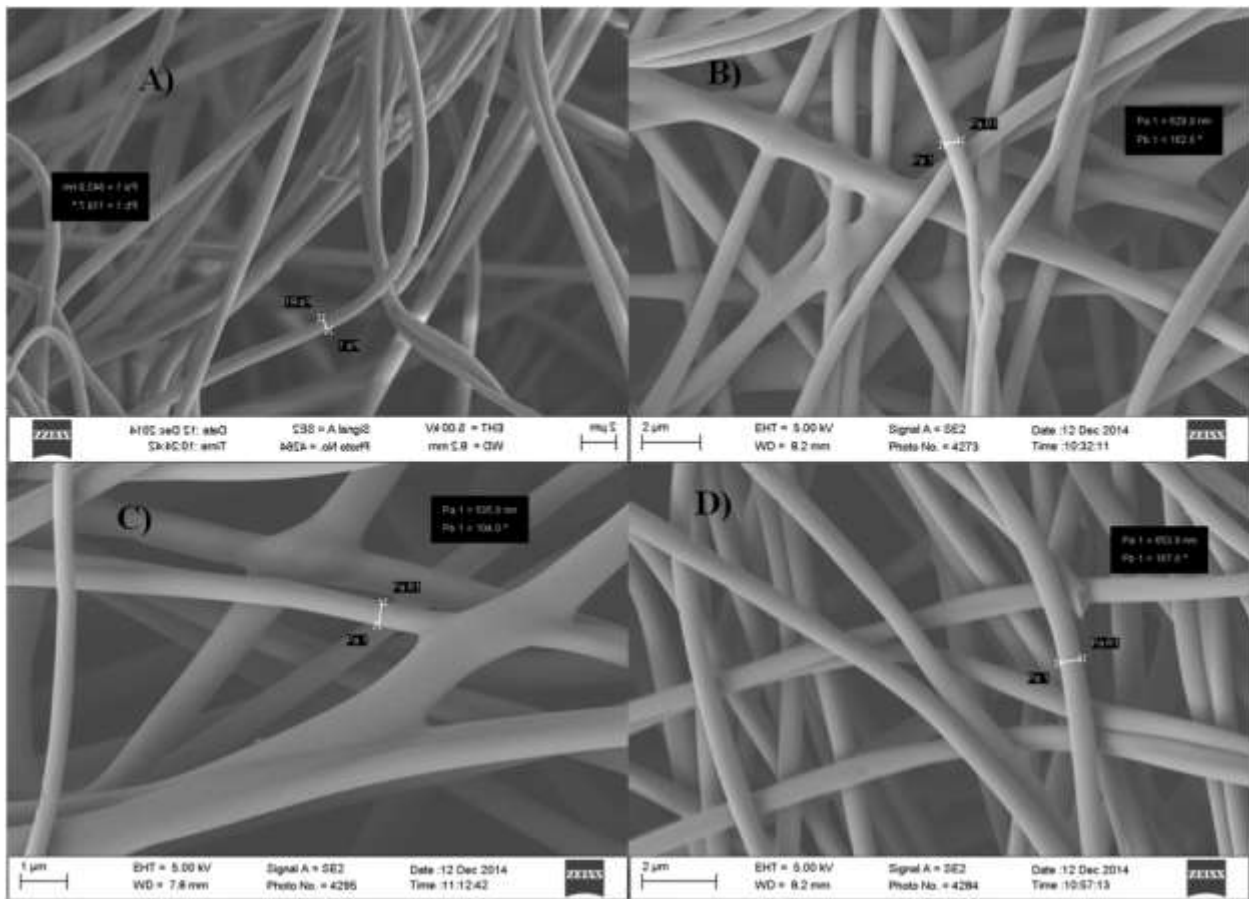


Figure 3.1. SEM images of PAN-derived carbon fibers: (a) electrospun, (b) after carbonization at 750°C for 1 hr, (c) after carbonization at 850°C for 1 hr, and (d) after carbonization at 950°C for 1 h.

The as-produced nanofibers were later converted to carbon nanofibers by stabilizing them in an oxygen atmosphere at 270°C for 1 h followed by carbonization at 750°C, 850°C, and 950°C in an inert (argon) atmosphere for 1 h, as shown in Figure 3.2. The ramp rate was 5°C/min. After heat treatment, the non-carbon elements, such as hydrogen, oxygen, nitrogen, and sulfur, were eliminated and released as volatile matter, leaving material with a high carbon content.

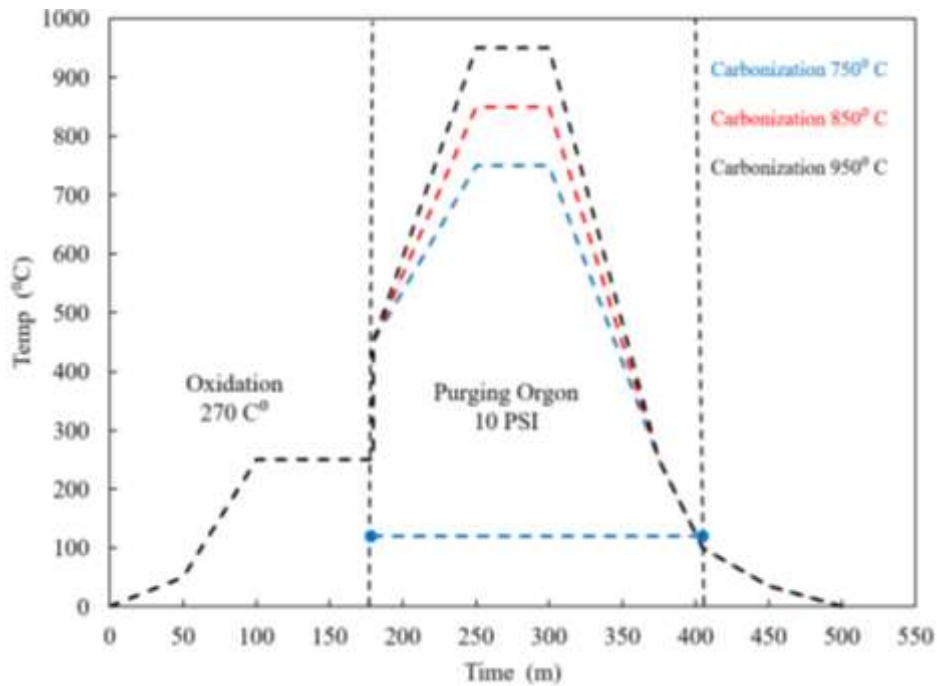


Figure 3.2. Heat treatment of carbonized fiber and conversion to carbon nanofibers by stabilizing in oxygen atmosphere at 270°C for 1 h followed by carbonization at 750°C, 850°C, and 950°C.

3.3.3 Fabrication of Nanocomposite for Sensors

The strain-sensing performance of PAN-derived carbon fibers was tested by fabricating nanocomposites employing the pre-preg technique. PAN-carbonized fibers were placed on top of the pre-preg carbon plies, which were laid up following a 0-, 45-, -45-, and 90-degree stacking sequence on an aluminum mold. The mold was cured in an oven for 2 h at 180°C. A four-circumferential ring probe was used to measure the resistance of the samples. A constant current

having small magnitude was applied along the axial direction through the outer probes, and variation in the voltage between the inner probes, corresponding to the change in strain, was recorded, as shown in Figure 3.3. Then quasi-static loading was applied, and the specimen was loaded at a constant rate of 1 mm/min.

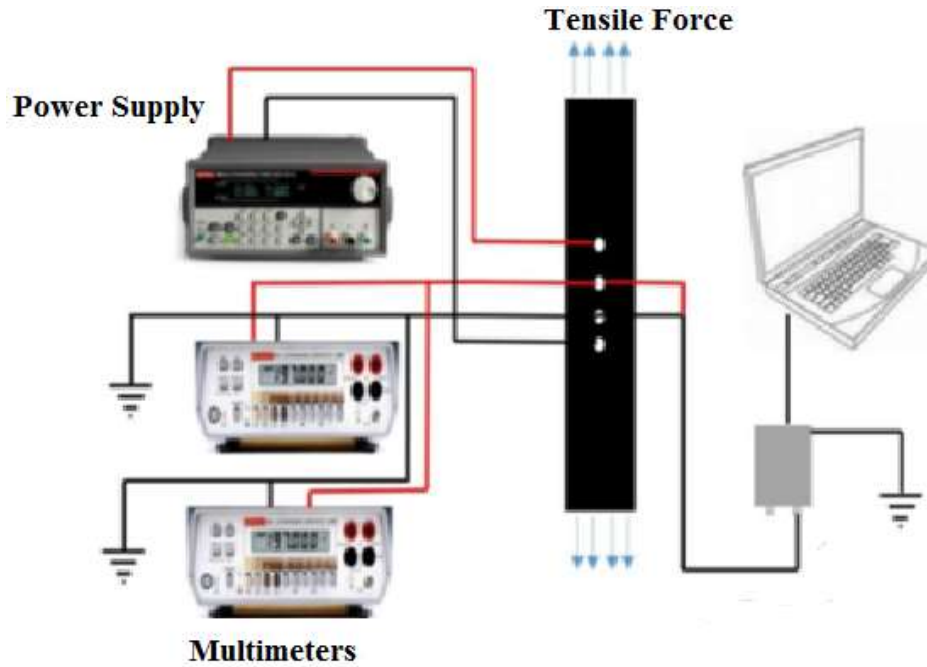


Figure 3.3. Experimental set up for strain sensor.

3.4 Results and Discussion

3.4.1 X-Ray Diffraction Analysis

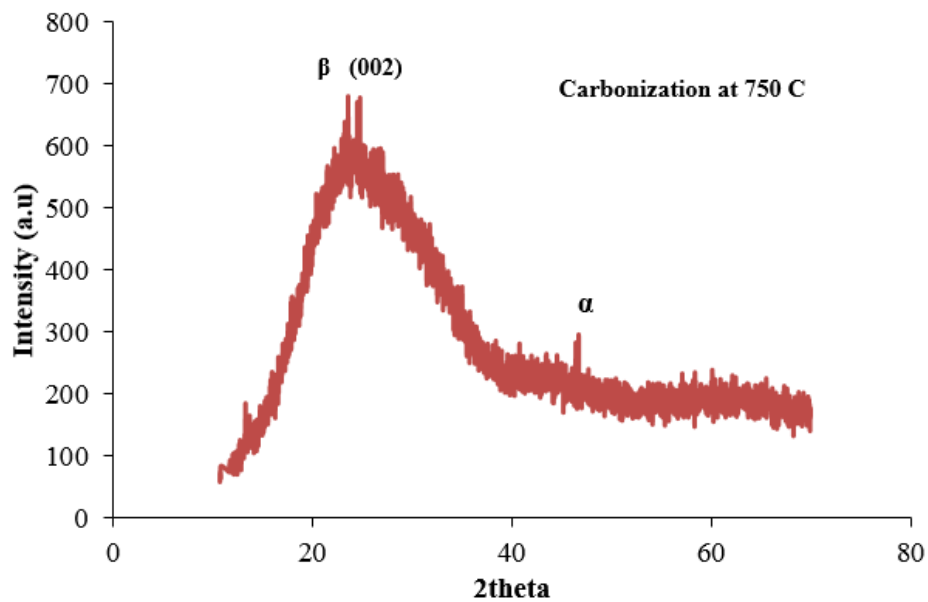
X-ray diffraction analysis was used to characterize the structure of the carbon materials in order to provide useful information regarding lattice constants and diffraction planes [17]. $\text{CuK}\alpha$ ($\lambda = 0.15418 \text{ nm}$) radiation was used over the 2θ range of 10° – 70° to observe the structural change during carbonization. An x-ray beam directed at a right angle to the samples produced reflections from the planes. The apparent crystallite thickness (L_c), apparent layer-plane length

parallel to the fiber axis (L_a), and average interlayer spacing (d) were calculated using Bragg and Scherrer formulas, expressed as equations (3.1) and (3.2), respectively [18]:

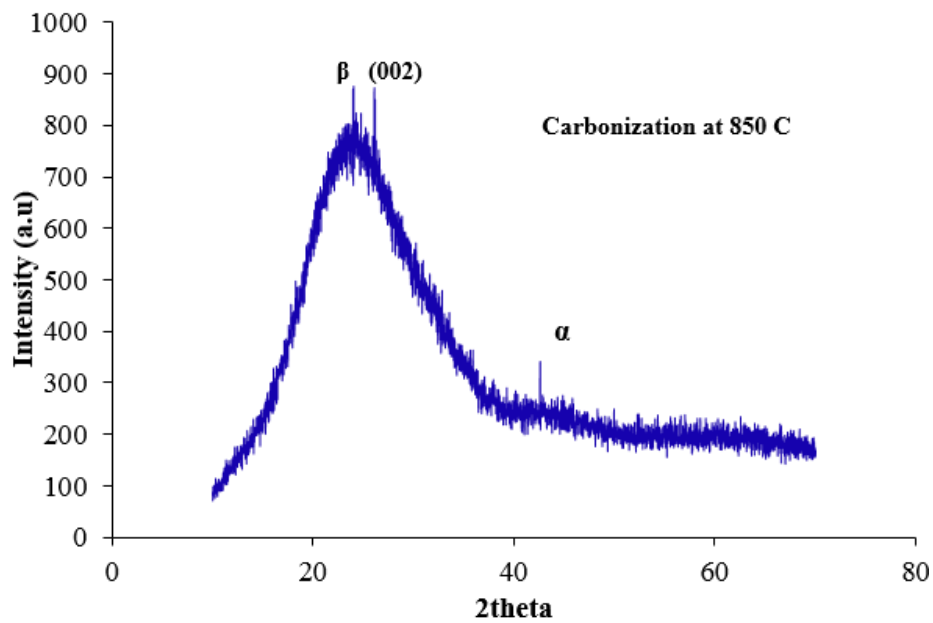
$$d = \frac{\lambda}{2 \sin\theta} \quad (3.1)$$

$$L = \frac{K\lambda}{\beta \cos\theta} \quad (3.2)$$

where θ is the Bragg angle in degrees, λ is the wavelength of the x-ray used, and β is the full-width half maximum of a given peak (rad). The shape factor K is 0.89 for L_c and 1.84 for L_a , respectively [18]. The Scherrer equation was used to calculate the values of L_c (stacking height of layer planes) from the width of the (002) reflection. Figure 3.4 shows the XRD patterns along the (002) plane of the PAN pre-carbonized fibers at various temperatures (750°C, 850°C, and 950°C). As can be seen, when the carbonization temperature increases, the (002) peaks shift from higher values of Bragg angles to slightly lower values of Bragg angles, indicating that carbon atoms arrange themselves into an increasingly ordered form as the carbonization temperature increases, resulting in improvement of the crystalline structure of the fibers [18]. According to Bragg's law, as 2θ decreases, the corresponding d-spacing increases (i.e., lower angles means a larger d-spacing). Table 3.1 provides the structural parameters of the XRD analysis for the carbonized PAN fibers.

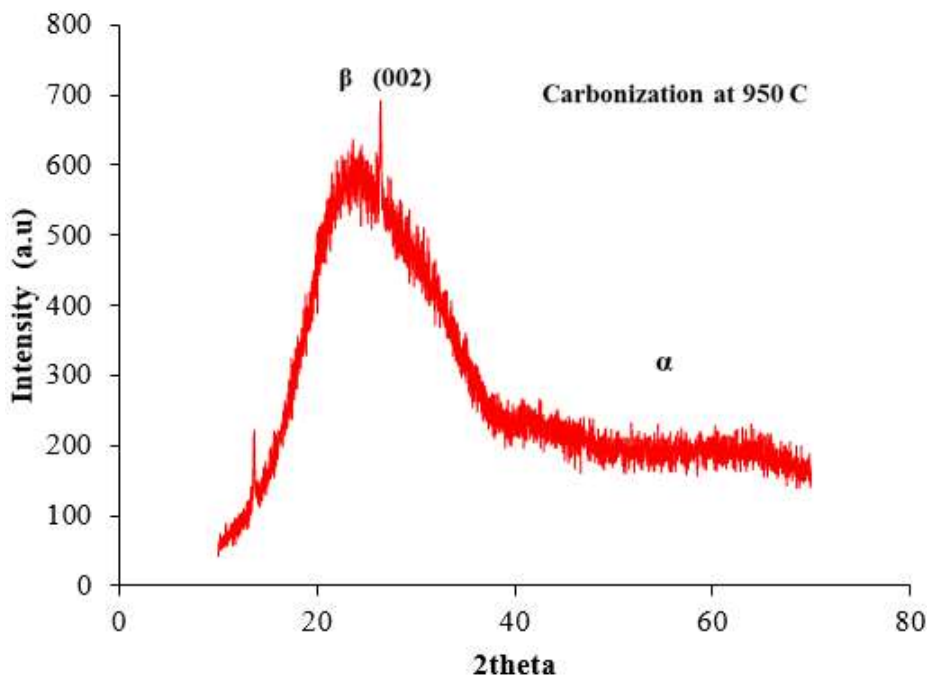


(a)



(b)

Figure 3.4. XRD pattern of PAN pre-carbonized fibers: (a) at 750°C; (b) at 850°C; at 950°C.



(c)

Figure 3.4. (Continued).

TABLE 3.1

STRUCTURE PARAMETERS DETERMINED BY XRD FOR PAN CARBON FIBERS

Temp. (°C)	$d_{(002)}$ nm	L_c nm	$L_c/d_{(002)}$
750	0.4053	2.66	1.87
850	0.4128	2.76	1.58
950	0.4226	2.76	1.58

3.4.2 Fourier Transform Infrared Analysis

FTIR spectra are a useful tool for determining the chemical interaction during the heat treatment of PAN fibers, making it possible to study the relaxation between chemical changes and strength [19]. As shown in Figure 3.5, the vibration characteristics of PAN fibers are those of the nitrile group, corresponding to 1668 cm^{-1} ; and the peak intensities at 2922 cm^{-1} , 1452 cm^{-1} ,

and 1093 cm^{-1} are assigned to the aliphatic CH group vibration of different modes in OH, CH_2 , and CH, respectively. The band at 1988 cm^{-1} is due to $\text{C}=\text{O}$ stretching, while the peak corresponding to 1668 cm^{-1} is due to nitrile stretching, indicating the presence of acrylonitrile.

The PAN molecule consists of methyl (CH_3) and nitrile ($\text{C}\equiv\text{N}$) groups in a linear arrangement [20]. During oxidation, some new compounds, such as ketones, aldehydes, and carboxylic acid, are formed. The carbonization process results in the evolution of volatile compounds, leaving behind primarily carbon and hydrogen molecules in the carbon fiber structure. However, a 100% conversion of PAN polymer to carbon may not be achieved due to the existence of other compounds [20]. Several distinct changes in the characteristic absorption peaks occur at some locations of the FTIR spectra following carbonization [13]. Significantly, most strong and sharp peaks disappear after carbonization (Figure 3.6).

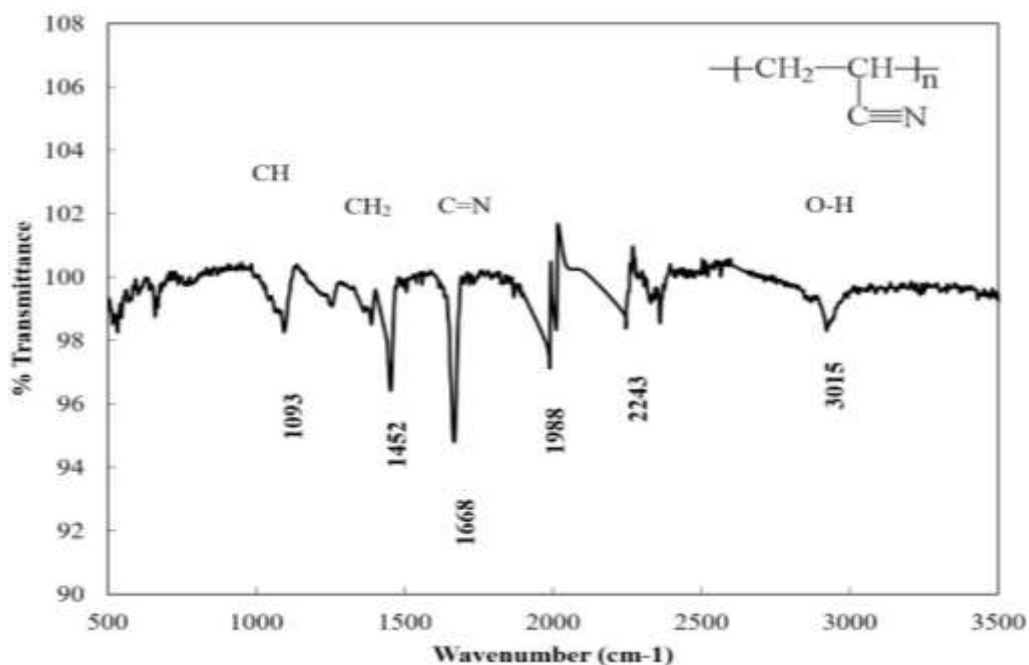


Figure 3.5. FTIR spectra of PAN fibers prior to carbonization.

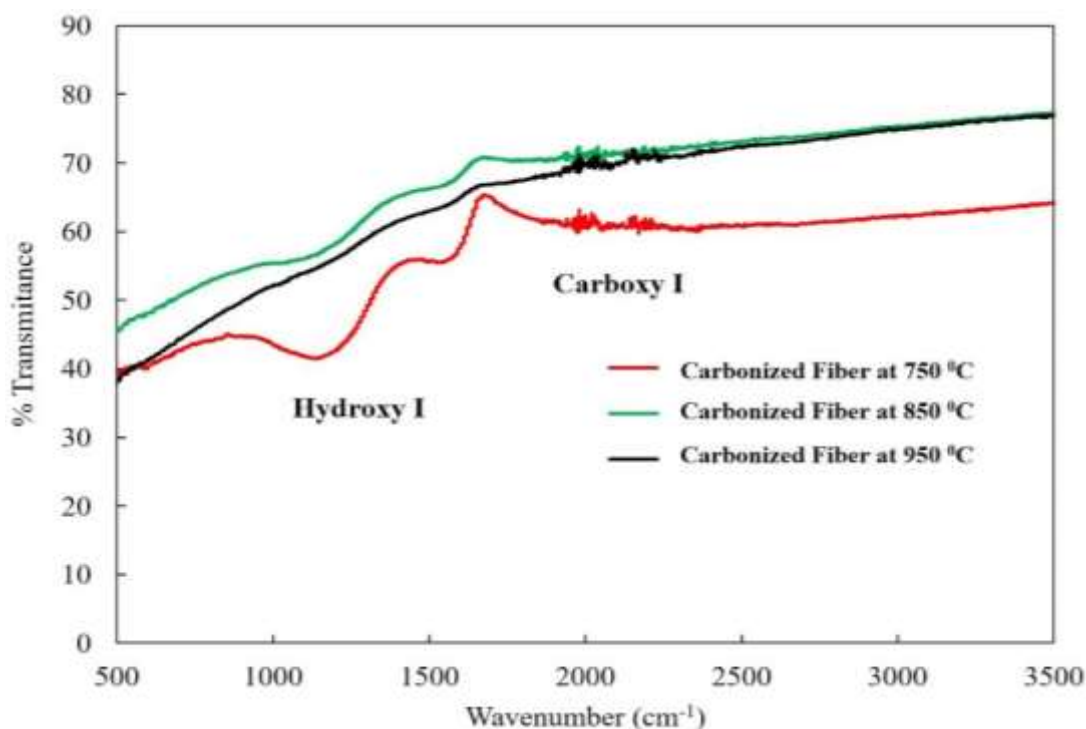


Figure 3.6. FTIR spectra of PAN fibers carbonized at 750°C, 850°C, and 950°C.

The strong peak from the nitrile groups observed at 1668 cm^{-1} (Figure 3.5) has almost disappeared after carbonization, especially at 850°C and 950°C. The peak at 1668 cm^{-1} decreased due to the reaction of the nitrile group during cyclization to form the conjugate C=N group [13]. No peak at 1668 cm^{-1} was observed in the 850°C curve, indicating that nitrile groups no longer exist and no ladder-like structure forms after carbonization at 850°C. A similar behavior was observed in the 950°C spectrum; however, several very small peaks are visible, which could be due to the sensitivity of the device or noise. The peak associated with the hydroxyl group at 2922 cm^{-1} completely disappeared after carbonization. The peak corresponding to 1452 cm^{-1} shows the bending vibration from the CH_2 group (Figure 3.5). FTIR spectra following carbonization at 750°C still exhibited distinct peaks, corresponding to 1093 cm^{-1} , 1452 cm^{-1} , and 1668 cm^{-1} , due to CH, CH_2 , and C=N group formations, respectively. However, as the carbonization increased

to 850°C and 950°C, the distinct peaks disappeared in the FTIR spectra, which can be attributed to the evolution of gasses and some liquid compounds and conversion into carbonaceous materials.

As can be seen in Figure 3.6, carbonization at 750°C indicated the presence of peaks in the FTIR spectra between 1093 cm^{-1} and 1700 cm^{-1} , meaning that 750°C was insufficient to fully carbonize the PAN fibers or that some reactions might not be complete. The lack of peaks over this range in the 850°C curve reveals that the PAN fibers have been almost fully carbonized. The reappearance of small peaks in the 950°C curve is most likely due to experimental conditions or sensitivity of the equipment/noise. The small wriggling behavior seen in the 950°C and 750°C curves may be attributed to the minute variations in the sample thickness, which was between 1.12 and 1.14 mm. PAN has a tendency to absorb moisture as well as water vapor from the environment. This could explain the wriggling behavior in the 950°C and 750°C curves. The heating rate was 5°C /min for all experiments. The magnitude of the peaks is still consistent with the PAN fibers being nearly fully carbonized at this condition.

3.4.3 Thermogravimetry Analysis

Thermogravimetry analysis offers a quantitative analysis of the amount of moisture and volatile compounds present in the fibers, weight loss, and thermal breakdown, and also assists in determining the degradation mechanism. It is important to note that an accurate heating rate is critical for TGA, which was employed to determine the weight loss pattern of the PAN fibers as a function of temperature. TGA was conducted on fiber samples at 25°C to 850°C with a nitrogen flow rate of 60 ml/min and a heating rate of 10°C/min. Test samples contained 3.237–5.5660 mg of fibers. Measurements were started at room temperature (25°C) and ramped to

850°C at a heating rate of 10°C/min using a nitrogen purge rate of 60 mL/min in a platinum pan.

Figure 3.7 shows the thermogravimetric curves of PAN fibers prior to carbonization.

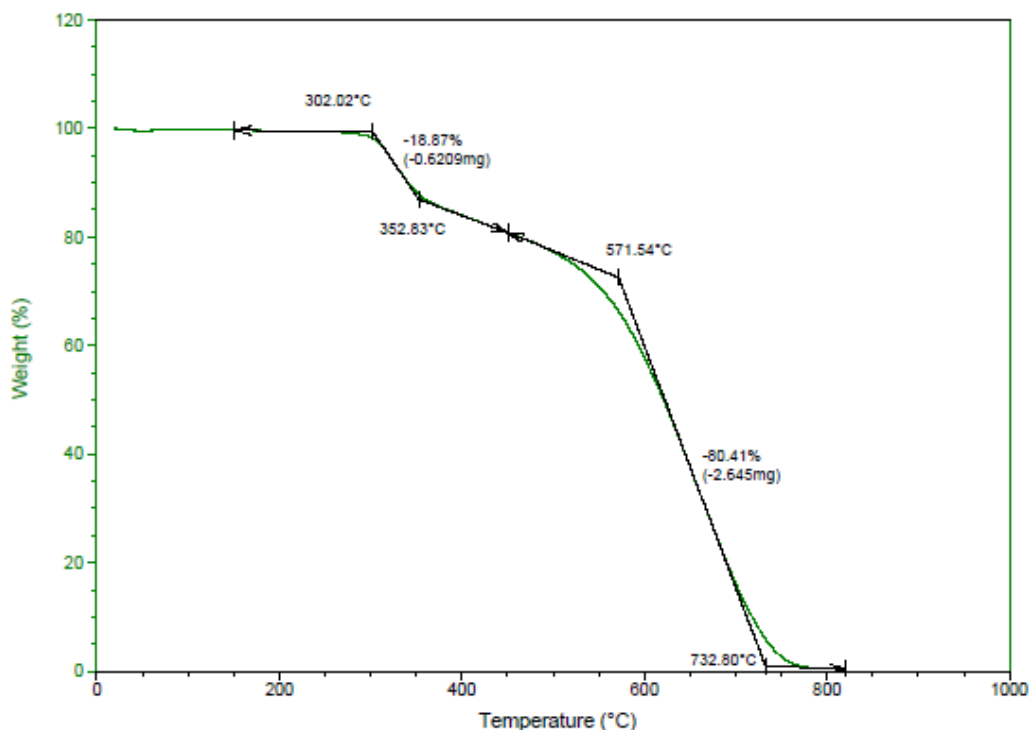


Figure 3.7. TGA curves of PAN fibers prior to carbonization.

The heating of the PAN fibers induced chemical reactions, such as cyclization, degradation, and thermal cross-linking, and the mechanisms of these processes depend on heating rate, medium, mass of the polymer, and type and nature of filler materials [22]. The TGA curve of PAN fibers shows a four-step weight-loss pattern. The TGA curves demonstrate that the weight loss caused by the pyrolytic reactions mainly occurred at around 302°C for pure PAN. The cyclization reactions continued until the residual nitrile groups did not react with other functional groups, and the pyrolytic reactions of the PAN fibers proceeded with minimum heating and shrinkage effects [23]. The cyclization of the fibers proceeded before any mass loss, and the factor responsible for cyclization process was the formation of aromatic rings [24]. In the

first stage up to 302.02°C, there was no weight loss. The cyclization reaction takes place in this step, and cyclization does not cause any weight loss, theoretically [25].

In the second stage (between 302.02°C and 352.83°C), weight loss was 18.87%, indicating that a chemical reaction occurred and volatile gasses were gradually released. It should be noted that the peak cyclization temperature is 294.63°C, as shown in the DSC thermogram in Figure 3.8.

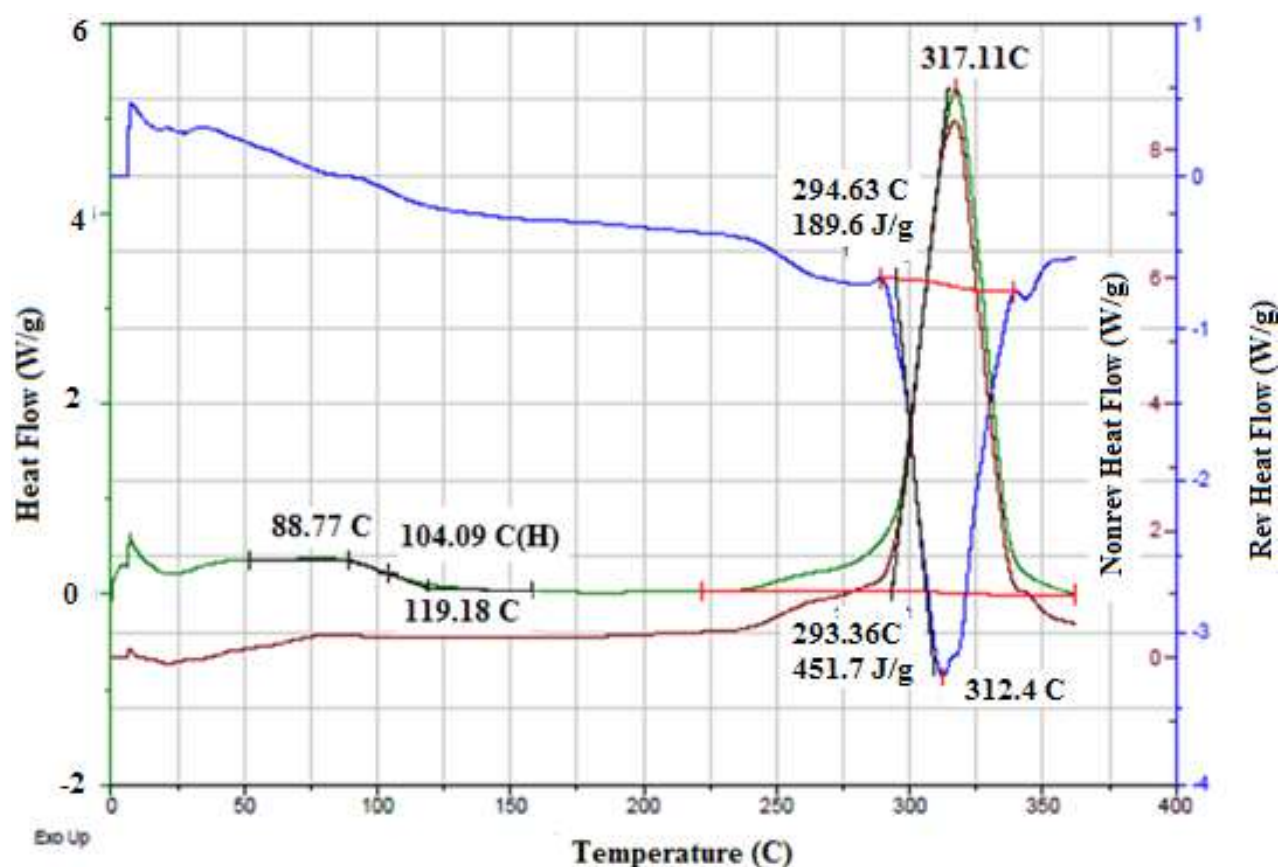


Figure 3.8. DSC thermogram of PAN fibers for heat flow, non-rev heat flow, and rev heat flow.

In the third stage, some weight loss was also observed between 382°C and 571°C, which could be attributed to partial evaporation of NH₃ and HCN [25]. In the fourth stage, between temperatures 571°C and 732°C, a steady decrease in weight was observed, with a total loss of

80.41%, indicating complete evaporation of polymer chain fragments from the PAN fibers. The TGA analysis of PAN fibers showed that the degradation process of the PAN fibers is exothermic and is accompanied by the evolution of volatile gaseous products.

3.4.4 Differential Scanning Calorimetry Analysis

A DSC Q1000 (TA instrument) interfaced with a PC was used to measure the thermal properties of the PAN fibers. Glass transition temperature (T_g) and melting temperature (T_m) were investigated at a heating rate of 20°C/min and a nitrogen flow rate of 50 ml/min. The samples were sealed in a T_{zero} Pan (TA Instruments), and the measurements were conducted in the temperature range of 25–350°C. A pre-determined weight of each sample was used in this experiment. The DSC heat flow and temperature were calibrated with an iridium standard prior to the tests. Figure 3.8 reveals the DSC thermogram of the PAN fibers.

As shown in Figure 3.8, the glass transition temperature of the PAN fibers is 104°C. No melting was observed with DSC as indicated by the green line. However, melting was observed with modulated DSC (Modulate 1.5°C/60 S) as indicated by the blue line. The PAN fibers show a broad exothermic peak at 312.4°C (Figure 3.8). The onset temperature was 294.63°C, and the reaction was completed at 330°C. The broadening of the exothermic peak may be due to the cyclization process. The broadening of the exothermic peak and corresponding temperature depends on the stabilization time. As the stabilization time, increased, the cyclization peak broadened, and the cyclization temperature considerably increased. The PAN fibers were cyclized only by a free radical mechanism, thereby indicating one peak at 312.4°C. The cyclization of nitrile groups is highly exothermic and leads to fragmentation of the chains owing to heat building up rapidly in the sample [26]. The single exothermic peak observed in the DSC

thermograms can be attributed to the cyclization of the PAN molecular chains [23]. It is well known that the cyclization reactions in PAN are based on free radicals and the initiated high temperature [27]. Therefore, the single exothermic peak observed in PAN can be attributed to the overlapping of the free radical cyclization and other exothermic reactions that can take place at high temperatures [27]. Cyclization is a highly exothermic process is accompanied by the evolution of a large amount of heat flow that can cause the cyclization of nitrile group in PAN [27]. In the TGA thermogram prior to carbonization (Figure 3.7), the cyclization continued without any weight loss until the temperature reached 302.02°C; nevertheless, the cyclization peak in the DSC thermogram (Figure 3.8) was observed at 312.4°C.

3.4.5 Ionic Conductivity Test

A Gamry Instruments Potentiostat/Galvanostat, ZRA, Reference 600, was employed to characterize the ionic conductivity of the PAN nanofibers. The experimental setup is shown in Figure 3.9.

From equation (3.3), the ionic conductivity can be calculated at different temperatures. The conductivity values of the polymeric fibers were calculated using the resistance obtained from a slope of the I-V plot.

$$\sigma = \frac{L}{R A} \quad (3.3)$$

where A is the area of the film and L is the thickness of the film. The addition of conducting moieties in the polymer matrix can also increase the ionic conductivity [28–30].

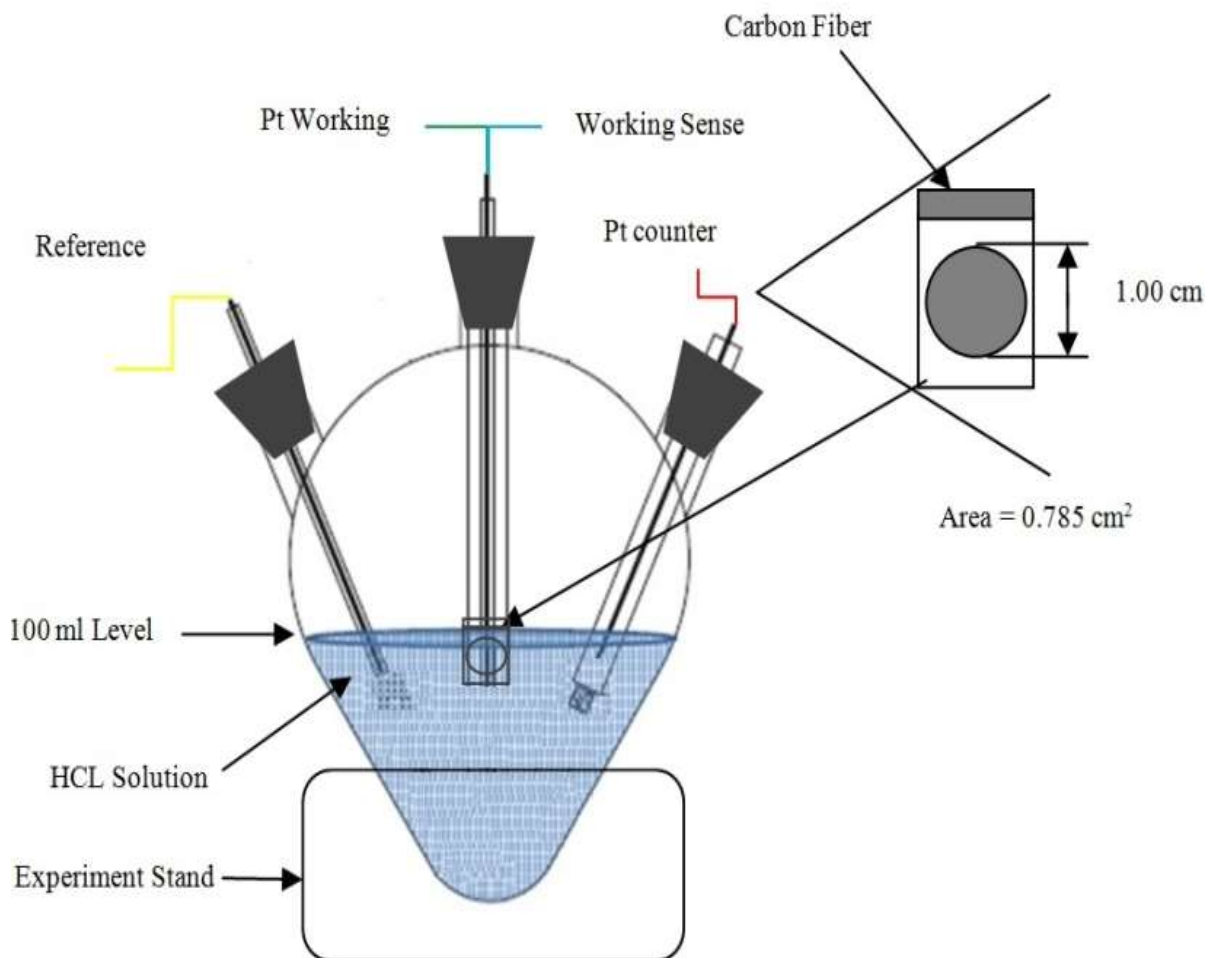


Figure 3.9. Experimental setup for electrochemical measurement (Gamry Instruments) of ionic conductivity [27].

Table 3.2. Show the conductivity values of PAN fibers carbonized at 850°C at different temperatures. Generally, conductivity increases with increasing temperature [31]. Changing carbonization environments does not have much influence on electrical and ionic conductivity values of the samples; however, the carbonization temperature is the only parameter that plays a major role in conductivity values [31]. The carbonized PAN nanofibers (inorganic phase) have much higher electrical conductivity than polymer nanofibers (organic phase) without any carbonization [32]. Carbonization at a high temperature generally increases the conductivity due

to the reduction of sp^3 bonds [32]. No significant changes in conductivity were observed between parallel and perpendicular directions. The electrical conductivity of most polymers is on the order of $\mu\text{S/cm}$. The electrical conductivity of individual PAN nanofibers after carbonization is 4.9 S/cm [33].

TABLE 3.2

CONDUCTIVITY VALUES OF CARBONIZED PAN FIBERS AT 850°C

Temperature (°C)	Conductivity (σ) S/cm ($\times 10^3$)
24.85	2.13
25.17	1.85
35.10	2.78
39.13	3.31
40.10	4.31
42.01	4.50
43.88	4.48
57.60	4.49
77.40	4.51

The conductivity of PAN-derived carbon fibers depends on the carbonization temperature of the carbon content of PAN-derived carbon fibers. Generally, the PAN-derived carbon fibers contain around 92 wt% carbon; however, when they are carbonized at 2000–3000°C, they could contain 99 wt% carbon. As shown in Table 3.2, conductivity values increase with increasing temperature. The highest value of conductivity is at 350.55°C, whereas the lowest value of conductivity is at 298°C. Carbonization was carried out at 850°C in this study, which means that the PAN fibers may still contain a small amount of impurities, and these impurities may reduce the conductivity values to some extent. If the carbonization is carried out at around 3000°C, the

fibers will have a pure graphite structure with nearly 99 wt% carbon, thereby showing the highest values of electrical conductivity.

3.4.6 Surface Hydrophobicity of Carbonized Fibers

Hydrophilic and hydrophobic properties of polymer surfaces are determined by the water contact angle between the water droplet and the polymeric fiber surface. A hydrophobic surface is one on which a droplet of water forms a contact angle greater than 90°, whereas a hydrophilic surface is one on which a droplet of water forms a contact angle less than 90° [34]. Polymer surfaces with the contact angle between 150° and 180° are called superhydrophobic [35]. This phenomenon is also known as the “lotus effect,” which exhibits self-cleaning and anti-contamination features [35-37]. Table 3.3 shows water contact angle values of PAN fibers at different carbonization temperatures.

TABLE 3.3

WATER CONTACT ANGLE VALUES FOR ELECTROSPUN CARBONIZED PAN FIBERS

Specimen No.	Water Contact Angle (°)					
	750°C		850°C		950°C	
	Right	Left	Right	Left	Right	Left
1	149.46	152.36	156.22	156.32	149.21	154.78
2	151.32	154.85	155.23	157.22	152.55	153.22
3	152.63	149.98	155.69	153.45	156.33	154.32
4	153.55	151.11	159.63	155.25	157.54	156.33
5	159.90	148.79	159.58	156.08	158.64	152.52
Mean	152.40		156.47		154.54	
Standard Deviation	± 3.23		± 1.92		± 2.80	

A goniometer (KSV CAM 100) contact angle meter was used to determine the surface wettability of the composite panels. To measure the water contact angle values, a small droplet of DI water was placed on the surface of the composite panels using a small syringe. Figure 3.10

shows the experimental setup for water contact angle values of the PAN-based carbon fiber-reinforced composite panels.

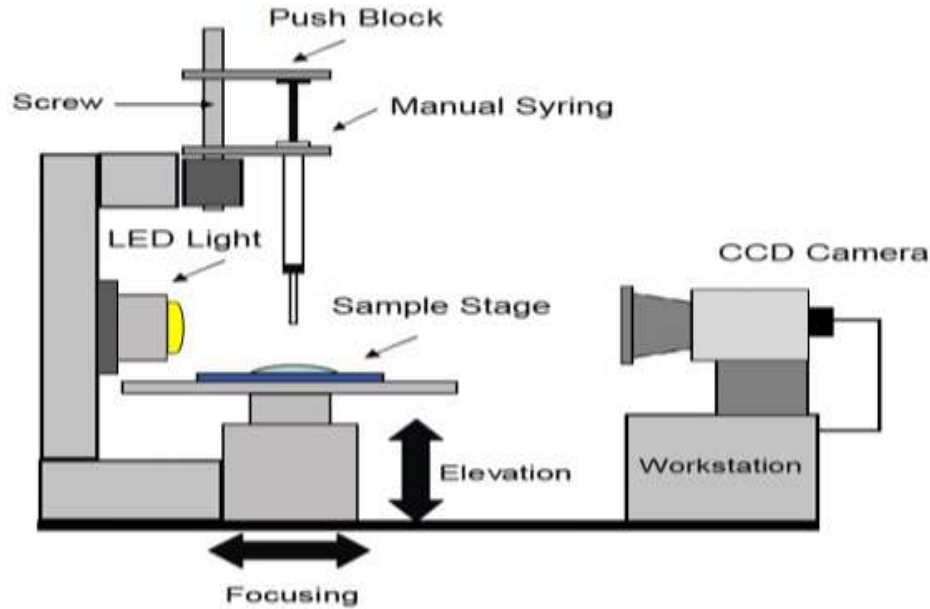


Figure 3.10. Experimental setup for water drop capture [15].

The water contact angle on solid surfaces depends on surface chemistry and surface morphology. PAN fibers are semi-crystalline, with some degree of polarity, due to radicals in the chain structure, which may affect the water contact angle values. Prior to carbonization, the PAN nanofibers provided a water contact angle of about 95° , which may be because of the moisture absorbed, porosity, or the presence of beads left from the electrospinning process. Because of these material defects, PAN has the tendency to absorb water under normal conditions and also absorb some moisture from the atmosphere as well. However, during the carbonization process, the surface chemistry and surface morphology of the PAN fibers are significantly altered. Specifically, the pores and beads in the material are diminished, and the polarity due to the radicals attached to the main chain is eliminated as non-carbonaceous compounds are released.

Figure 3.11 shows an illustration of water contact angle of pre-carbonized PAN fibers.

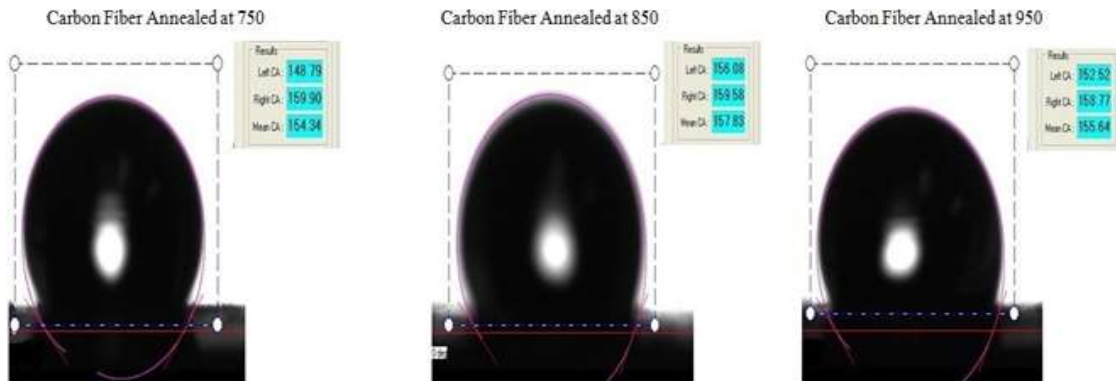


Figure 3.11. Water contact angle of pre-carbonized PAN fibers at different temperatures of 750°C, 850°C, and 950°C.

The carbonized PAN fibers fell into the superhydrophobic material range, with water contact angles between 152° and 156°. The carbonized PAN fibers at 750°C had an average water contact angle of 152.40° (± 3.23), while the fibers carbonized at 850°C provided the highest average water contact angle (156° ± 1.92). Interestingly, the average water contact angle decreased slightly (154° ± 1.54) when the carbonization temperature was increased to 950°C, although it was still within the superhydrophobic range

As shown previously in Table 3.3, carbonized PAN fibers at 850°C had the highest values of water contact angle. This could be attributed to the absence of any residual element in the fibers. The FTIR results for 850°C, shown previously in Figure 3.6, confirms no wiggling in the curve. However, the other two curves for 750°C and 950°C show some wiggling in the FTIR spectra. Likewise, the contact angle values for these two samples (750°C and 950°C) display a declining trend, due to the presence of some residual elements in the fiber texture. PAN can absorb moisture and suspended water vapor from the atmosphere, which may lead to heterogeneity in the samples and cause small variations in contact angle values and some

wriggling in the FTIR spectra. Apart from these minor differences in contact angle values, all the samples are still superhydrophobic. The superhydrophobicity of these PAN fibers is useful in fabricating pre-preg nanocomposites since these fibers can provide better contact and good adhesion with pre-preg carbon fibers. These pre-preg nanocomposites with PAN-derived carbon fibers placed on top of the composite plies having superhydrophobic characteristics can attach to composite structures, thus serving as strain sensors due to their excellent electrical conduction and piezoresistive characteristics.

Excessive loading causes matrix debonding and cracking between nanofibers and pre-preg plies. As can be seen in Figure 3.12, the sample that was carbonized at 850°C shows the highest value of stress, whereas the sample that was carbonized at 950°C shows the lowest value of stress. Table 3.4 provides the mechanical properties of the prepared carbon fiber composites incorporated with PAN-derived carbon fibers.

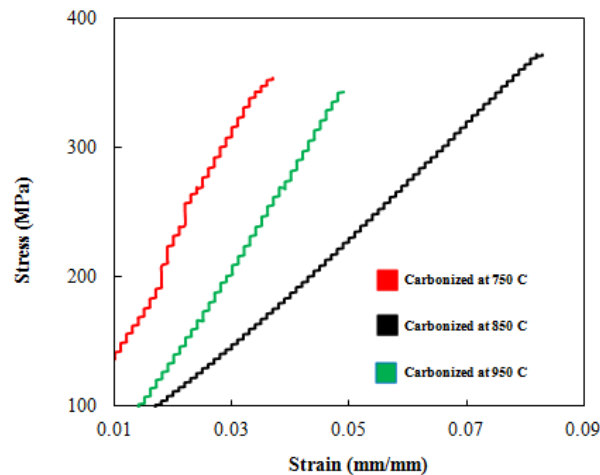


Figure 3.12. Results of tensile tests for carbonized PAN nanocomposite fibers at different temperatures of 750°C, 850°C, and 950°C.

TABLE 3.4

MECHANICAL PROPERTIES OF PAN-DERIVED CARBON FIBER COMPOSITES

Carbonized Temperature of Composite Specimens	Elastic Modulus (MPa)	Peak Load (N)	Ultimate Stress (MPa)	Strain (mm/mm)
750°C	3913.786	24401.950	342.9	0.032
850°C	4546.988	23882.567	350.6	0.085
950°C	4326.986	23871.826	332.8	0.047

3.4.7 Thermal Behavior of Stabilized PAN Fibers

Figure 3.13 shows the differential scanning calorimetry thermogram of bulk PAN, which is shown as an endotherm corresponding to the heat added to the samples in order to maintain the same temperature as the reference pan. The bulk PAN before stabilization showed one cyclization peak at 305°C. The onset temperature was 280°C, and the curves were completed at 325°C. Figure 3.14 shows DSC thermograms of PAN fibers after stabilization.

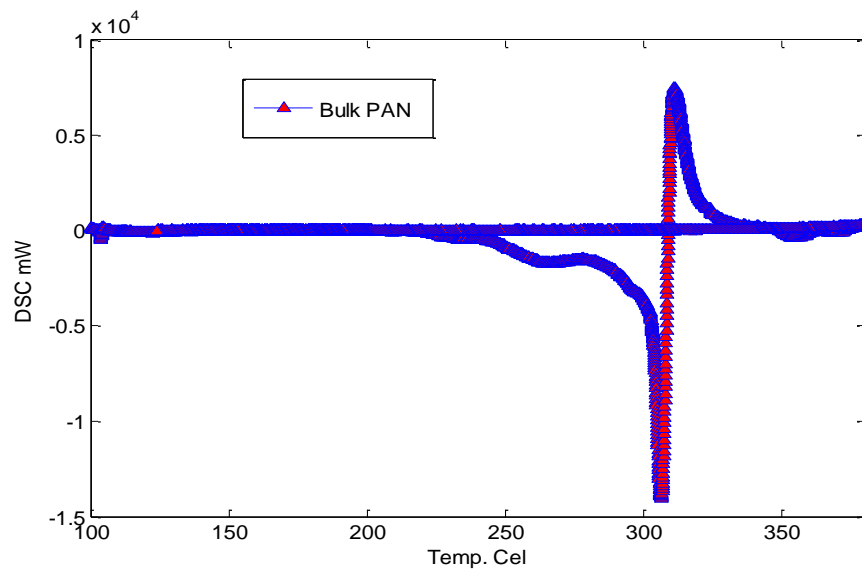


Figure 3.13. DSC thermogram of bulk PAN polymer.

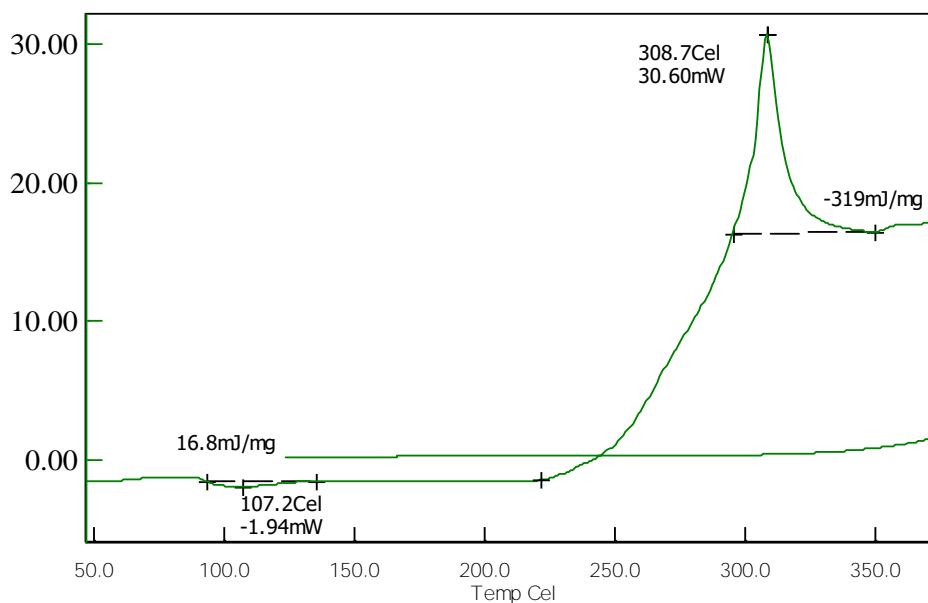


Figure 3.14. DSC thermograms of stabilized PAN fibers.

The DSC thermogram of the stabilized PAN fibers is different than that of the bulk PAN polymer. The bulk sample shows a sharp exothermic peak at 305°C (Figure 3.13), whereas the stabilized fibers show a broad exothermic peak at 308°C (Figure 3.14). Broadening of the exothermic peak could be due to the cyclization process. The cyclization stage of nitrile groups is highly exothermic and leads to fragmentation of the chains due to heat that builds up rapidly in the sample and does not dissipate quickly [25]. It is difficult to eliminate DMF completely in the PAN fibers. The DMF molecules occlude the PAN polymer, and as a result, the DSC thermogram of bulk PAN is different from that of pure PAN fibers. The heat that evolved from the PAN fibers is higher compared to the bulk sample. The characteristic of PAN that dominates its unique properties is the presence of nitrile groups at an intramolecular distance of only a few tenths of a nanometer [25]. It is well-known that the heat capacity difference between PAN fibers and bulk PAN resulted in the heat flow difference in the DSC thermograms. The PAN fibers

were cyclized only by a free radical mechanism, revealing one peak [26]. Additionally, the stabilized PAN fibers revealed a higher cyclization temperature than the bulk PAN polymer, suggesting that more thermal energy is needed for achieving cyclization stage.

3.4.8 Raman Spectra of Stabilized PAN and PAN Fibers

Figure 3.15 shows the representative Raman spectra of carbonized bulk PAN investigated. The peak intensity at 1800 cm^{-1} can be attributed to stabilizing at 280°C , as a result of the tangential vibration of a graphite structure (G-band) and shows additional cross-linking and the formation of a two-dimensional graphitic structure [27]. The Raman spectroscopy peak around 1100 cm^{-1} and 500 cm^{-1} indicates the formation of the γ -phase of the carbonized PAN fibers. The Raman spectroscopy peak at 900 cm^{-1} indicates the formation of the α -phase.

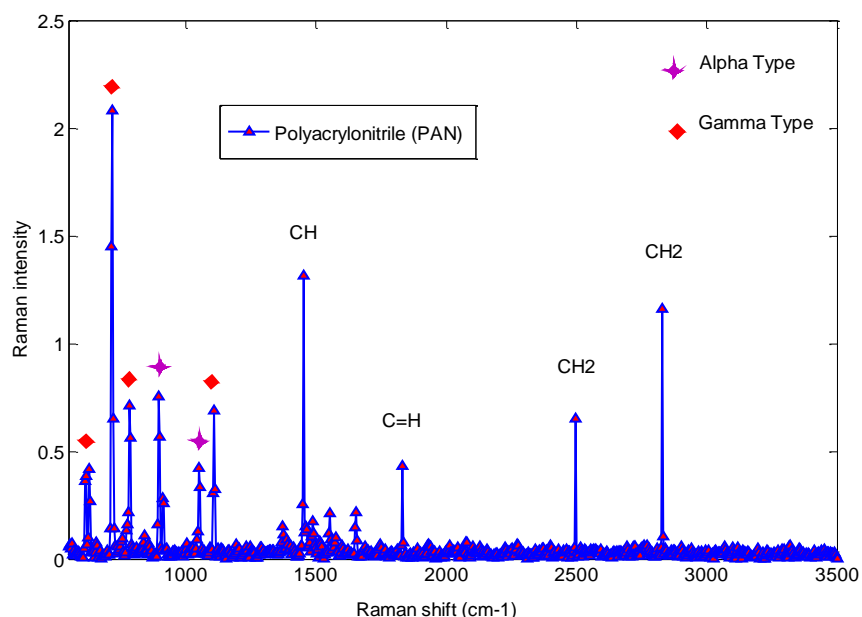


Figure 3.15. Raman spectrum of carbonized bulk PAN polymer.

The highest stretching peak of the CH_2 group was recognized at between $2,500\text{ cm}^{-1}$ and $2,800\text{ cm}^{-1}$ for the carbonized fibers. The group of $\text{C}\equiv\text{N}$ vibration peaks also appeared in the

1,800 cm^{-1} spectrum. As shown in Figure 3.15, a peak at 1,500 cm^{-1} (D-peak) characterizes the disorderly structure of carbon materials [27]. The G- and D-peaks increase as the carbonization temperature increases, indicating that the higher carbonization temperature facilitates the arrangement of carbon from a disorderly to an orderly state [28]. The higher carbonization temperature facilitates the formation of a graphite phase. The D-band is related to the turbostratic structure, and the G-band is related to the other graphite structures. The positions of these two bands are not relevant to the carbonization temperature, and their ratio is known as the “R-value,” which indicates a number of orderly graphite crystallites present in the carbonaceous materials [29]. The ratio of Raman intensities corresponding to the D-band and G-band are generally employed to determine the graphite phase. The lower value ratio of these two intensities shows a high amount of the graphite phase. Raman spectra are helpful in providing information about the crystalline perfection of graphite materials [29].

Figures 3.16, 3.17, and 3.18 show Raman spectra of PAN fibers carbonized at 750°C, 850°C, and 950°C, respectively. The Raman spectra of PAN-derived carbon fibers carbonized at 850°C indicate that the G-band was due to C=C stretching vibrations in the graphite crystallites and that the D-band was attributed to the turbostratic and/or disordered carbonaceous material [29]. The existence of several functional groups with oxygen affects change in the mechanical constant of the C–C bond, resulting in a shift of the D- and G-curves of the sample during the low-temperature carbonization stage [29]. Raman spectra provide useful information on the crystalline perfection of graphite-based materials. All three figures indicate that G- and D-peaks increased as the carbonization temperature increased, indicating that higher carbonization temperature facilitates the arrangement of carbon from a disorderly to an orderly state. They also

show a carbonization line with no peak since all samples are pure carbon or black samples. Therefore, the black samples clearly indicate the steady line behavior with no peaks for carbonized PAN nanofiber composite samples.

Figure 3.19 shows the engineering stress-strain curve behavior of the carbon fiber composites with carbonized electrospun PAN nanofibers. As seen from the 0-strain rate, the composite angle linearly deforms until fracture failure takes place at a strain sensor of 4.5 mm/mm [31]. Carbon fiber composites typically exhibit linear behavior because of their brittle structure, so adding carbonized PAN nanofibers can change their overall behavior [31].

Table 3.5 shows the tensile properties of carbonized electrospun PAN nanofibers on prepreg composites.

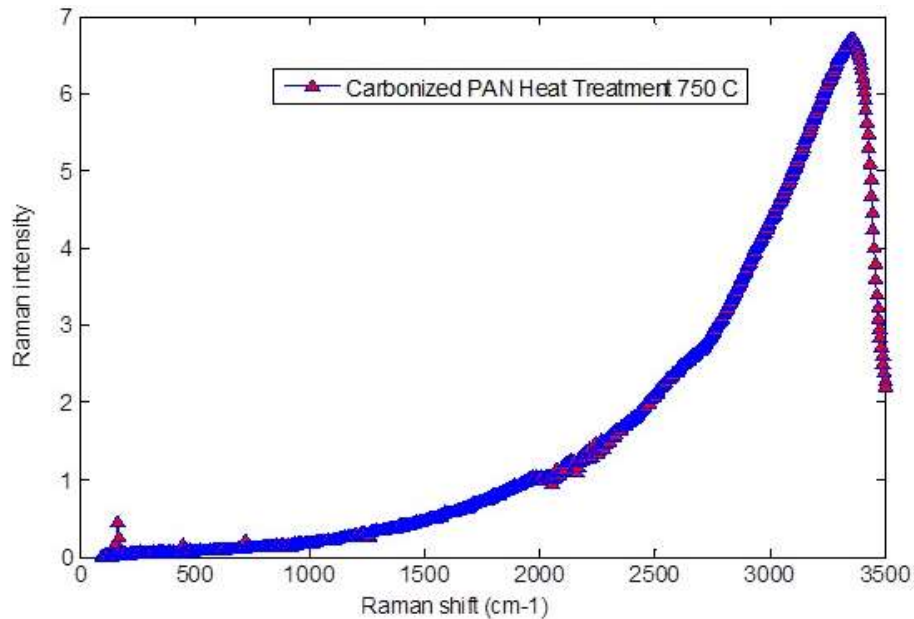


Figure 3.16. Raman spectra of PAN fibers carbonized at 750°C.

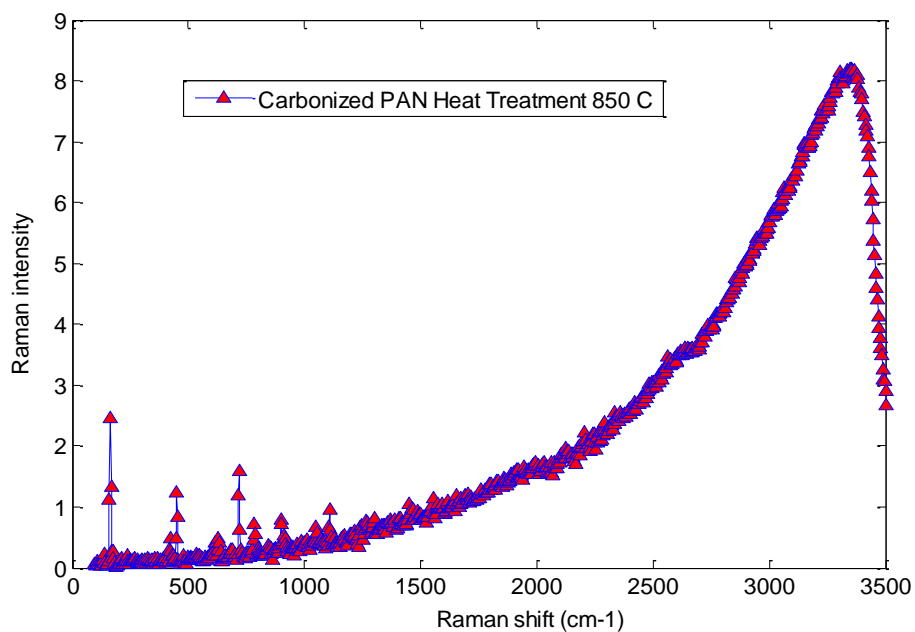


Figure 3.17. Raman spectra of PAN fibers carbonized at 850°C.

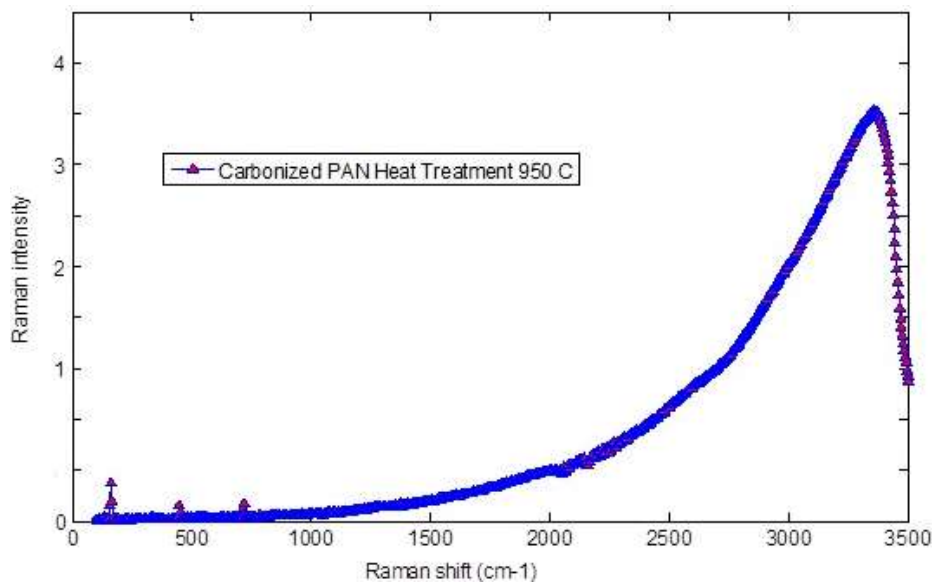


Figure 3.18. Raman spectra of PAN fibers carbonized at 950°C.

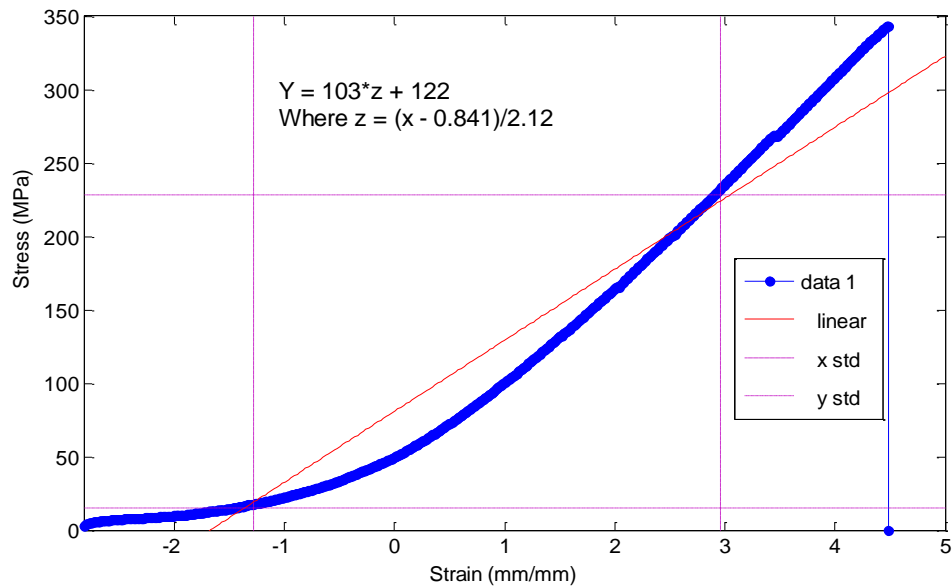


Figure 3.19. Stress vs. strain behavior of carbon fiber composites with carbonized electrospun PAN nanofibers.

TABLE 3.5

PROPERTIES OF CARBONIZED ELECTROSPUN PAN NANOFIBERS
ON PREPREG COMPOSITE

Property	Values
Modules	3913.786 MPa
Peak Load	24401.950 N
Peak Stress	342.9 MPa
Strain at Break	4.5 mm/mm
Width	50.800 mm
Thickness	1.401 mm

A surface is considered to be hydrophobic if it tends not to absorb water or the static contact angle (θ) is greater than 90° . A surface is considered to be hydrophilic if it tends to adsorb water or is wetted by water through making a static contact angle less than 90° [32]. Superhydrophobic surfaces manifest high contact angles ($\theta > 150^\circ$) and low contact hysteresis

[33]. Solid surfaces with a very low water contact angle ($\theta < 5^\circ$ in 0.5 second) are commonly referred to as superhydrophilic. These terms describe the interaction of the boundary layer of a solid phase with a liquid or vapor water. A surface is considered to be wetted if water spreads over the surface evenly without the formation of droplets, and is termed hydrophilic [32]. However, on a hydrophobic surface, water forms distinct droplets that roll off easily without wetting the surface.

In this study, the water contact angles of the carbonized PAN samples were measured, and the results are shown in Figure 3.20. The main goal of measuring the water contact angle of PAN carbonized samples was to determine whether the carbonization at different temperatures made PAN samples hydrophobic or hydrophilic. As can be seen in Figure 3.20, the histogram shows that all PAN carbonized samples are superhydrophobic. The average water contact angle values of the PAN samples carbonized at 750°C, 850°C and 950°C are 155°, 159°, and 160°, respectively. It is well known that PAN is a hydrophobic polymer, and after carbonization, the contact angle varies due to thermal expansion and evolution of volatile compounds.

Both superhydrophobicity and superhydrophilicity of solid surfaces are based on surface chemistry (surface energy) and surface roughness. The wettability of solid surfaces is determined by the surface energy and smoothness of the surface. The surface microstructure and surface chemistry determine whether droplets of water will roll off or spread evenly on the surface. As can be seen in Figure 3.20 the surface morphology completely changed after carbonization. The surface appeared as bumpy or pitted after carbonization due to the evolution of volatile compounds and water vapor during the heat treatment, thereby making the surface rougher. The presence of DMF in PAN fibers that evaporated during heat treatment left behind a possible

rough and porous microstructure. The diameter of fibers was reduced during carbonization; thus, the surface area is increased, thereby reducing the surface free energy.

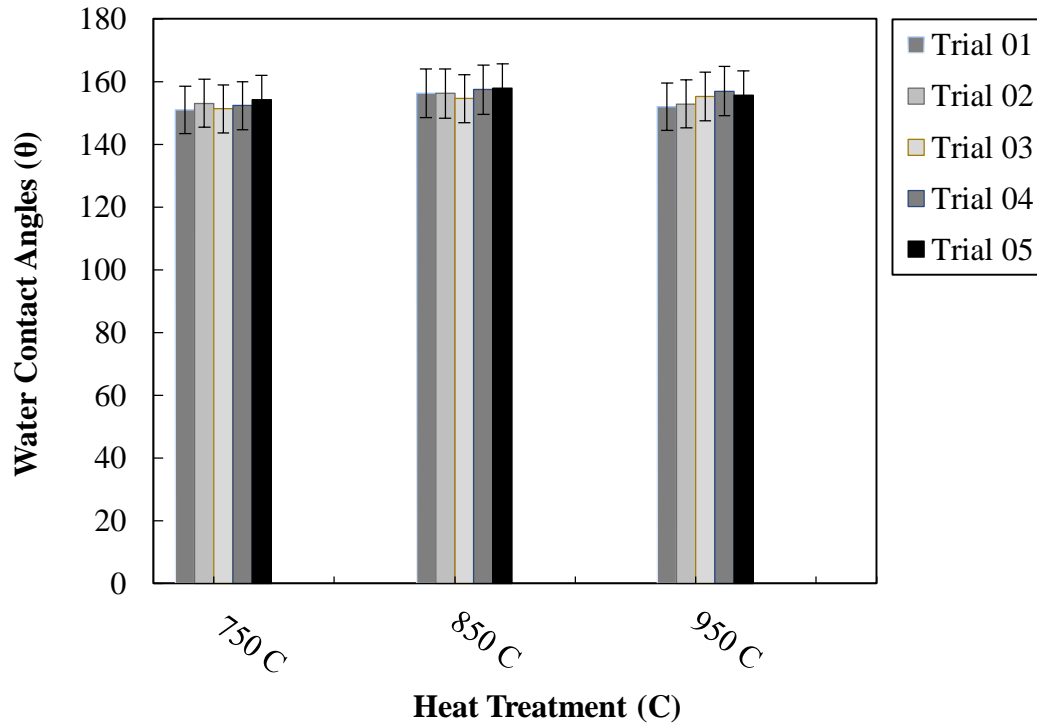


Figure 3.20. Contact angle measurements of PAN samples after carbonization at 750°C, 850°C, and 950°C.

3.5 Conclusions

PAN is one of the most extensively studied polymers that has a wide range of industrial applications (e.g., aircraft, wind turbines, automobiles, etc.). In this study, PAN-based electrospun fibers were oxidized at 270°C and subsequently carbonized at 750°C, 850°C, and 950°C for 1 hr to fabricate highly purified carbon nanofibers mats. This study deals with the property analysis of the carbonized electrospun PAN fibers for possible structural health monitoring system development. Several characterization techniques—XRD, TGA, DSC, FTIR, and water contact angle measurements—were conducted on the PAN fibers before and after the

carbonization processes in order to investigate the chemical, electrical, structural, and surface properties of the PAN-based fibers. Test results indicate that after the carbonization of the PAN nanofibers, physical properties of the nanofibers such as the carbon weight%, hydrophobicity, and ionic conductivity were drastically improved, which may be useful for the various industries that employ SHM systems. These PAN-derived fibers were characterized using DSC and Raman spectroscopy to determine their thermal and chemical properties. Raman spectroscopy peaks around 1100 cm^{-1} and 500 cm^{-1} indicated the formation of the γ -phase of the carbonized PAN fibers. Likewise, a Raman spectroscopy peak at 900 cm^{-1} indicated the formation of the α -phase.

The G- and D-peaks increased as the carbonization temperature increased, indicating that the higher carbonization temperature facilitates the arrangement of carbon from an amorphous to crystalline state. DSC studies showed that PAN fibers are cyclized only by a free radical mechanism, revealing one peak. Moreover, the stabilized PAN fibers revealed a higher cyclization temperature than the bulk PAN polymer, thus suggesting that more thermal energy is needed for the cyclization stage. These studies also showed that PAN-derived carbon fibers are rich in carbon content and have excellent thermal stability, so these fibers could be useful for structural health monitoring as well as lightning strike and electromagnetic interference shielding applications. Shear stress tests were applied to composite panels to characterize the mechanical properties of these novel nanomaterials. Water contact angle measurements revealed that all samples were superhydrophobic. These nanomaterials and methods could widely open up many possibilities to developing highly sensitive SHM devices and sensors for composite aircraft and wind turbines, as well as other infrastructures.

3.6 References for Chapter 3

- [1] Farrar, C. R., and Worden, K., “An Introduction to Structural Health Monitoring,” *Philosophical Transactions of the Royal Society A*, Vol. 365, 2007, pp. 303-315.
- [2] Cawley, P., “Long Range Inspection of Structures Using Low Frequency Ultrasound,” in *Proceedings of DAMAS*, 1997, Sheffield, UK: Sheffield Academic Press, pp. 1-17.
- [3] Bartelds, G., “Aircraft Structural Health Monitoring, Prospects for Smart Solutions from a European Viewpoint,” *Journal of Intelligent Material Systems and Structures*, Vol. 9, No. 11, 1998, pp. 906-910.
- [4] Staszewski, W. J., Biemans, C., Boller, C., and Tomlinson, G. R., “Impact Damage Detection in Composite Structures—Recent Advances,” in *Structural Health Monitoring 2000*, Ed. Fu-Kuo Chang, Proceedings of the 2nd Internatioal Workshop on Structural Health Monitoring, Stanford University, Palo Alto, CA, September 8-10, 1999, pp. 754-763.
- [5] Spencer, B. F., Ruiz-Sandoval, M., and Kurata, N., “Smart Sensing Technology for Structural Health Monitoring,” *13th World Conference on Earthquake Engineering Vancouver*, BC, Canada, August 1-6, 2004, Paper No. 1791.A.
- [6] Ilison, M. B, Dimitry, P., Shuyou, L., Yuris, D., and Horacio, D. E., “In Situ Transmission Electron Microscope, Tensile Testing Reveals Structure–Property Relationships in Carbon Nanofibers,” *Carbon*, Vol. 60, 2013, pp. 246-253.
- [7] Nataraj, S. K., Yang, K. S., and Aminabhavi, T. M., “Polyacrylonitrile-Based Nanofibers: A State of the Art Review,” *Progress in Polymer Science*, Vol. 37, No. 3, 2012, pp. 487-513.
- [8] Chand, S., “Carbon Fibers for Composites,” *Journal of Materials Science*, Vol. 35, No. 6, 2000, pp. 1303-1313.
- [9] Yun, K. M., Hogan, C. J., Matsubayashi, Y., Kawabe, M., Iskandar, F., and Okuyamam, K., “Nanoparticle Filtration by Electrospinning Polymer Fibers,” *Chemical Engineering Science*, Vol. 62, No. 17, 2007, pp. 4751-4759.
- [10] Yalcinkaya, B., Yener, F., Jirsak, O., and Cengiz-Callioglu, F., “On the Nature of Electric Current in the Electrospun Fibers,” *Journal of Nanomaterials*, Vol. 2013, 2013, 10 pages.
- [11] Tse-Hao, K., Tzy-Chin, D., Jeng-An, P., and Ming-Fong, L., “The Characterization of PAN-Based Carbon Fibers Developed by Two-Stage Continuous Carbonization,” *Carbon*, Vol. 31, No. 5, 1993, pp. 765-771.

- [12] Cho, C. W., Cho, D.C., Ko, Y-G., Kwon, O. H., and Kang, I. K., “Stabilization, Carbonization, and Characterization of PAN Precursor Webs Processed by Electrospinning Technique,” *Carbon Letters*, Vol. 8, No. 4, 2007, pp. 313-320.
- [13] Su, C.-I., Haung, Y. X., Wong, J. W., Lu, C.-H., and Wang, C.-M., “PAN-Based Carbon Nanofiber Absorbents Prepared Using Electrospinning,” *Fibers and Polymers*, Vol. 13, No. 4, 2012, pp. 436-442.
- [14] Ndi Nsami, J., and Ketcha Mbadcam, J., “The Adsorption Efficiency of Chemically Prepared Activated Carbon from Cola Nut Shells on Methylene Blue,” *Journal of Chemistry*, Vol. 2013, 2013, pp.1- 7.
- [15] Abich, S. E., Gimba, C. E., Uzairu, A., and Dallatu, Y. A., “Preparation and Characterization of Activated Carbon from Palm Kernel Shell by Chemical Activation,” *Research Journal of Chemical Sciences*, Vol. 3, No. 7, 2013, pp. 54-61.
- [16] Rodrigues, L. A., de Sousa Ribeiro, L. A., Thim, G. P., Ferreira, R. R., Alvarez-Mendez, M. O., and dos Reis Coutinho, A., “Activated Carbon Derived from Macadamia Nut Shells: An Effective Adsorbent for Phenol Removal,” *Journal of Porous Materials*, Vol. 20, 2013, pp. 9635-9645.
- [17] Iwashita, N., Park, C., Fujimoto, H., Shiraishi, M., and Inagaki, M., “Specification for a Standard Procedure of X-Ray Diffraction Measurements on Carbon Materials,” *Carbon*, Vol. 42, 2004, pp. 701–714.
- [18] Ma, X., Yuan, C., and Liu, X., “Mechanical, Microstructure and Surface Characterizations of Carbon Fibers Prepared from Cellulose after Liquefying and Curing,” *Materials*, Vol. 7, 2014, pp. 75-84.
- [19] Eslami, F. R., Raissi, S., Shokuhfar, A., and Sedghi, A., “FT-IR Study of Stabilized PAN Fibers for Fabrication of Carbon Fibers,” *World Academy of Science, Engineering and Technology*, Vol. 50, 2009, pp. 430-433.
- [20] Saufi, S. M., and Ismail, A. F., “Development and Characterization of Polyacrylonitrile (PAN)-Based Carbon Hollow Fiber Membrane,” *Songklanakarin Journal of Science and Technology*, Vol. 24, 2002, pp. 843-854.
- [21] Memon, S. A., Liao, W., Yang, S., Cui, H., and Shah, S. F. A., “Development of Composite PCMs by Incorporation of Paraffin into Various Building Materials,” *Materials*, Vol. 8, No. 2, 2015, pp. 499-518.

- [22] Goracheva, V. O., Mikhailova, T. K., Fedorkina, S. G., Konnova, N. F., Azarova, M. T., and Konkin, A. A., “Thermographic and Thermogravimetric Analysis of the Thermal Behavior of Polyacrylonitrile Fibers,” *Fiber Chemistry*, Vol. 5, No. 5, 1973, pp. 496-498.
- [23] Shijie, X., Honghong, L., Yuanjian, T., Lianghua, X., and Biaohua, C., “Thermal Behavior and Kinetics during the Stabilization of Polyacrylonitrile Precursor in Inert Gas,” *Applied Polymer Science*, Vol. 122, 2011, pp. 480–488.
- [24] Boulet, P., Brissinger, D., Collin, A., and Parent, G., “On the Influence of the Sample Absorptivity when Studying the Thermal Degradation of Materials,” *Materials*, Vol. 8, No. 8, 2015, pp. 5398-5413.
- [25] Ouyang, Q., Cheng, L., Wang, H., and Kaixi, L., “Mechanism and Kinetics of the Stabilization Reactions of Itaconic Acid-modified Polyacrylonitrile,” *Polymer Degradation and Stability*, Vol. 93, No. 8, 2008, pp. 1415-1421.
- [26] Aviles, M. A., Gines, J. M., Del Rio, J. C., Pascual, J. L., and Perez-Rodriguez, P. J., “Thermal Analysis of Acrylonitrile Polymerization and Cyclization in the Presence of N,N-dimethylformamide,” *Thermal Analysis and Calorimetry*, Vol. 67, No. 1, 2002, pp. 177-188.
- [27] Alarifi, I. M., Alharbi, A., Khan, W. S., Swindle, A., and Asmatulu, R., “Thermal, Electrical and Surface Hydrophobic Properties of Electrospun Polyacrylonitrile Nanofibers for Structural Health Monitoring,” *Materials*, Vol. 8, No. 10, 2015, 7017-7031.
- [28] Slade, P. E., and Jenkins, T. L., *Thermal Characterization Techniques*, Marcel Dekker, New York, 1970.
- [29] Ramakrishna, S., Fujihara, K., and Ma, Z., *An Introduction to Electrospinning and Nanofibers*, World Scientific, Singapore, 2005.
- [30] Wendorff, J. H., Agarwal, S., and Greiner, A., *Electrospinning: Materials, Processing, and Applications*, John Wiley & Sons, 2012.
- [31] Lee, J. K., An, K. W., Ju, J. B., Cho, B. W., Cho, W. I., Park, D., and Yun, K. S., “Electrochemical Properties of PAN-Based Carbon Fibers as Anodes for Rechargeable Lithium Ion Batteries,” *Carbon*, Vol. 39, 2001, pp. 1299–1305.
- [32] Ra, E. J., An, K. H., Kim, K. K., Jeong, S., and Lee, Y. H., “Anisotropic Electrical Conductivity of MWCNT/PAN Nanofiber Paper,” *Chemical Physics Letters*, Vol. 413, 2005, pp. 188–193.

- [33] Khan, W. S., El-Tabey, M. M., and Asmatulu, R., “Electrical and Thermal Characterization of Electrospun PVP Nanocomposite Fibers,” *Journal of Nanomaterials*, Vol. 2013, 2013, pp. 9.
- [34] Groszek, A. J., and Partyka, S., “Measurements of Hydrophobic and Hydrophilic Surfaces Site by Flow Microcalorimetry,” *Langmuir*, Vol. 9, 1993, pp. 2721–2725.
- [35] Nuraje, N., Khan, W. S., Lei, Y., Ceylan, M., and Asmatulu, R., “Superhydrophobic Electrospun Nanofibers,” *Journal of Materials Chemistry A*, Vol. 1, No. 6, 2013, pp. 1929-1946.
- [36] Jing, D., Zhaohui, Y., Tianzhong, Y., Lili J., and Chengmin, S., “Control of Superhydrophilic and Superhydrophobic Graphene Interface,” *Scientific Report*, Vol. 3, 2013, pp. 1733-1739.
- [37] Mohammed, A. A., Moussa, W. A., and Lou, E., “High Sensitivity MEMS Strain Sensor: Design and Simulation,” *Sensors*, Vol. 8, 2008, pp. 2642-266.
- [38] Nagy, M., Apanius, C., and Siekkinen, J., “A User Friendly, High-Sensitivity Strain Gauge,” *Sensors*, Vol. 18, 2001, pp. 20-27.
- [39] Hrovat, M., Belavic, D., Samardzija, Z., and Holc, J., “An Investigation of Thick-Film Resistor, Fired at Different Temperatures, for Strain Sensors,” *24th International Spring Seminar on Electronics Technology: Concurrent Engineering in Electronic Packaging*, 2001, pp. 32-36.
- [40] Wen, S., and Chung, D. D. L., “Carbon Fiber-Reinforced Cement as a Strain-Sensing Coating,” *Cement and Concrete Research*, Vol. 31, 2001, pp. 665-667.
- [41] Wang, X., Fu, X., and Chung, D. D. L., “Strain Sensing Using Carbon Fiber,” *Journal of Materials Research*, Vol. 14, No. 3, 1999, pp. 790-802.
- [42] Mäder, T., Nestler, D., and Wielage, B., “Strain Sensing Using Single Carbon Fibers,” *18th International Conference on Composite Materials*, August 2011, pp. 21-26.

CHAPTER 4

MECHANICAL AND THERMAL PROPERTIES OF CARBONIZED PAN NANOFIBERS COHESIVELY ATTACHED TO SURFACE OF PREPREG CARBON COMPOSITE

4.0 Abstract

Prepreg composite materials are becoming increasingly common in the composite industry due to their ease of fabrication, consistent properties, and good surface finish. The term “prepreg” is actually an abbreviation for the word “pre-impregnated.” Generally, the resin used in prepreg composite materials is an epoxy resin. However, other types of resins can be used, including the majority of thermoset and thermoplastic resins. The resin system used in this study is an epoxy that includes the proper curing agent. As a result, it is ready to lay into a mold without the addition of resin or the steps required of a typical hand lay-up. It has the advantage of having nearly perfect epoxy resin content, thus maximizing strength. In this study, unidirectional prepreg carbon fibers of ten plies were laid up in a 0-, 45-, -45-, and 45-degree stacking sequence on a flat and smooth aluminum plate, and then carbonized electrospun polyacrylonitrile nanofibers were placed on top of the last ply prior to curing in a vacuum oven. The PAN electrospun fibers were oxidized at 280°C in an ambient condition for 1 hr and then carbonized at 850°C for 1 hr in an argon gas atmosphere. The resultant composite panels were cut into small pieces and subjected to a number of different characterization techniques.

Thermomechanical analysis (TMA) measurements clearly showed that significant reinforcement was achieved for the prepreg/carbonized PAN fiber composites because of the enhanced interfacial bonding between the PAN nanofibers and the matrix. Dynamic mechanical analysis (DMA) tests exhibited a shift in the glass transition temperature of the carbonized PAN

nanofiber/composite, which may be helpful in high-temperature applications using these composites. A Raman spectroscopy peak around 897 cm^{-1} indicated the formation of the γ -phase of the carbonized PAN fibers. The highest stretching peak of the CH_2 group was recognized within the range of $2,500\text{--}2,800\text{ cm}^{-1}$ for the carbonized fibers. The vibration peak of the $\text{C}\equiv\text{N}$ group also appeared in the spectrum at $1,452\text{ cm}^{-1}$. TMA determined the coefficient of thermal expansion (CTE), indicating an improvement in stability of the composite material, which can be useful for structural health monitoring as well as lightning strikes and electromagnetic interference shielding applications of new carbon fiber composites.

4.1 Introduction

Carbon fibers have been receiving significant attention due to their excellent properties, such as high mechanical strength and moduli, high thermal and electrical conductivity, good corrosion resistance, high fatigue strength, high creep resistance, and superior stiffness. As such they are finding widespread applications in heat-treatment materials, high-temperature catalysts, sensors, composite reinforcement materials, woven composites, structural laminates, membrane-based separation, nanoelectronics, and photonics [1, 2]. Carbon nanofibers are multi-functional and one-dimensional nanomaterials, which are being used in advanced polymer matrix composites due to their outstanding properties and low density [3]. They behave elastically until failure, possess a low CTE, and are chemically inert until they are exposed to oxidizing environments [3, 4]. Many precursors are used for the large-scale production of carbon fibers, such as polyacrylonitrile, pitch, and cellulose [3, 6, and 7]. However, PAN is largely used as the precursor for the large-scale production of carbon fibers, owing to its good tensile and compressive properties, and high carbon yield [3, 8]. Generally, PAN-derived carbon fibers are

produced as follows: (1) first, the precursor is spun to fabricate PAN fibers; (2) then, the PAN fibers are stabilized in an atmosphere of 270–300°C; and (3) finally, the stabilized PAN fibers are carbonized in an inert atmosphere at high temperature (900°C) to eliminate all non-carbon elements and obtain high-purity carbon [3]. PAN-derived carbon fibers are one of the important carbon fibers, and have been under extensive investigation from a research point of view and from a practical applications point of view. These fibers are finding applications in electrical devices, electrode materials in batteries, and supercapacitors, as well as sensors.

Prepregs are a kind of specially formulated resin system that can be reinforced with carbon fibers, Kevlar fibers, and glass fibers. These composites have fiber-reinforced resins that can be cured under pressure and temperature in order to be transformed into solid structure materials that are exceptionally strong, lightweight, temperature-resistant, and durable. In this study, uncured prepreg carbon fiber composite peel plies, provided from a local store, and a ply of PAN-derived carbon fibers placed on top of the assembly, were used to fabricate pre-preg carbon fiber composites. Conventional carbon fibers developed from a PAN precursor have a tensile strength as high as 7 GPa and diameters of 5–10 microns [3]. Carbon fibers derived from electrospun PAN have diameters in the range of 100–300 nm, are approximately 1,000 times smaller in cross section than conventional fibers, and can provide high material refinement and tremendous interaction with matrix materials, thus increasing the shear strength of composites [3]. Electrospun PAN nanofibers are converted into carbon fibers by stabilizing and carbonizing, and the high-temperature heat treatment of PAN fibers results in high strength due to the higher carbon content [3].

The electrospinning technique was used to fabricate PAN nanofibers. Electrospinning is a straightforward, simple, and cost-effective method of producing fibers from a polymeric solution or melts having a diameter in the range of microns to nanometers [3, 9, 10, 11, 12]. Electrospun nanofibers possess a high orientation of polymer chains due to applied electrostatic forces, which cause large plastic deformation [3]. This process is accompanied by a large evaporation of the solvent, resulting in electrospun fibers with high packaging density [3]. During plastic stretching, fibers experience thinning at a strain rate of $\sim 1000 \text{ s}^{-1}$ and a drawing ratio as high as 10^4 [13]. Recently, it has been observed that the molecular orientation and degree of crystallinity of electrospun fibers is high [13]. Some factors are critical in the fabrication of PAN-derived carbon fibers using the electrospinning process. One is control of the molecular orientation and crystallinity of the fibers, and the other is the thermal treatment of PAN fibers including pre-oxidation, stabilizing, and carbonization [3]. These processes convert PAN precursor nanofibers into carbon nanofibers that are very long, contain a high content of carbon, and possess the desired microstructure, electrical, mechanical, and thermal properties [3].

4.2 Experimental Materials and Methods

4.2.1 Materials

Dimethylformamide (CAS no. 68-12-2, 99.8%) and polyacrylonitrile (CAS no. 25014-41-9, 0.2%, molecular weight 150,000 g/mole) were purchased from Sigma-Aldrich and used without any alteration. Uncured pre-preg carbon fibers composite peel plies were provided from a local store to fabricate pre-preg carbon fiber composites in a vacuum oven [14].

4.2.2 Fabrication of PAN Nanofibers

PAN was dissolved in the polar DMF solvent at a 10:90 weight ratio, and then the mixture was mechanical stirred on a hot plate at 500 rpm for 1 hr at a temperature of 70°C. The PAN polymeric solution was allowed to cool to room temperature before electrospinning and then transferred to a 10-ml plastic syringe having an inside diameter of 0.5 mm. A copper electrode with a 0.25-mm diameter was attached to the syringe at one end, while the other end of the electrode was attached to a high DC power supply. The electrospinning process was carried out with a voltage of 25 kV DC, feed rate of 1 ml/hr, and spinneret-to-collector distance of 25 cm. All experiments were performed at room temperature under ambient conditions.

Figure 4.1 shows SEM images of PAN fibers. Figure 4.1(a) shows PAN fibers before carbonization as well as a uniform cross section of a PAN fiber with an average diameter of $1,000 \pm 50$ nm. The average fiber diameter shrinks after carbonization. Figure 4.1(b) shows a magnified view of the PAN fibers after carbonization. As can be seen, after carbonization, the fiber mat retains its shape, but the average diameter becomes approximately 500 ± 50 nm.

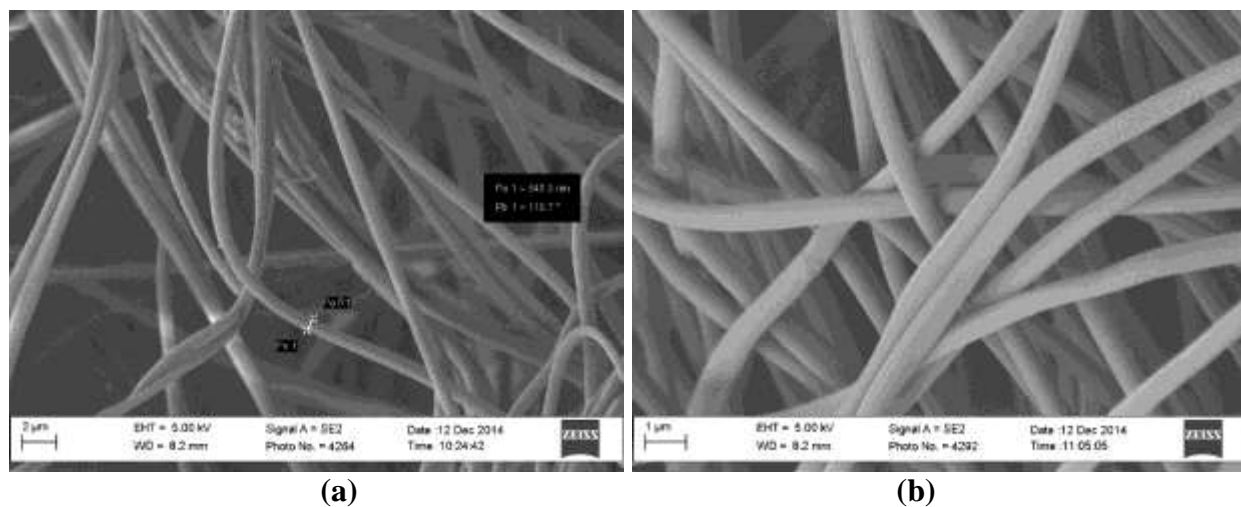


Figure 4.1. SEM images of PAN fibers: (a) before carbonization; (b) after carbonization.

4.2.3 Carbonization of PAN Nanofibers

The PAN nanofibers thus generated through electrospinning were converted into high-purity carbon nanofibers, first by stabilizing them in an oxygen atmosphere at 280°C for 1 hr and then subsequently carbonizing them at 850°C in an inert atmosphere (argon) for 1 hr more. The carbon nanofibers thus produced contain around 92% carbon, but in order to produce 99% carbon fibers, which are actually graphite nanofibers, additional heating at 3,000°C is needed. However, 92% pure carbon is good enough for the present study. The heating ramp rate was 5°C/min. An acidic solution was prepared by mixing 3.5 g of HCl into 100 ml of DI water for the acid treatment (carbon activation) of the carbonized fibers. The fiber samples were mixed with the solution for about 2 hr and dried in a conventional oven at 120°C overnight. The dried samples were further dried at 400°C in a furnace with an N₂ atmosphere for nearly 2 hr. Then the samples were washed with DI water several times until reaching pH 7 and dried at 100°C overnight in a vacuum.

During the stabilizing process, PAN fibers absorb oxygen from the atmosphere and undergo some chemical changes that result in cyclization of the PAN macromolecules. This leads to the formation of a ladder-like structure, which is difficult to melt, thus retaining fiber morphology in the subsequent carbonization process [22]. During stabilization, PAN experiences cyclization and partly dehydrogenation, which make these fibers denser and able to retain their fibrous structure during carbonization at elevated temperatures [3]. In the carbonization process, gasses such as N₂, HCN, and H₂O evolve, and the carbon yield is increased to around 90%; therefore, this process leads to a significant reduction in fiber diameter and the formation of three-dimensional carbonaceous structures [22].

4.2.4 Nanocomposite Fabrication

Pre-preg carbon fibers of ten plies were laid up in a 0-, 45-, -45-, and 45-degree stacking sequence on a flat and smooth aluminum mold, and then a carbonized electrospun PAN nanofiber mat was placed on top of the last ply prior to vacuum curing in a vacuum oven [15]. Figure 4.2 shows the fabrication of a highly conductive PAN-derived carbon fiber composite used in this study.

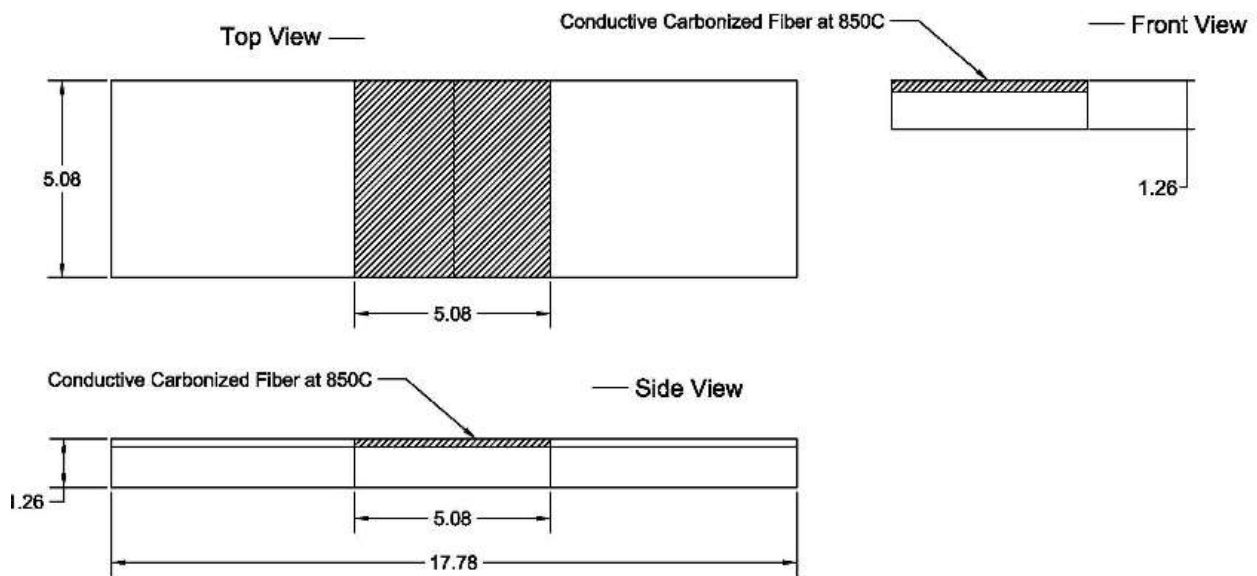


Figure 4.2. Fabrication of PAN-derived carbonized nanofibers composite.

A release agent was sprayed several times on the mold before placing the piles on the mold. Then a release film, cold sheet, berating film, and vacuum bag film were applied before sealing with a tacky tape. After the de-bulking process under a vacuum at 27 Hg, the prepreg and carbon nanofiber was cured in a four-step heating process: (1) 30 min at 75°C; (2) 1 hr at 140°C; (3) 2 hr at 185°C; and (4) 30 min at 50°C [15]. As a result, the carbonized carbon fiber mat was cohesively bonded on the surface of the fiber composite without any damage.

4.3 Results and Discussion

4.3.1 Tensile Tests of PAN-Derived Carbon Nanofibers Composite

The prepared PAN-derived carbon fibers composite panels were tested under tensile loadings. These tests were performed in the axial direction of the applied load, and Young's modulus and yield strength were determined. A four-circumferential ring probe was employed to measure resistance in the nanocomposite sample. A constant current was applied along the axial direction through outer probes, and the corresponding voltage drop between inner probes was measured for various strains along the axial direction. Data was continuously acquired using a LabVIEW software program. The sample was subjected to ramping loads, both tensile and compressive, and loaded at a constant rate of 1 mm/min. The displacement due to loading was used to calculate strain under the quasi-static loading. Figure 4.3 shows the engineering stress-strain curve for a PAN-derived carbon fiber composite.

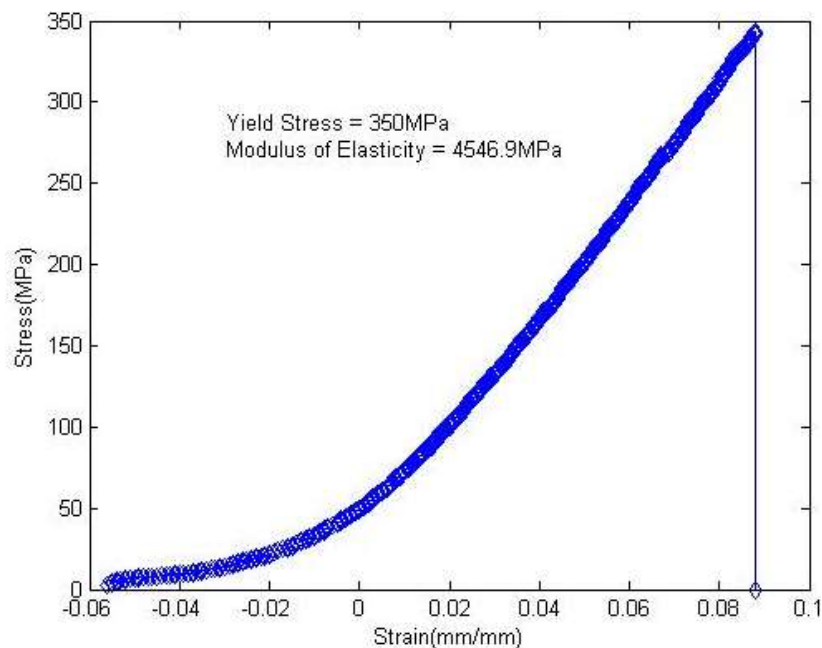


Figure 4.3. Engineering stress-strain curve for PAN-derived carbonized nanofiber composite.

As can be seen in Figure 4.3, the percentage of elongation at breaking is around 0.084, which corresponds to a stress value of 350 MPa. The composite specimen deforms linearly until a fracture occurs. Some microcombustion analysis reveals that the carbonized fibers contain nearly 89.47% carbon, 3.93% nitrogen, and 3.03% oxygen [13]. The small percentage of nitrogen is due to the presence of the C-N bond, which is found in PAN carbon fibers when they are subjected to heat treatment at an elevated temperature [13, 16, 17]. Beese et al. [18] and Arshad et al. [19] reported that the modulus of elasticity increases with the decrease in fiber diameter. Many researchers have studied the dependence of fiber strength on its diameter using various fibers, and it has been determined that decreasing the number of fibers results in a lower fiber volume and a reduced number of defects and cracks, thereby resulting in a lower probability of failure [20, 21].

Additionally, when nanofibers are spun at the longest distances between the capillary tube and the collector, they possess the highest modulus and tensile strength, due to the fact that they have better molecular orientation, which is significant in improving the properties of carbon fibers [3]. The strain rate during electrospinning increases to as high as $1,000\text{S}^{-1}$, which, according to many studies, increases the molecular orientation of the resulting nanofibers [3]. Short electrospinning distances limit the number and order of molecular-stretching/bending instabilities during electrospinning, while long electrospinning distances allow multiple bending instabilities and ensure complete evaporation of the solvent, which promotes better molecular orientation [3]. Some studies have shown that PAN nanofibers fabricated at 25 kV and a 25-cm distance between the target and the collector have the highest tensile strength and modulus, but the strain failure could be $\sim 200\%$ for all electrospinning conditions [3, 19]. The high modulus of

PAN-derived carbon fiber composites is due to the stabilization at high temperature, which results in a high capacity fraction of a purely ordered phase caused by additional cross-linking reactions [23].

4.3.2 Raman Spectrum of PAN-Derived Carbon Fiber Composite

Figure 4.4 shows a typical Raman spectrum of carbonized PAN fibers. The intensity of the peak at 1700 cm^{-1} can be attributed to stabilizing at 280°C . This peak comes from the tangential vibration of a graphite structure (G-band) and shows additional cross-linking and the formation of a two-dimensional graphitic structure [23].

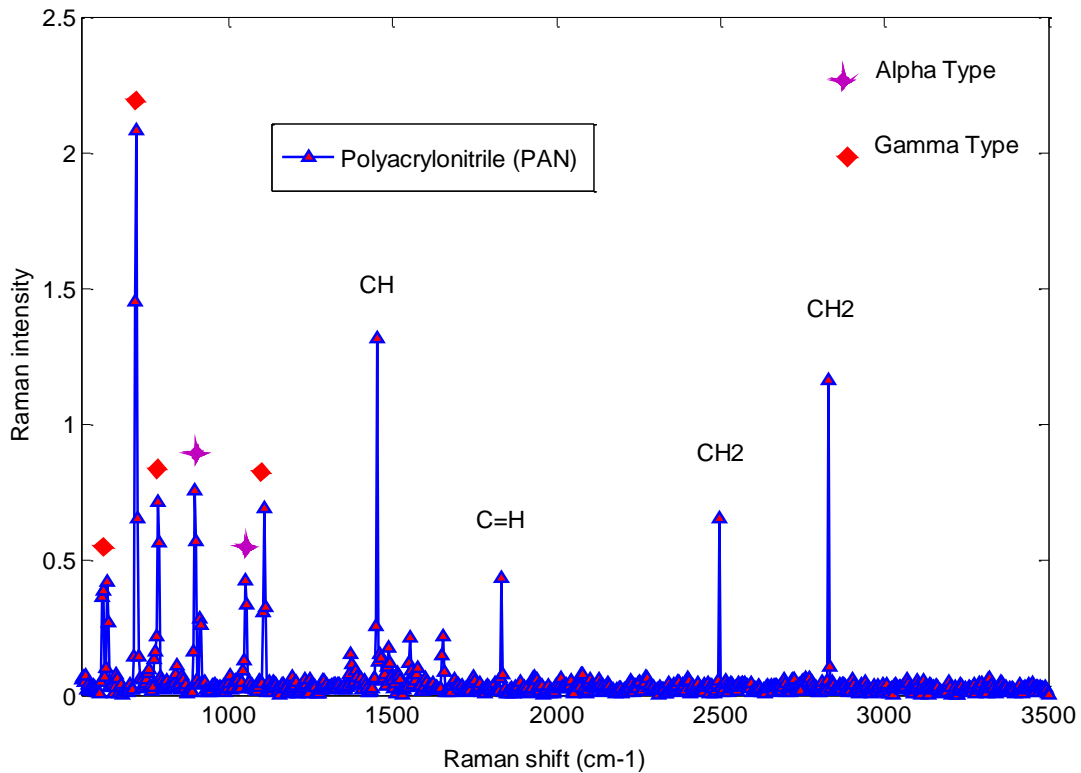


Figure 4.4. Raman spectrum of carbonized PAN nanofibers.

A Raman spectroscopy peak at around 897 cm^{-1} indicates the formation of the γ -phase of the carbonized PAN fibers. The highest stretching peak of the CH_2 group was recognized within

the range of 185–200 cm^{-1} for the carbonized fibers. The group of $\text{C}\equiv\text{N}$ vibration peak also appeared in the spectrum at 1,452 cm^{-1} . As shown in Figure 4.4, a peak at 1,350 cm^{-1} (D-peak) characterizes the disorderly structure of carbon materials [23]. The G- and D-peaks increased as the carbonization temperature increases, indicating that the higher carbonization temperature facilitates the arrangement of carbon from a disorderly to an orderly state [37]. The D-band is related to the turbostratic structure; the G-band is related to the order graphite structures. The positions of these two bands are not relevant to the carbonization temperature, and their ratio is known as the “R-value,” which indicates the amount of orderly graphite crystallites present in the carbonaceous materials [22]. The ratio of Raman intensities corresponding to the D-band and the G-band are used as identification for determining the graphite phase. The lower value of the ratio of these two intensities indicates low defects, a low amount of the amorphous phase, and a high amount of the graphite phase. Raman spectra are helpful in providing information about the crystalline perfection of graphite materials [22]. Raman spectra of PAN-derived carbon fibers carbonized at 850°C indicate that the G-band was due to $\text{C}=\text{C}$ stretching vibrations in the graphite crystallites, and the D-band was attributed to the turbostratic and/or disordered carbonaceous material [22].

4.3.3 Thermogravimetric Analysis of PAN-Derived Carbon Fibers

Thermal stability of the PAN fibers was studied by means of thermogravimetric analysis (Q500 TA instrument). TGA was conducted on PAN fiber samples from 30°C to 400°C with a nitrogen flow rate of 60 ml/min and a heating rate of 5°C/min. Thermogravimetry is primarily influenced by an accurate heating rate and conditions. TGA offers a quantifiable analysis of the amount of moisture and volatile compounds present in fibers, weight loss, and thermal

breakdown, and it also assists in determining the degradation mechanism. A TGA study was employed to determine the weight loss patterns of PAN fibers as a function of temperature. Figure 4.5 shows the thermogravimetric curves (TGA thermograms) of PAN-derived carbon fiber composites.

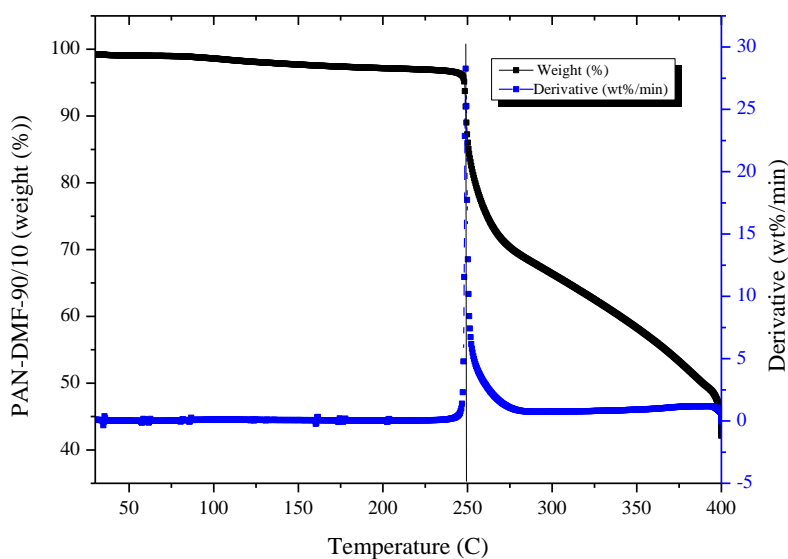


Figure 4.5. Thermogravimetric curves of PAN-derived carbon fiber composites.

The initial weight loss at around 149.56°C (~3–4 wt%) could be due to moisture absorbed by PAN and residual DMF [23]. A significant weight loss occurred at 270°C. According to some studies, weight loss at the stabilization temperature (270–280°C) is due to the evolution of HCN groups [23, 24, 25]. It has also been reported that the higher heating rate affects the weight loss, that is, the higher the heating rate, the higher the weight loss [23]. The higher heating rate increases the exothermic rate since PAN is not a good conductor. Therefore, higher heating rates cause overheating and decomposition of PAN [23]. A dramatic weight loss between 280°C and

330°C may be attributed to the pyrolysis of PAN nanofibers and partial decomposition of PAN [22]. The weight loss after 330°C indicates total decomposition of PAN.

4.3.4 Dynamic Mechanical Analysis of PAN-Derived Carbon Fibers

Dynamic mechanical analysis, a dynamic method of characterizing the viscoelastic behavior of material, is done by applying a sinusoidal force (or displacement) and measures the response to that input. If the material is not purely elastic, then the response will be out of phase with the input [26]. From the out-of-phase response, viscoelasticity can be measured. Samples can be tested in various configurations: double cantilever, single cantilever, three-point bending, torsion, shear, tension, and compression. This study employed three-point bending, which is a common configuration for composite materials since it eliminates the combined loading that takes place by a single- or double-cantilever mode, and it provides measurable strains in relatively stiff materials [26, 27]. Figure 3.6 shows a specimen in the DMA three-point bending fixture.

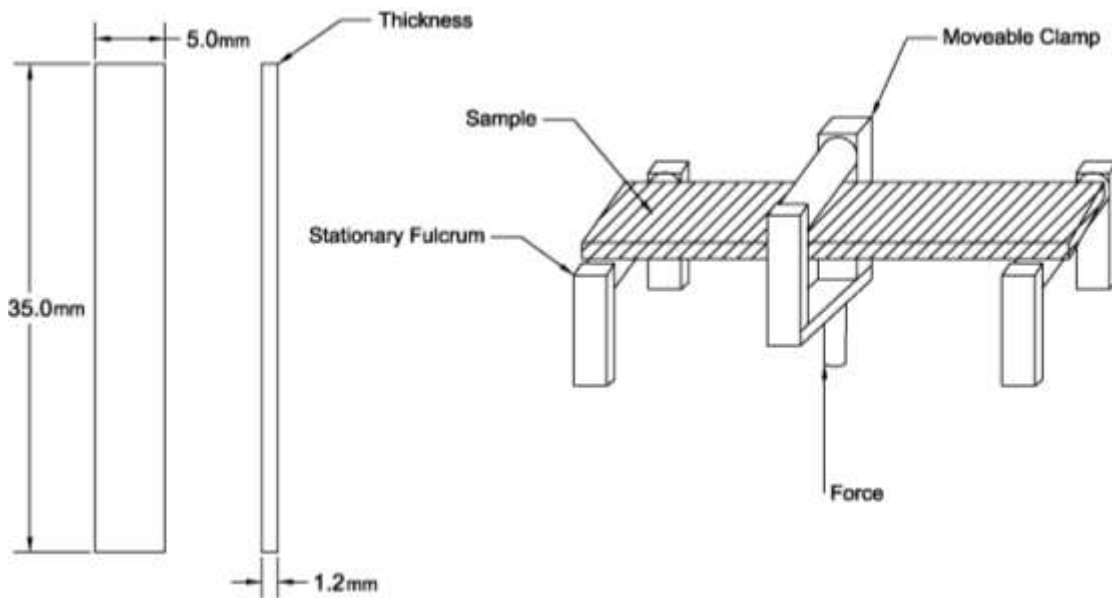


Figure 4.6. Specimen mounted in DMA three-point bending fixture.

A DMA system (Q800, TA Instruments) was employed to generate DMA curves under a heating rate of 5°C. The test was run at an oscillation frequency of 1 Hz. The sample size was 5 x 35 mm² with a thickness of 1.26 mm. In this trial, first, the PAN nanofibers were dried in a vacuum at 50°C to remove absorbed moisture. Then, DMA tests were performed in the temperature range of 0–205°C under a nitrogen environment. Typical DMA curves are shown in Figures 4.7 and 4.8.

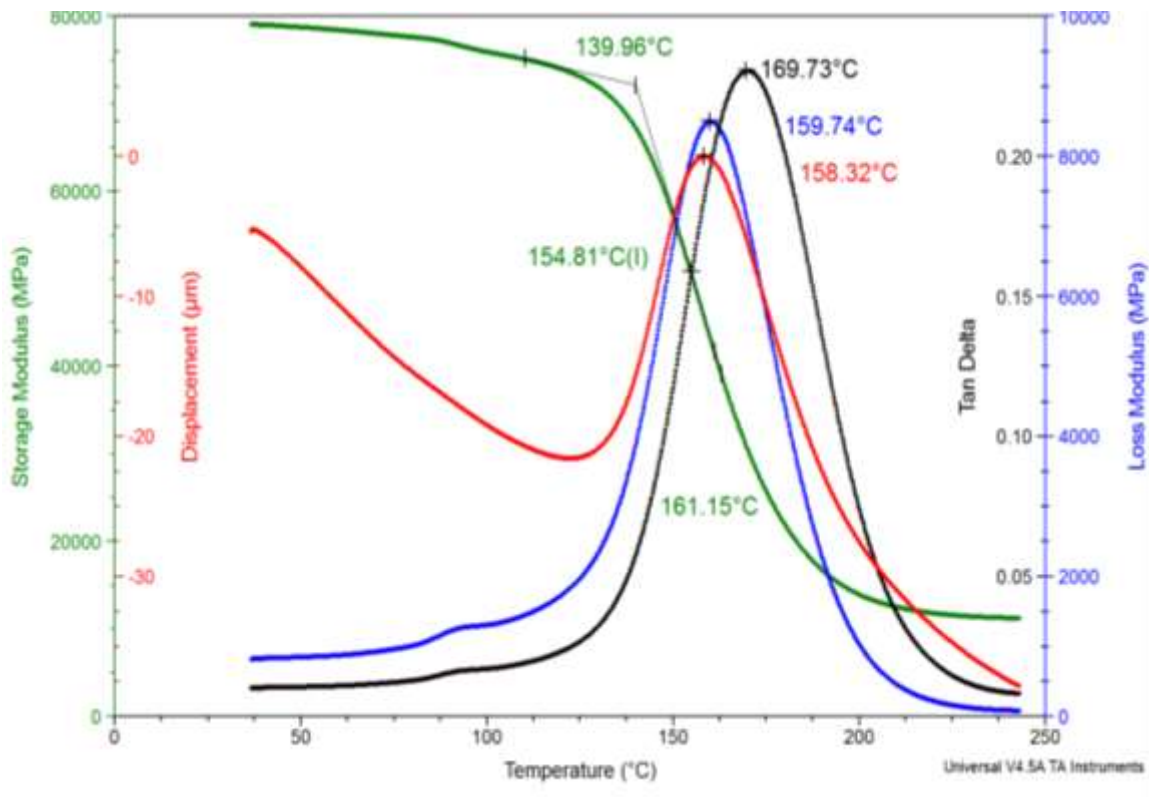


Figure 4.7. DMA curves of storage modulus, loss modulus, and $\tan \delta$ of carbonized PAN nanocomposite fibers.

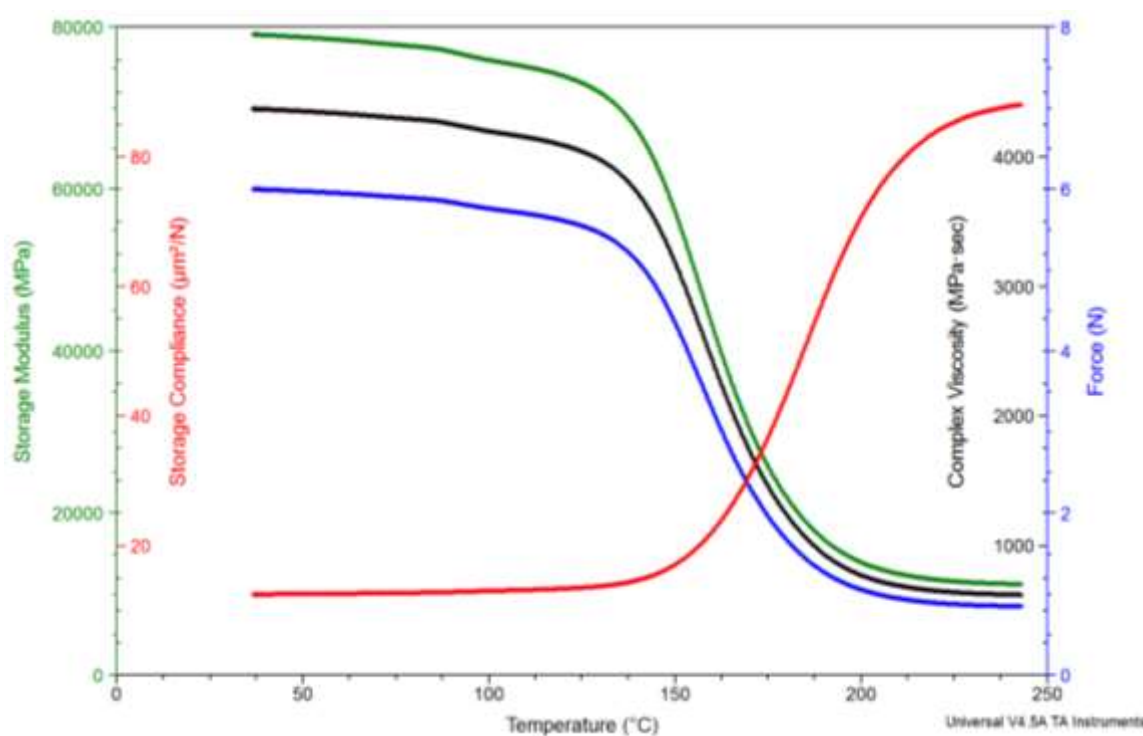


Figure 4.8. Storage modulus (E') curves as a function of temperature for pre-preg carbonized nanofibers, complex composite viscosity as a function of temperature, and change in system compliance as a function of force level up to 6 N.

DMA analysis provides information on the storage modulus, loss modulus, damping factor, and complex viscosity data [29]. The dynamic storage modulus is nearly similar to the elastic modulus or stiffness. The damping factor ($\tan \delta$) is used to provide information on the contributions of viscous and elastic components of a viscoelastic material [29]. The dynamic loss modulus provides information on the energy absorbed due to relaxation and is helpful in clarifying the mechanisms of internal motions [29]. When the polymer experiences the glass transition, its storage modulus decreases significantly, and its loss modulus and damping factor reach a maximum value [29]. The complex modulus is the sum of the storage modulus and loss modulus. The ratio of storage modulus and loss modulus is the damping factor and indicates the loss of energy in the form of heat resulting from the viscoelastic properties of PAN. Polymers

have both elastic and viscosity characteristics; therefore, the complex modulus is the sum of both the elastic and viscosity parts.

The green line shown in Figure 4.8 indicates the storage modulus (E') as a function of temperature for the carbonized PAN nanofibers. As can be seen, the sharp transition in the storage modulus corresponds to the glass transition. The storage modulus is increased by the stiffness effect of the carbonized PAN fibers, which is particularly significant at higher temperatures. As shown in Figure 4.7, the glass transition temperature can be found from either the first inflection point of the storage modulus curve, the peak of the loss modulus curve, or the peak of the $\tan \delta$ curve [26]. Depending upon methodology, the T_g could vary up to 25°C [26, 28].

During the glass transition temperature, a change in stiffness occurs. PAN is a semi-crystalline polymer, and crystallites impart a high modulus in carbonized PAN fibers. The black curve in Figure 4.7 shows the $\tan \delta$ peak of carbonized PAN fibers. This peak moved slightly to a higher temperature, i.e., 169°C, indicating that heat treatment impedes the chain segmental motion. Some broadening of the $\tan \delta$ peak was observed; however, this is not as significant as initially thought. The effect of crystallinity plays a major role in a broadening of the $\tan \delta$ peak. Around 140°C, a rapid decrease in the elastic part of the modulus (storage modulus) can be observed (Figure 4.7), while $\tan \delta$ is moving towards the maximum. This relaxation phenomenon can be attributed to energy dissipation involving cooperative motion of polymer chain fragments, in relation to the glass transition phase.

Also, as shown in Figure 4.7, the $\tan \delta$ peak appeared at 169.73°C, which could be attributed to the T_g of PAN. The $\tan \delta$ was stable at low temperatures but increased to a

pronounced peak as the temperature was increased above 150°C, thus indicating high damping due to the initiation of motion in the chain segment of the polymer [38]. At low temperatures, the storage modulus has the maximum value, and as the temperature increases the moisture and water molecules in the PAN fibers evaporate and ultimately contribute to the decrease in the modulus. Figure 4.8 shows the dynamic properties vs. temperature for a specimen. At high temperatures, the modulus of composites is dominated by the intrinsic matrix modulus. The storage modulus decreases as a function of the temperature throughout the temperature range used in this experiment due to thermal expansion of the polymer at high temperatures. The polymer molecules become rigid below the glass transition temperature, indicating an increase in storage modulus due to the fact that polymer chain segments become immobile. However, the storage modulus drops significantly as the temperature increases since the polymer chain segments become more flexible.

As can be seen in Figure 4.8, the loss modulus increased with the increase in temperature. When the composites were subjected to external stresses due to heating, the energy dissipated as the result of friction between adjacent plies. Figure 4.8 also shows the temperature dependence of pure carbonized nanofibers composite. It can be seen that the G-peak of the carbonized composite sample decreased slowly in the temperature range from 50°C to 200°C but dropped dramatically between 150°C and 200°C due to the glass transition temperature [5]. The complex viscosity η of the pure carbonized nanofibers composite dropped slowly, depending on the temperature [5].

4.3.5 Differential Scanning Calorimetry of PAN-Derived Carbon Fibers

A differential scanning calorimetry system (Q1000, TA instrument) was employed to generate DSC thermograms under a heating rate of 5°C/min from 50°C to 380°C. A pre-determined weight of each sample was used in this experiment. The DSC heat flow and temperature were calibrated with an indium standard. A given sample of 3–6 mg was sealed in a platinum pan, and the measurements were conducted in the temperature range of 50–400°C. The DSC heat flow and temperature were calibrated with an indium standard. Figure 4.9 shows the DSC thermograms of PAN nanocomposite fibers carbonized at 850°C.

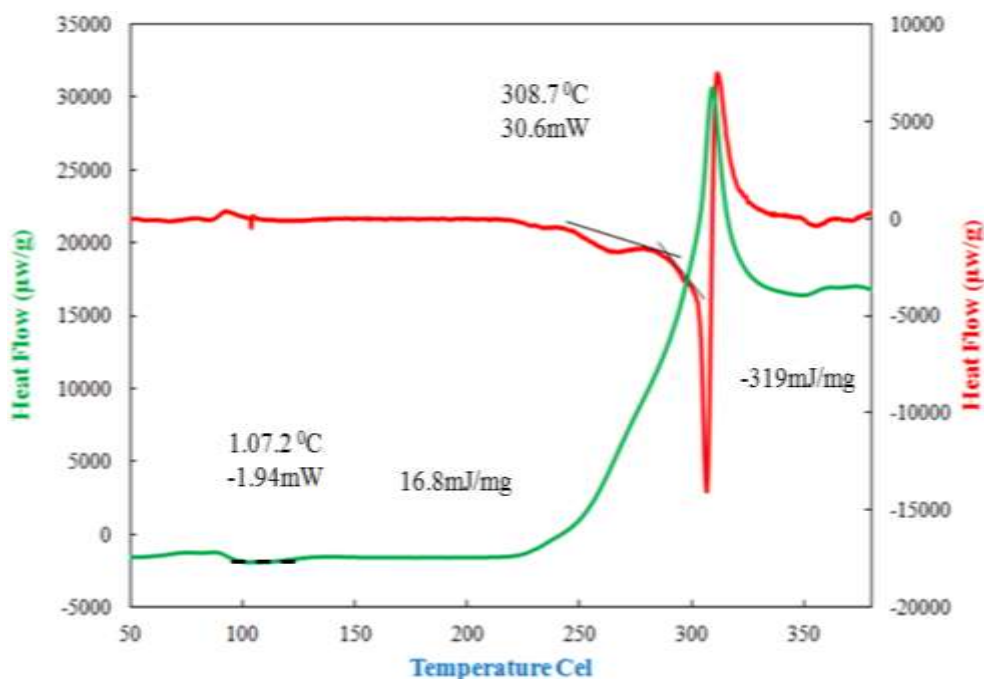


Figure 4.9. DSC thermogram curves of carbonized PAN nanocomposite fibers at 850°C.

The two sets of thermogram curves shown in Figure 4.9 represent heating and cooling, and reveal two major features that follow the DSC analysis. First, with PAN being a semi-crystalline polymer, a glass transition with an amorphous phase was expected [30]. As can be

seen, the glass transition temperature of the carbonized PAN is 107.2°C. The T_g of pure PAN is around 95°C. The increase in T_g may be attributed to the presence of polar solvent (DMF) entrapments in the pores and voids present in the fibers, which could potentially cause dipole-dipole interactions with nitrile groups that are present in the PAN structure. Also shown in Figure 4.9 is a broad exothermal peak (green line) at 320°C. The increasing exothermic peak may be due to the cyclization process. The cyclization of nitrile groups is highly exothermic and leads to fragmentation of the polymer chains owing to the rapid heat build-up in the sample, whereby the heat does not dissipate rapidly [31].

Reneker and Chun [12] calculated the melting temperature of PAN as 317°C using a series of experiments with PAN in DMF and γ -butyrolactone. The strong nitrile dipole interactions are the main reason for the high melting point of PAN [32]. The single exothermic peak observed in all DSC thermograms can be attributed to the cyclization of PAN molecular chains [33]. It is well known that cyclization reactions in PAN are based on free radicals and the initiated high temperature [34]. Therefore, the single exothermic peak observed in PAN can be attributed to the overlapping of the free radical cyclization and other exothermic reactions that can take place at high temperatures [34, 35]. Cyclization is a highly exothermic process and is accompanied by the evolution of a large amount of heat flow that can cause cyclization of the nitrile group in PAN [34]. The intermolecular oligomerization of nitrile groups leads to the cross-linking structure and is possibly more important than the intramolecular reaction leading to the ladder-like structure at high temperatures in PAN [36]. The oligomerization of nitrile groups at high temperature (above 200°C) can be a radical mechanism. For the main chain carbon-carbon bonds, which are the weakest bonds in PAN, a homolytic main chain scission occurs

during heat treatment, and the formed radicals initiate nitrile oligomerization [36]. From DSC thermograms, it is clear that the melting temperature of pure PAN fiber is 320°C. Dimethylformamide may also cause a plasticized effect in the PAN polymer and may be responsible for forming complexes [31].

4.3.6 Thermomechanical Analysis of PAN-Derived Carbon Fibers

Thermomechanical analysis is used to measure dimensional changes under controlled temperature, time, force, and atmosphere. A TMA analyzer (Q400, TA Instruments) was employed to observe dimension changes in the PAN nanocomposite. The sample size was 5x5 mm with a thickness of 1.26 mm, heating ramp of 5°C/min, and maximum temperature of 250°C. TMA is useful in measuring dimensional properties such as the coefficient of thermal expansion and penetration during heating. In structural health monitoring, the dimensional stability of the sensor is the most important aspect. However, TMA is extremely useful in the electronic industry since it confirms that the electronic components manufactured have the same CTE. Figure 4.10 shows the TMA schematics used in this study.

Figure 4.11 shows the dimensional changes of the sample versus time and temperature. Here, the deviation in the curve from a linear behavior at 215.68°C could be due to the rubbery state of the polymer. Theoretically, the slope of the curve changed at the gel point of the composites. The dimension change from 63.3 μm to 3.479 μm was the result of sample shrinkage between temperatures 157.35°C and 140.28°C. The curing cycle of typical carbonized nanofibers composites indicates that chemical shrinkage undergoes thermal expansion [39] and will shrink the resin in the heating step. In the cooling step, the resin will shrink again, depending

on temperature, and the dimension changes are frequently measured [39]. Sample shrinkage was due to thermal expansion in the 0° direction.

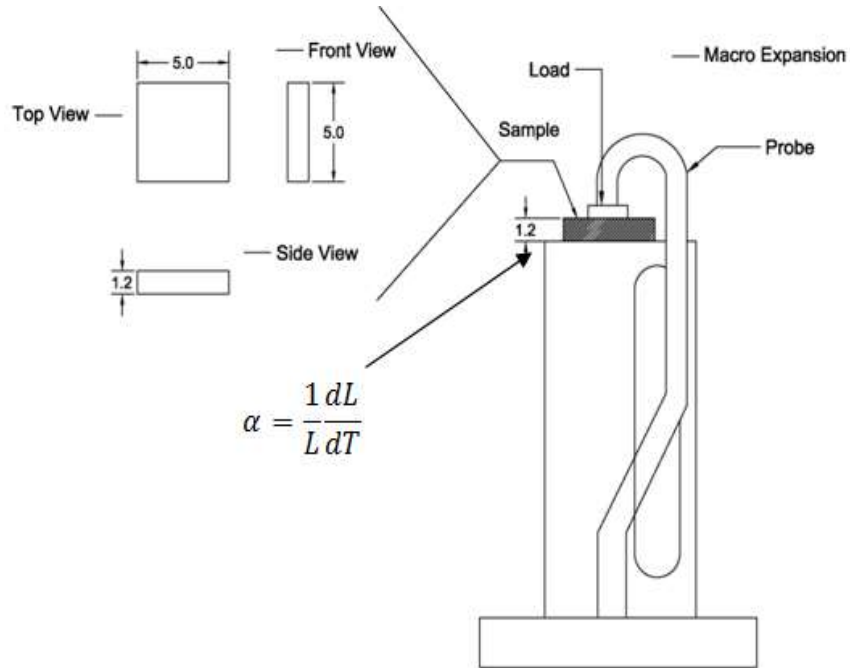


Figure 4.10. Schematics of TMA used in this study.

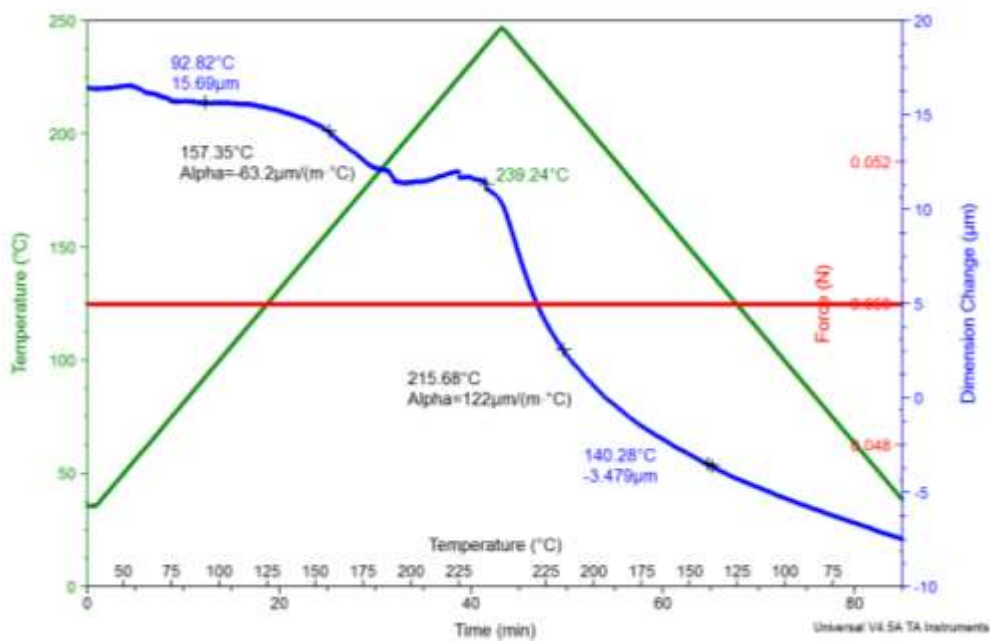
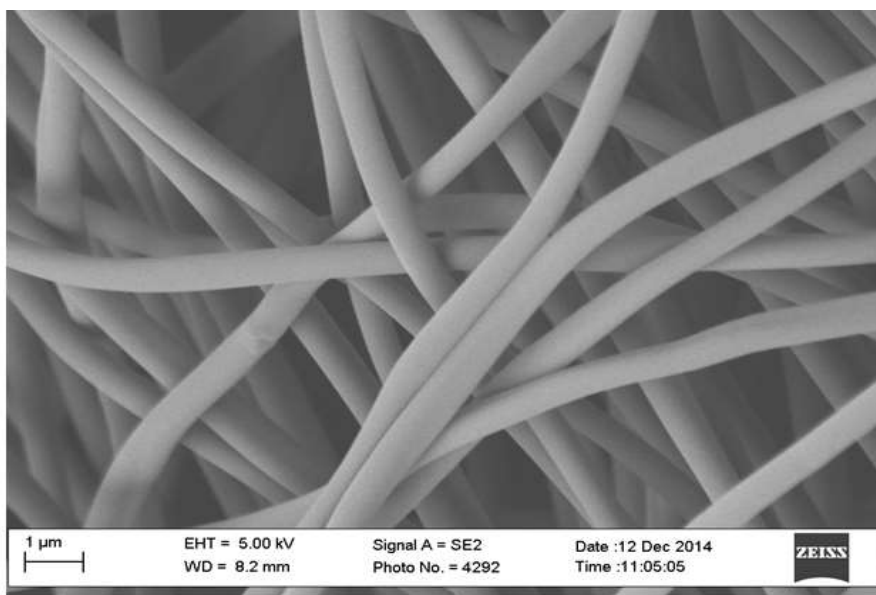


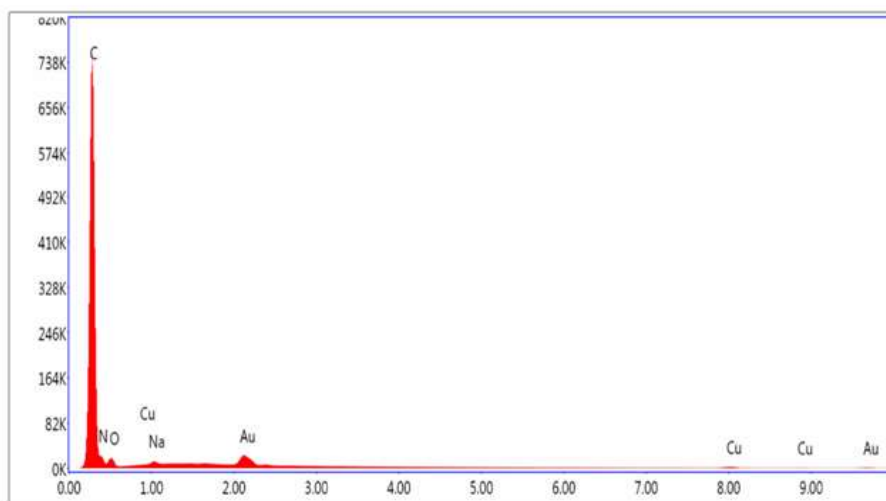
Figure 4.11. TMA curves of CTE, thermal expansion of carbonized nanofiber-reinforced composite in 0° direction.

4.3.7 Energy-Dispersive X-Ray Analysis

The energy-dispersive X-ray (EDX) analysis of carbonized PAN nanofibers was conducted to investigate the morphology of fibers and elemental analysis. Figure 4.12 shows the SEM image and results of the EDX analysis of the carbonized PAN nanofibers.



(a)



(b)

Figure 4.12. Carbonized PAN fibers: (a) SEM image; (b) results of EDX analysis.

Table 4.1 shows the quantity analysis of elements in the carbonized PAN fibers. EDX analysis of these fibers indicated the presence of a high percentage of carbon as well as nitrogen, due to the presence of nitrile groups in the PAN polymer. Also, O₂ was present in a significant amount (5.51 wt%). Some impurities present in minute amounts were Na, Au, and Cu. The large content of carbon, as indicated by the peak in Figure 4.12, was due to the elimination of noncarbonaceous matter during the carbonization process. Results indicate that carbon and nitrogen were the principal elements of the carbonized PAN sample. EDX analysis does not show any other significant peaks (Figure 4.12). However, a few small bumps can be seen, confirming the presence of a small amount of other impurities. After the stabilization and carbonization processes, the diameter of the PAN fiber was reduced by 15–25%.

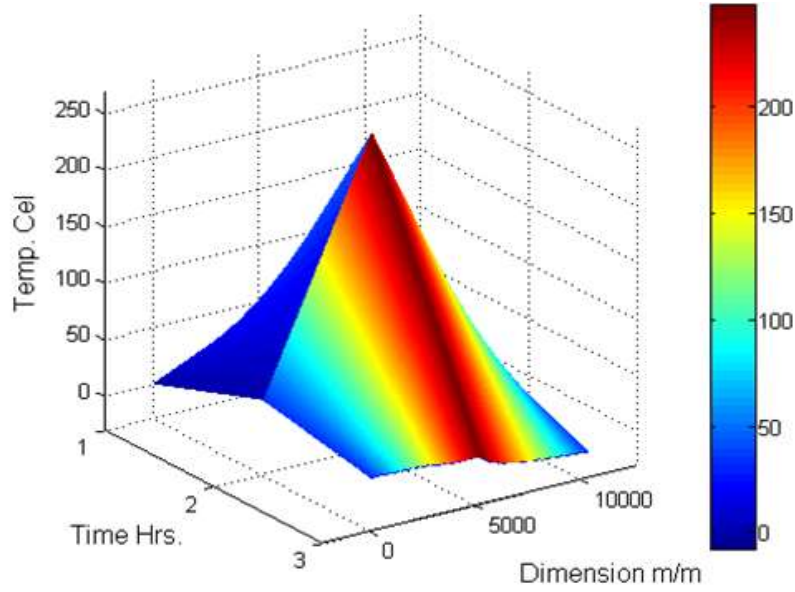
TABLE 4.1
QUANTITY ANALYSIS OF ELEMENTS IN CARBONIZED PAN NANOFIBERS

Elements	Weight%	Atomic%
C	66.17	72.21
N	24.14	22.59
O	5.51	4.51
Na	0.35	0.20
Au	2.21	0.15
Cu	1.62	0.33
Total	100.00	

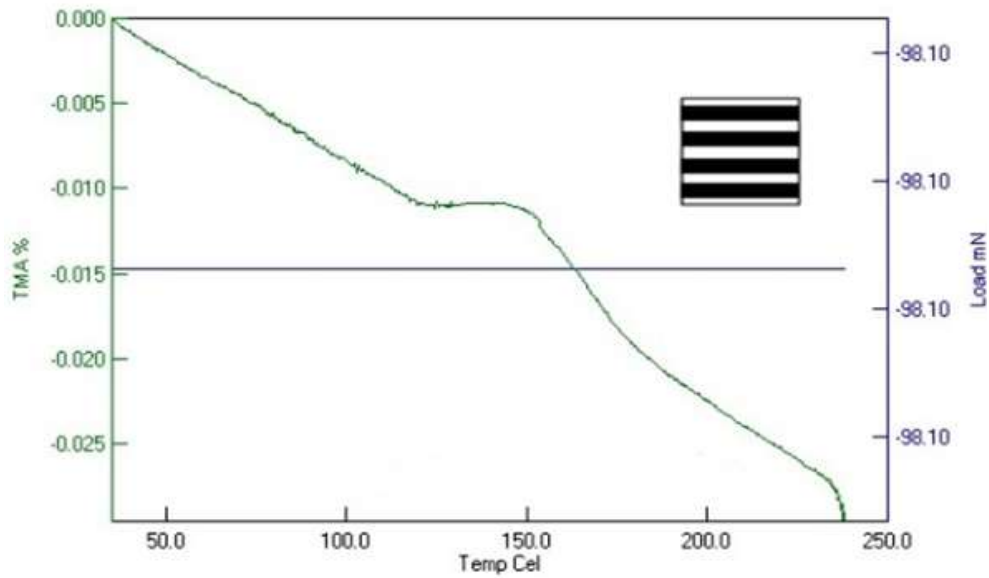
4.3.8 Thermomechanical Analysis

Simulation and experimental results of the thermal expansions of the composites at 0° and 90° orientations were studied in detail and are shown in Figures 4.13 and 4.14. The

coefficients of thermal expansion of the prepreg nanocomposites for the two fiber directions are given in Tables 4.2 and 4.3.

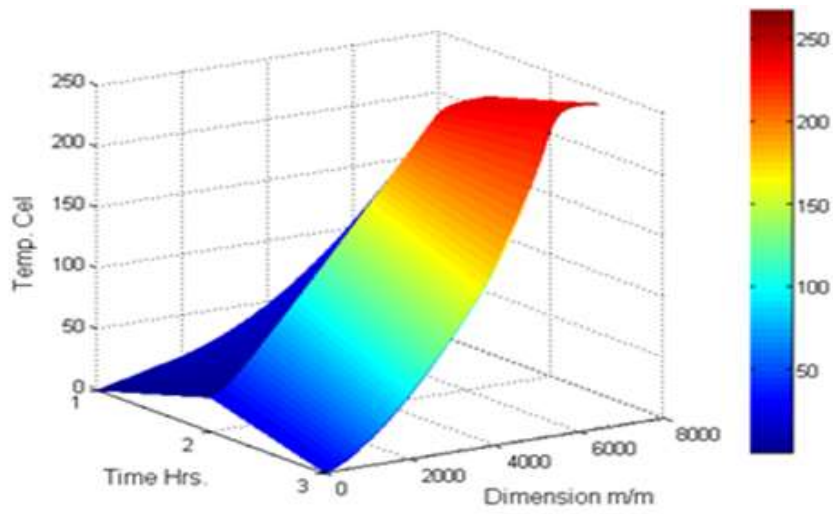


(a)

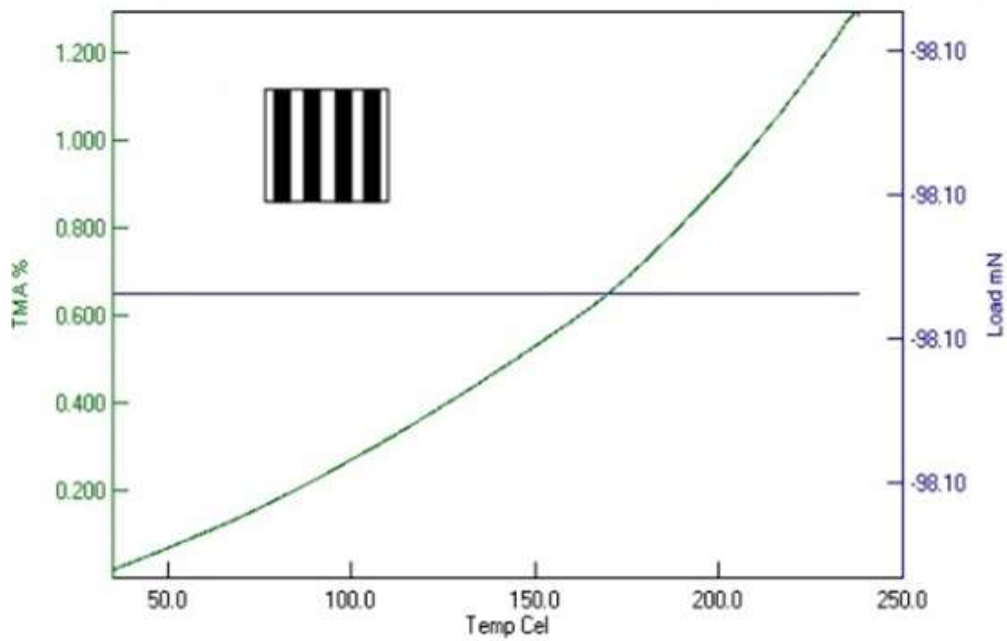


(b)

Figure 4.13. Thermal expansion of components: (a) 3-D mesh surface generated by MATLAB; (b) CTE curves of prepreg nanocomposites with 0° plies orientation.



(a)



(b)

Figure 4.14. Thermal expansion of components: (a) 3-D mesh surface generated by MATLAB; (b) CTE curves of prepreg nanocomposites at 90° plies orientation.

TABLE 4.2

AVERAGE LINEAR THERMAL EXPANSION COEFFICIENT OF PREPREG CARBON NANOCOMPOSITES AT 0° ORIENTATION

Sample No.	Start (°C)	End (°C)	CTE (μ strain)
1	57.37	87.9	-1.2
2	88	117.8	-1.3
3	118.5	139.5	-0.075
4	140	153	-0.66
5	153.2	180.5	-2.8
6	180.5	209.6	-1.5
7	210	233.6	-1.4

TABLE 4.3

AVERAGE LINEAR THERMAL EXPANSION COEFFICIENT OF PREPREG CARBON NANOCOMPOSITES AT 90° ORIENTATION

Sample No.	Start (°C)	End (°C)	CTE (μ strain)
1	49.8	80	37.5
2	80	110	45.7
3	110	140	52.3
4	140	170	59
5	170	200	82.5
6	50	80	37.5
7	80	110	45.7
8	110	140	52.3
9	140	170	59
10	170	200	82.5

Figure 4.13(a) shows the 3-D mesh surface generated by MATLAB, while Figure 4.13(b) shows the CTE curves of the prepreg nanocomposite with 0° plies orientations. As shown in Figure 4.13 and Table 4.2, a linear and negative CTE (-1.2 to -1.3μ strain) was found in the initial temperature range, which is between 57.3°C and 118°C . However, a deviation from linear behavior (from -1.3 to -0.075μ strain) was observed between 118°C and 139°C . The coefficient of thermal expansion is a quantitative evaluation of the expansion of a material over a temperature range. The CTE is not only sensitive to the glass transition temperature but also to the fiber direction. Changes in the CTE in this temperature range are due to relaxation in the molecular orientations in both prepreg carbon fibers and PAN nanofibers around the glass transition temperature of pure PAN, which is approximately 105°C . Around the T_g of PAN, a thermal mismatch possibly occurred due to variations in the CTE of PAN nanofibers and prepreg carbon fibers. A slight increase in the T_g could be attributed to the presence of prepreg carbon fibers and calcination of PAN nanofibers at 950°C . At the glass transition zone, the prepreg nanocomposite exhibits a pronounced change in slope due to an increase in the rate of expansion. From Figure 4.14 and Table 4.3, the prepreg scheme with 90° plies orientation shows entirely different behavior. The prepreg nanocomposite with 90° orientation shows linear behavior.

Figure 4.14 reveals the TMA expansion results with no significant variation in linear behavior near the glass transition region. However, the highest CTE can be observed in the temperature range of 49 – 80°C . This shift in the CTE for the 90° orientation compared to the 0° orientation could be due to the fact that the CTE is significantly different in different directions. Since no carbon fiber is aligned in the 90° orientation, the CTE (in the range of 3.75 to 8.25μ strain) found in this direction represents thermal expansion due to the interaction of the

matrix and the PAN nanofibers alone. These results confirm the directional dependence of CTE in the composite structures.

4.3.9 Mechanical Properties of Pre-preg Nanocomposite

Figure 4.15 shows the linear stress analysis of prepreg nanocomposite, where the maximum elastic strain is about 8.83×10^{-5} and the minimum elastic strain is about 5.45×10^{-5} .

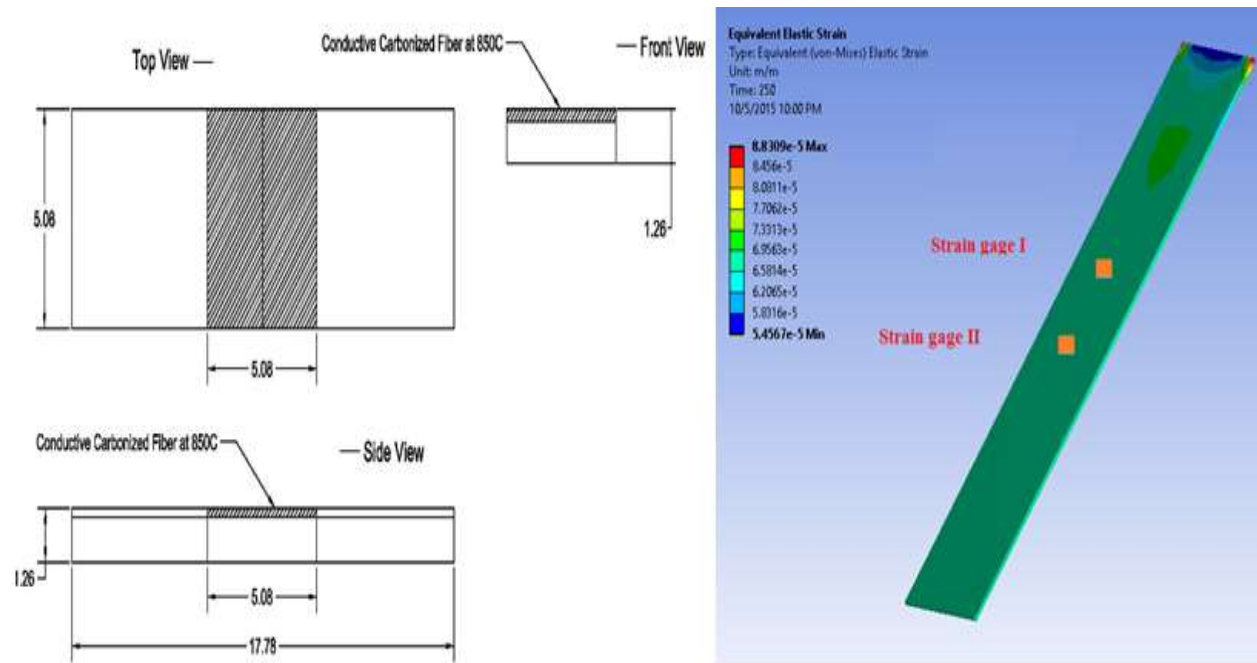


Figure 4.15. Stress analysis of prepreg composites incorporated with carbonized PAN nanofibers as top layers using ANSYS analysis.

Table 4.4 provides the mechanical properties of the prepreg nanocomposite. The mechanical properties of composites depend on many factors, such as fiber and matrix volume ratio, types of fibers and resin materials, curing agents, curing time and temperature, and processing techniques [23]. Therefore, no comparison can be made with other composites. Test results suggest that the carbonized PAN nanofiber composite presents a great compatibility with the carbon prepreg plies, without expensive autoclave processing. Consequently, this

compatibility has definitely improved the interfacial adhesion between the components as well as the mechanical properties of the laminates. In this study, the constraints were applied in only the y-direction during the simulation, so the Young's modulus, which was determined in the y-direction, is 4456 MPa.

TABLE 4.4

MECHANICAL PROPERTIES OF PREPREG COMPOSITES INCORPORATED WITH CARBONIZED PAN NANOFIBERS AS TOP LAYERS

Yield Strength (MPa)	Young's Modulus (MPa)	Poisson's Ratio	Bulk Modulus (MPa)	Shear Modulus (MPa)
3728	4456	0.285	3524	1768.9

4.3.10 Thermal Analysis of PAN-Carbonized Fiber Composite

Figure 4.16 shows the thermal analysis of the prepreg composites incorporated with the carbonized PAN nanofibers as top layers. The sample size was 5×5 mm with a thickness of 1.26 mm, a heating ramp of 5°C/min, and a maximum temperature of 250°C. As shown, the edges of the specimen indicate higher thermal conduction, with thermal expansion of approximately $1.57 \times 10^{-7} \text{ } ^\circ\text{C}$. The minimum thermal expansion was found to be $5.249 \times 10^{-10} \text{ } ^\circ\text{C}$, as shown in the ANSYS simulation in Figure 4.17. The mismatch between the coefficient of thermal expansion of the fiber and the resin causes some distortion in the structures, which is also influenced by the evolution of mechanical properties of the plies (laminated composites) during processing [24]. The fiber properties remain essentially constant or change very little; however, the resin properties change considerably during the curing cycle as the resin polymerizes [24]. This causes residual stresses to build up during the polymerization or curing cycle and subsequently result in some distortion.

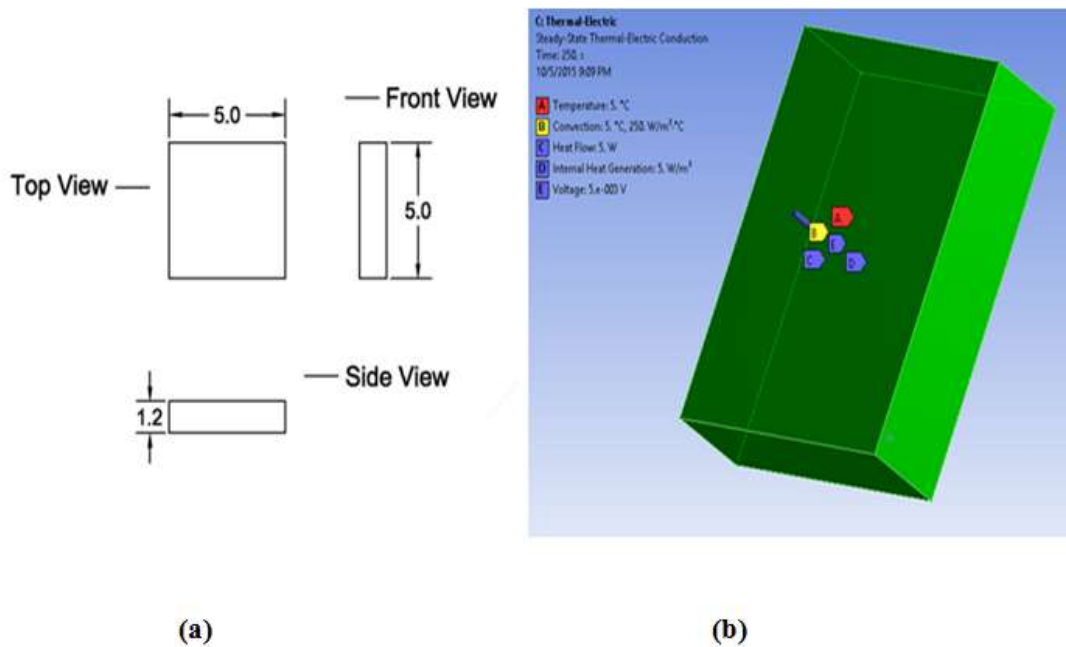


Figure 4.16. Thermal analysis: (a) dimensions of prepreg composites incorporated with carbonized PAN nanofibers as top layers; (b) steady-state from ANSYS simulation.

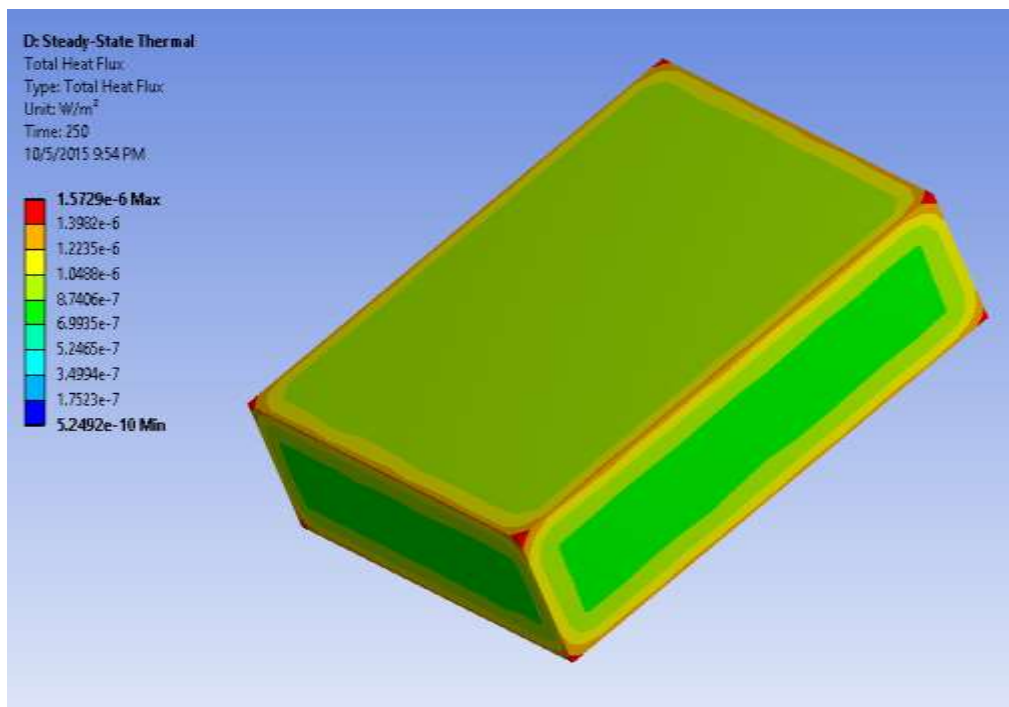


Figure 4.17. Steady-state thermal analysis of carbonized PAN nanofibers using ANSYS simulation.

4.4 Conclusions

PAN-based nanofibers were fabricated via an electrospinning process, and these electrospun nanofibers were used as precursors to prepare PAN-derived carbon nanofibers for thermal treatments including stabilization in an oxidative environment at 280°C followed by carbonization in an inert atmosphere at 850°C. The microstructure and surface morphology of these fibers before and after carbonization were investigated by means of SEM micrograms, which revealed that the average diameter of the fibers decreased about 40–50% after carbonization at elevated temperatures. These PAN-derived carbon fibers were characterized further by means of TGA, DMA, TMA, and DSC analysis in order to determine their thermal and mechanical properties. These studies confirmed that PAN carbon nanofibers are crystalline, have very good thermal and mechanical properties, and integrate well with the prepreg carbon fiber surface. These fibers can be useful for the structural health monitoring, as well as lightning strike and electromagnetic interference shielding applications of new carbon fiber composites.

The PAN nanofibers were synthesized via an electrospinning technique, stabilized in air at 270°C for one hour and then carbonized at 950°C in argon for another hour. The carbonized nanofibers were co-cured with the prepreg carbon fiber composites as top layers to increase the mechanical and thermal properties of the composites fibers. SEM studies indicated significant changes in form and size of the PAN nanofibers before and after the carbonization process. The EDX analysis results clearly confirmed the high content of carbon in carbonized PAN fibers followed by nitrogen, which was due to the presence of nitrile groups in the PAN polymer. The TMA exhibited the glass transition regions in two different prepreg nanocomposite schemes and dependence of the coefficient of thermal expansions in the fiber direction. ANSYS simulation

was used to analyze the mechanical properties of prepreg nanocomposites. A steady-state thermal analysis using ANSYS software was also carried out to distinguish between the CTE of the carbonized PAN fibers and the prepreg nanocomposite. The carbonized PAN nanofibers exhibited the highest thermal conduction around the edges of the specimen with an average CTE of $1.57 \times 10^{-7} \text{ }^\circ\text{C}^{-1}$. However, the highest value of CTE was determined as $37.5 \times 10^{-6} \text{ }^\circ\text{C}^{-1}$ in the temperature range of 50–80°C for a 90° orientation. As far as the 0° orientation is concerned, the highest value of the CTE was recorded as $0.075 \times 10^{-6} \text{ }^\circ\text{C}^{-1}$ in the temperature range of 118.5–139.5°C. The thermomechanical analysis for the 90° orientation exhibited linear behavior. However, the thermomechanical analysis for 0° orientation exhibited nonlinearity behavior. The thermal analysis results displayed a strong dependence of the CTEs on the direction of fibers. Mechanical strain was also found to be dependent on the direction of the fiber orientations. Overall thermal and mechanical analyses of the composite system suggests that this system can be applicable to many structural components of composites.

4.5 References for Chapter 4

- [1] Zhang, C., Ding, X., and Wu, S., “The Microstructure Characterization and the Mechanical Properties of Electrospun Polyacrylonitrile-Based Nanofibers, in *Nanofibers: Production, Properties and Functional Applications*, INTECH Open Access Publisher, 2011, 177 pages.
- [2] Chand, S., “Carbon Fibers for Composites,” *Journal of Materials Science*, Vol. 35, 2000, pp. 1303-1313.
- [3] Salman, N. R., “High Strength Carbon Nanofibers Derived from Electrospun Polyacrylonitrile,” Master’s Thesis, University of Illinois, Champaign, IL, 2010.
- [4] Hammel, E., Tang, X., Trampert, M., Schmitt, T., Mauthner, K., Eder, A., and Pötschke, P., “Carbon Nanofibers for Composite Applications,” *Carbon*, Vol. 42, 2004, pp. 1153-1158.

- [5] Chen, R. Y., Zou, W., Zhang, H. C., Zhang, G. Z., Yang, Z. T., Jin, G., and Qu, J. P., "Thermal Behavior, Dynamic Mechanical Properties and Rheological Properties of Poly (Butylene Succinate) Composites Filled with Nanometer Calcium Carbonate," *Polymer Testing*, Vol. 42, 2015, pp. 160-167.
- [6] Edie, D. D., "The Effect of Processing on the Structure and Properties of Carbon Fibers," *Carbon*, Vol. 36, 1998, pp. 345-362.
- [7] Basova, Y. V., Edie, D. D., Lee, Y. S., Reid, L. K., and Ryu, S. K., "Effect of Precursor Composition on the Activation of Pitchbased Carbon Fibers," *Carbon*, Vol. 42, 2004, pp. 485-495.
- [8] Sutasinpromprae, J., Jitjaicham, S., Nithitanakul, M., Meechaisue, C., and Supaphol, P., "Preparation and Characterization of Ultrafine Electrospun Polyacrylonitrile Fibers and Their Subsequent Pyrolysis to Carbon Fibers," *Polymer International*, Vol. 55, 2006, pp. 825-833.
- [9] Khan, W. S., Asmatulu, R., Ceylan, M., and Jabbarnia, A., "Recent Progress on Conventional and Non-Conventional Electrospinning Processes," *Fibers and Polymers*, Vol. 14, No. 8, 2013, pp. 1235-1247.
- [10] Nuraje, N., Khan, W. S., Lei, Y., Ceylan, M., and Asmatulu, R., "Superhydrophobic Electrospun Nanofibers," *Journal of Materials Chemistry A*, Vol. 1, No. 6, 2013, pp. 1929-1946.
- [11] Dzenis, Y. A., "Spinning Continuous Fibers for Nanotechnology," *Science*, Vol. 304, Iss. 5679, 2004, pp. 1917-1919.
- [12] Reneker, D. H., and Chun, I., "Nanometre Diameter Fibers of Polymer Produced by Electrospinning," *Nanotechnology*, Vol. 7, 1996, pp. 216-233.
- [13] Zussman, E., Chen, X., Ding, W., Calabri, L., Dikin, D. A., Quintana, J. P., and Ruoff, R. S., "Mechanical and Structural Characterization of Electrospun PAN-Derived Carbon Nanofibers," *Carbon*, Vol. 43, No. 10, 2005, pp. 2175-2185.
- [14] Ching-Iuan, Su, Haung, Y. X., Wong, J. W., Lu, C. H., and Wang, C. M., "PAN-Based Carbon Nanofiber Absorbents Prepared Using Electrospinning," *Fibers and Polymers*, Vol. 13, 2012, pp. 436-442.

- [15] Alarifi, I. M., Alharbi, A., Khan, W. S., and Asmatulu, R., "Electrospun Nanofibers for Improved Electrical Conductivity of Fiber Reinforced Composites," *SPIE Smart Structures/Non-Destructive Evaluation Conference*, March 8-12, 2015, San Diego, CA, 8 pages.
- [16] Wangxi, Z., Jie, L., and Gang, W., "Evolution of Structure and Properties of PAN Precursors during Their Conversion to Carbon Fibers," *Carbon*, Vol. 41, 2003, pp. 805-2812.
- [17] Allen, R. A., Ward, I. M., and Bashir, Z., "The Variation of the D-spacings with Stress in the Hexagonal Polymorph of Polyacrylonitrile," *Polymer*, Vol. 35, 1994, pp. 4035-4040.
- [18] Beese, A. M., Pakov, D., Li, S., Dzenis, Y., and Espinosa, H. D., "In Situ Transmission Electron Microscopy Tensile Testing Reveals Structure–Property Relationships in Carbon Nanofibers," *Carbon*, Vol. 60, 2013, pp. 246-253.
- [19] Arshad, S. N., Naraghi, M., and Chasiotis, I., "Strong Carbon Nanofibers from Electrospun Polyacrylonitrile," *Carbon*, Vol. 49, 2011, pp.1710-1719.
- [20] Griffith, A. A., "The Phenomena of Rupture and Flow in Solids," *Philosophical Transactions of the Royal Society of London. Series A*, Vol. 221, 1921, pp. 163-198.
- [21] Tagawa, T., and Miyata, T., "Size Effect on Tensile Strength of Carbon Fibers," *Materials Science and Engineering: A*, Vol. 238, 1997, pp. 336-342.
- [22] Pashaloo, F., Bazgir, S., Tamizifar, M., Faghihisani, M., and Zakerifar, S., "Preparation and Characterization of Carbon Nanofibers via Electrospun PAN Nanofibers," *Textile Science and Technology Journal*, Vol. 3, No. 2, 2009, 10 pages.
- [23] Liu, Y., "Stabilization and Carbonization Studies of Polyacrylonitrile/Carbon Nanotube Composite Fibers," Ph.D. Dissertation, Georgia Institute of Technology, Atlanta, GA, 2010.
- [24] Fitzer, E., Frohs, W., and Heine, M., "Optimization of Stabilization and Carbonization Treatment of PAN Fibers and Structural Characterization of the Resulting Carbon Fibers," *Carbon*, Vol. 24, 1986, pp. 387-395.
- [25] Sivy, G. T., Gordon, B., and Coleman, M. M., "Studies of the Degradation of Copolymers of Acrylonitrile and Acrylamide in Air at 200°C: Speculations on the Role of the Preoxidation Step in Carbon Fiber Formation," *Carbon*, Vol. 21, 1983, pp. 573-578.

- [26] Goertzen, W. K., and Kessler, M. R., "Dynamic Mechanical Analysis of Carbon/Epoxy Composites for Structural Pipeline Repair," *Composites Part B: Engineering*, Vol. 38, 2007, pp. 1-9.
- [27] Li, G., Lee-Sullivan, P., and Thring, R. W., "Determination of Activation Energy for Glass Transition of an Epoxy Adhesive Using Dynamic Mechanical Analysis," *Journal of Thermal Analysis and Calorimetry*, Vol. 60, 2000, pp. 377-390.
- [28] Menard, K. P. *Dynamic Mechanical Analysis: A Practical Introduction*, CRC Press, Boca Raton, FL, 1999.
- [29] Yang, S., Taha-Tijerina, J., Serrato-Diaz, V., Hernandez, K., and Lozano, K., "Dynamic Mechanical and Thermal Tnalysis of Aligned Vapor Grown Carbon Nanofiber Reinforced Polyethylene," *Composites: Part B*, Vol. 38, 2007, pp. 228-235.
- [30] Harry, J. H., "Synthesis, Characterization, Processing and Physical Behavior of Melt-Processible Acrylonitrile Co- and Terpolymers for Carbon Fibers: Effect of Synthetic Variables on Copolymer Structure," Master's Thesis, Virginia Polytechnic Institute and State University, Blacksburg, VA 2006.
- [31] Avilés, M., Ginés, J., del Rio, J., Pascual, J., Pérez-Rodríguez, J., and Sánchez-Soto, P., "Thermal Analysis of Acrylonitrile Polymerization and Cyclization in the Presence of N, N-dimethylformamide," *Journal of Thermal Analysis and Calorimetry*, Vol. 67, 2002, pp. 177-188.
- [32] Bajaj, P., Sreekumar, T. V., and Sen, K., "Thermal Behavior of Acrylonitrile Copolymers Having Methacrylic and Itaconic Acid Co-monomers," *Polymer*, Vol. 42, No. 4, 2001, pp. 1707-1718.
- [33] Xiao, S., Lv, H., Tong, Y., Xu, L., and Chen, B., "Thermal Behavior and Kinetics during the Stabilization of Polyacrylonitrile Precursor in Inert Gas," *Journal of Applied Polymer Science*, Vol. 122, 2011, pp. 480-488.
- [34] Moafi, H. F., Fallah, S., and Ali, Z., "Photoactive Polyacrylonitrile Fibers Coated by Nano-Sized Titanium Dioxide: Synthesis, Characterization, Thermal Investigation," *Journal of the Chilean Chemical Society*, Vol. 56, 2011, pp. 610-615.
- [35] Ouyang, Q., Cheng, L., Wang, H., and Li, K., "Mechanism and Kinetics of the Stabilization Reactions of Itaconic Acid-Modified Polyacrylonitrile," *Polymer Degradation and Stability*, Vol. 93, 2008, pp. 1415-1421.

- [36] Henrici-Olive, G., and Olive, S., "Inter- Versus Intramolecular Oligomerization of Nitrile Groups in Polyacrylonitrile," *Polymer Bulletin*, Vol. 5, 1981, pp. 457-461.
- [37] Ma, X., Yuan, C., and Liu, X., "Mechanical, Microstructure and Surface Characterizations of Carbon Fibers Prepared from Cellulose after Liquefying and Curing," *Materials*, Vol. 7, 2013, pp. 75-84.
- [38] Essabir, H., Elkhaoulani, A., Benmoussa, K., Bouhfid, R., Arrakhiz, F. Z., and Qaiss, A., "Dynamic Mechanical Thermal Behavior Analysis of Doum Fibers Reinforced Polypropylene Composites," *Materials and Design*, Vol. 51, 2013, pp. 780-788.
- [39] Nawab, Y., Shahid, S., Boyard, N., and Jacquemin, F., "Review: Chemical Shrinkage Characterization Techniques for Thermoset Resins and Associated Composites," *Journal of Materials Science*, Vol. 48, 2013, pp. 5387-5409.

CHAPTER 5

GENERAL CONCLUSIONS

The mechanical, thermal and chemical properties of PAN-derived carbon fibers were presented in this dissertation. Carbon nanofibers, like other quasi-one-dimensional nanostructures such as nanowires and nanotubes, have recently been receiving extensive attention due to their applications in composite reinforcement, membrane-based separation, and heat-management materials and more recently as strain sensors due to their piezoresistive properties. Carbon-based piezoresistive sensors such as graphite, graphene, and carbon nanotubes are developing as an alternative for conventional metal/silicon-based microelectromechanical systems due to their high performance and easy manufacturing process with applications ranging from industrial to medical fields. These sensors can be used in in-situ structural health monitoring in industries and in prosthesis applications due to their small size and high sensitivity to minuscule forces. The electromechanical behavior depends on the effect of strain or stress on the electrical resistivity. This phenomenon is commonly known as piezoresistivity, which is related to strain/stress sensors. Piezoresistivity is a conductive phenomenon, and piezoconductivity is a dielectric phenomenon; both are useful for smart materials applications. Carbonaceous materials are extensively used in piezoresistive polymer composites due to their piezoresistive behavior.

Electromechanical sensors, such as pressure sensors, force sensors, strain gages, etc., work on the principle of piezoresistivity. Certain very precise applications require devices that can sense forces and generate output signals. In such applications, small and high sensitive sensors are required. The traditional silicon/metal-based sensors experience many technical

problems such as limited sensitivity, a time-consuming fabrication process, and interference due to external electrical and mechanical fields. In this context, researchers have taken a keen interest in carbon-based materials such as carbon nanotubes, graphene nanoplatelets, and graphite for piezoresistive application due to their unique electromechanical properties, which exhibit a change in resistance with a change in dimension on a very small scale. Carbon nanotubes occupy the major share of the research due to their outstanding piezoresistive behavior.

In this work, PAN electrospun fibers were transformed into almost pure carboneous material through stabilizing and carbonizing, in order to utilize the piezoresistive properties of carboneous materials and apply these properties in fabricating strain sensors for SHM applications. This study presented a cost-effective and easy processing procedure to fabricate PAN-derived electrospun carbon fiber-based piezoresistive sensors commonly known as strain sensors for SHM applications in composite aircraft. The piezoresistive and strain-sensing behavior of pre-preg carbon composite containing a PAN-derived carbon nano mat as a top layer was analyzed by employing a four-circumferential ring probe method. The PAN-derived carbon fibers were characterized further by means of TGA, DMA, TMA, and DSC investigation in order to determine their thermal and mechanical properties. These studies confirmed that PAN carbon nanofibers are crystalline, have very good thermal and mechanical properties, and integrate well with the pre-preg carbon fiber surface. These fibers can be useful for the SHM, as well as lightning strike and electromagnetic interference shielding applications of new carbon fiber composites.

Several characterization techniques, such as XRD, TGA, DSC, FTIR and water contact angle measurements were also employed before and after the carbonization processes in order to

investigate the chemical, electrical, structural, and surface properties of the PAN-based fibers. Test results indicated that after the carbonization of the PAN nanofibers, the physical properties, including carbon weight percent, hydrophobicity, and ionic conductivity, of the nanofibers were drastically improved, which may be useful for various industries that employ SHM systems.

CHAPTER 6

FUTURE WORK

Energy-dispersive x-ray spectroscopy could be used for investigating the chemical characterization or elemental analysis of carbonized PAN fibers in order to confirm that they contain approximately 90% carbon. The presence of a high percentage of carbon is vital for piezoresistivity. Thermomechanical analysis could also be conducted to investigate the glass transition temperature and coefficient of thermal expansion of pre-preg nanocomposites.

In the future, it might be possible to encapsulate either carbon black powder or graphene nanoplatelets in PAN fibers to increase the content of carbonaceous materials further in the prepreg composite and investigate the piezoresistive and strain-sensing behavior of the resulting material. Carbon is found in different allotropic forms, so in the future, it might be possible to combine the latest two allotropic forms of carbon and observe the piezoresistive behavior of the resulting material in different directions. Also, other polymers, such as polyvinyl alcohol, could be used to fabricate graphite/PVA-based piezoresistive sensors for SHM applications.

Polyvinylidene difluoride is a piezoelectric polymer that has been used in many applications, including microphones, transducers, sensors, and actuators. In the future, PVDF electrospun fibers could be used to fabricate composites (piezoelectric fiber composites). Piezoelectric fiber composite products are highly flexible and can sustain extensive deformation without being damaged; also, they are compatible with the processing procedure of composite structures, which makes them an ideal material to be used as an embedded sensor, power harvesting device, or a force actuator within the composite structure.

In the future, characterization and simulation of electrospun PAN nanofibers into pre-impregnated are carbon fiber composites for different industrial applications. Thermomechanical analysis exhibited glass transition regions in the pre-preg nanocomposites and the significant dependence of the coefficient of thermal expansion on the fiber direction. In the near future, the highest value of the CTE could be defined within a temperature range.